Growth History of Galaxy Clusters Traced by Protoclusters at $z \sim 3-6$

Thesis for the degree of Doctor of Science

Jun Toshikawa

Department of Astronomical Science
School of Physical Science
The Graduate University for Advanced Studies

February 25, 2015

ACKNOWLEDGMENTS

First and foremost, I would like to express my deep sense of gratitude to my supervisor, Associate Prof. Nobunari Kashikawa. I could ask him for advice whenever I was in trouble, and he gave me uncountable instruction. Furthermore, he started to teach me even before my entering the graduate university. I could learn many things about the research of astronomy. This thesis would not have been possible unless his support. I am also thankful for the excellent example, he has provided as a successful man both in research and home.

I would like to appreciate Dr. Kazuaki Ota. Thanks to his previous work, I could get my research off to a very good start. He supported my research by giving suggestion as well as data. When I addressed a paper or proposals, he carefully checked them like a referee and provided valuable comments. It is an honor for me to take over his work, and I would like to make further advance.

I would like to show my deep appreciation for Prof. Roderik Overzier. With his great help from theoretical aspects, we were able to push our research toward new directions. Theoretical part of this thesis could not be completed without his supports. I have a lot of respect for his versatility from observational to theoretical research.

I am indebted to my collaborators for providing data, instruction, and comments on my study. Assistant Prof. Tomoki Morokuma provided optical imaging data; Associate Prof. Motohara Kentaro and Dr. Masao Hayashi provided near-infrared imgaging data; Associate Prof. Eiichi Egami provided mid-infrared imaging data. In addition to imaging data, Associate Prof. Kazuhiro Shimasaku, Associate Prof. Tohru Nagao, and Dr. Linhua Jiang brought me spectroscopic data. Dr. Takashi Hattori kindly gave me a lot of help for observations and data analysis, and Dr. Masao Hayashi kindly taught me how to do and gave me useful codes. Thanks to their instruction, I could save time and concentrate on interpretation and discussion. When I had to express my idea or interpretation in a paper or proposals, Prof. Matthew A. Malkan closely checked my English and corrected it to be more impressive. This thesis is constructed from these observational data, and I could not have researched without their cooperation.

I am also grateful to my colleagues, Dr. Takatoshi Shibuya, Mr. Yoshifumi Ishizaki, Mr. Shogo Ishikawa, and Mr. Masafusa Onoue for discussion at the seminar and a lot of help with my study. They empathetically taught me many technical things and answered even my petty questions. Not only about research, they answered my questions about the life in National Astronomical Observatory of Japan or in Tokyo. Therefore, I could get used to new surroundings soon and enjoy my Ph.D. course. On top of that I could get many help from Associate Prof. Tadayuki Kodama, Dr. Masakazu Kobayashi, Dr. Yousuke Utsumi, and Dr. Ken-ichi Tadaki.

I acknowledge financial support from the Japan Society for the Promotion of Science (JSPS) through JSPS Research Fellowship for Young Scientists for that last three years of the doctor course. I have been able to spend all time for my research due to the support.

Finally, I would like to thank to my parents and my wife for their understanding and encouragement. Because they are supporting my life in every way, I can go ahead.

ABSTRACT

We performed a systematic survey of protoclusters of galaxies across cosmic time ($z \sim 3-6$). Protoclusters, which are defined as overdense regions of galaxies in the high-redshift universe, are the precursors of massive clusters of galaxies in the local universe. In the universe at present, the spatial distribution of galaxies is significantly inhomogeneous. This is termed the large-scale structure, and galaxies reside in various environments from clusters to voids; it is clear that the physical properties of galaxies differ depending on their environment. Clusters of galaxies occupy particularly high-density regions in the large-scale structure of the universe, although the universe was initially almost homogeneous. The environments of clusters evolved drastically from the small density fluctuations of dark matter via merging and accretion. Therefore, galaxy clusters are important targets for understanding both galaxy evolution and structure formation. However, the number of known protoclusters is limited, and such structures are particularly rare. Increasing the number of known high-redshift protoclusters is the first step to improving our understanding of the entire history of cluster formation as well as the significance of environmental effects on galaxy evolution. Furthermore, most of the known protoclusters were discovered by using the probe of overdense regions, such as radio galaxies (RGs) and quasars (QSOs), which lie in very massive halos in the local universe. Some contradictory results, including that RGs and QSOs reside in low-density regions, have been observed at high redshift. Systematic searches for protoclusters without RGs or QSOs are imperative to create unbiased samples and to lead correct understanding of cluster growth. In this thesis, we have probed for protoclusters from $z \sim 6$ to $z \sim 3$ with wide-field imaging, not using RGs/QSOs, in order to discover rare objects in high-redshift universe.

We used two sets of wide-field imaging data from the Subaru Deep Field and (SDF) and the Canada-France-Hawaii Telescope Legacy Survey (CFHTLS) Deep Fields. Both datasets are unique in terms of survey depth and area, which is advantageous in finding rare objects in the high-redshift universe. Based on samples selected using a dropout technique, we derived the sky distribution of galaxies from $z \sim 6$ to $z \sim 3$. In total, 22 protocluster candidates were identified from $z \sim 3$ to $z \sim 6$, based on surface overdensity defined by counting galaxies within a fixed aperture. We applied the same overdensity measurement to the simulated galaxy sample, which was selected to have the same redshift distribution from the light-cone model as in the dropout sample. We find that the overdensity at high redshift is strongly correlated with the descendant halo mass at $z = 0$, and $\gtrsim 85\%$ of the overdense regions with significance greater than 4σ are expected to grow up to dark matter halos with $M > 10^{14}\,\mathrm{M}_{\odot}$, which corresponds to nearby rich cluster of galaxies, at $z = 0$. The number density of detected protocluster candidates with an overdense significance of $> 4\sigma$ is approximately one candidate per $1\,\mathrm{deg}^2$, which is consistent with the prediction of the model. The distribution of protocluster members is expected to be within 2 physical Mpc radius on sky, as well as the line-of-sight velocity of $\Delta v < 1000\,\mathrm{km\,s^{-1}}$. Spectroscopic observations were carried out for nine of these candidates, and four genuine protoclusters were discovered by confirming galaxy clustering in spatial and line-of-sight directions. According to the redshifts determined by detecting the Lyα emission lines, we distinguished protocluster members from non-members. Furthermore, we discovered a protocluster at $z = 6.01$, which is the highest-redshift protocluster ever found.

Based on the protocluster sample, we investigated protocluster structure and galaxy properties. We find that a protocluster at $z = 6.01$, which is far from virialization, is composed of

several small galaxy pairs. In contrast, at $z = 3.67$, half of the protocluster galaxies are concentrated in the small central region of a protocluster, and the others are distributed around it. This result suggests that protocluster structure evolves drastically toward a virialized structure from $z \sim 6$ to $z \sim 4$, although more protocluster samples are required to confirm a general trend.

We investigated differences in the properties of protocluster and field galaxies. There are no significant differences in $M_{\rm UV}$, $L_{{\rm Ly}\alpha}$, and $EW_{\rm rest}$ at $z = 6.01$; however, the Lyα emission lines are significantly suppressed in a $z = 3.67$ protocluster compared to field galaxies at the same redshift. We consider two possible causes of this difference: attenuation due to dust in member galaxies (which is associated with the rapid evolution of galaxies in high-density environments), and absorption due to intracluster neutral hydrogen gas. We were not able to find differences in UV continuum slope (an indicator of dust) between protocluster and field galaxies. A large amount of neutral hydrogen gas may explain the suppression of Lyα emission lines in protocluster galaxies; however, this hypothesis currently lacks significant supporting evidence. Our finding of Lyα suppression in more dynamically mature protocluster at lower redshift suggests that the properties of protocluster galaxies might be affected by their environment in combination with dramatic changes in the internal structure. However, we find two $z \sim 3$ protoclusters that exhibit inconsistent tendencies in the protocluster properties even at the same redshift. This study, as a precursor to the Hyper Suprime-Cam (HSC) survey, demonstrates that wide-field imaging is an effective tool to locate high-redshift protoclusters, and future HSC surveys will enable us to derive a more complete picture of cluster formation and galaxy evolution in high-density environments.

CONTENTS

1. INTRODUCTION

1.1. Mature Clusters of Galaxies

The present-day universe exhibits the large-scale structures composed of clusters, filaments, voids, and sheet-like structures. The spatial distribution of galaxies is significantly inhomogeneous, and clusters of galaxies (typically containing between 50 and 10^3 member galaxies) are frequently located at the intersections of filaments. These rich structures are surrounded by extremely underdense regions, termed "voids," which contain no (or very few) galaxies. The large-scale structure was first discovered from the angular distribution of galaxies based on photographic maps (Seldner et al. 1977). Subsequently, many of the early galaxy surveys, such as the CfA Redshift Survey (de Lapparent et al. 1986), more clearly revealed the structures of the distribution of galaxies. Modern galaxy redshift surveys, such as the Two-degree Field Galaxy Redshift Survey (2dFGRS; Colless et al. 2001), the Sloan Digital Sky Survey (SDSS; e.g., Tegmark et al. 2004), and the Galaxy And Mass Assembly (GAMA; Driver et al. 2011), revealed a more obvious filamentary structure, and showed that clusters form large networks of galaxies, termed the "cosmic web," connected by groups of galaxies or filaments (e.g., Smargon et al. 2012; Einasto et al. 2014). From these observations, we recognized that galaxies reside in various environments from clusters to voids in the local universe. At the beginning of the universe, however, the amplitude of the density fluctuations was small. Exploring the structure formation toward the early universe has been one of the hottest issues in astronomy in recent years. Our understanding of large-scale structure have been aided by sophisticated simulations (e.g., Aragón-Calvo et al. 2010; Angulo et al. 2012; Park et al. 2012). Based on the cold dark matter (CDM) models, the density fluctuations of dark matter evolve as time progress by merging and by accretion. Baryonic matter accumulates in the gravitational potential wells formed by the dark matter (Springel et al. 2005). Particularly dense matter fluctuations eventually resulted in the formation of galaxies and clusters. Clusters of galaxies, which occupy the densest parts of the large-scale structure of the local universe, have evolved considerably compared to the initial condition of the universe. In principle, we can derive the information on the early universe from observations of the local universe, if the universe evolved under the simple laws of physics. However, due to poorly understood complex physical processes, information derived only from the local universe cannot be used to draw strong conclusions about the evolution of the universe. More reliable results may be obtained from both direct observations of the high-redshift universe and the local universe. Therefore, the growth of density fluctuations measured from comparisons of abundances and mass distributions of present-day clusters with those at earlier times provides unique constraints on the ΛCDM concordance model (e.g., Vikhlinin et al. 2003; Voit 2005; Mortonson et al. 2011).

Clusters of galaxies are of significant astronomical interest in terms of the environmental dependence of galaxy evolution. Observations of the local universe have revealed that the fraction of elliptical galaxies is larger in higher density region; this is known as the "morphology-density relation" (e.g., Dressler 1980). Moreover, clusters of galaxies represent a distinct relationship in the color-magnitude diagram. The "red sequence" of clusters is mainly composed of spheroidal and lenticular galaxies with old stellar populations and high stellar masses (e.g., Visvanathan & Sandage 1977; Lerchster et al. 2011). Bright and red (i.e., massive and old) galaxies are likely to inhabit clusters of galaxies, and the shape of the stellar mass function

is strongly influenced by the environment (e.g., Vulcani et al. 2012). Even in modest galaxy group environments, the star formation is known to be effectively quenched at $z < 0.1$ (e.g., Rasmussen et al. 2012). Furthermore, local clusters sometimes harbour cD galaxies, which are more massive, more extended, and less dense than the normal elliptical galaxies. In particular, massive and bright elliptical galaxies in a cluster have significantly different properties from their field counterparts, such as a larger stellar velocity dispersion and a higher α/Fe ratio. These differences suggest that elliptical galaxies in a cluster contain more dark matter and are characterized by a shorter star-formation timescale (Thomas et al. 2005; von der Linden et al. 2007). These are intuitively expected within the hierarchical structure formation scenario: halos in higher-density regions are expected to collapse earlier and merge more rapidly, leading to earlier galaxy formation and more rapid evolution (Kauffmann et al. 1999; Benson et al. 2001; Springel et al. 2005; De Lucia et al. 2006). In this manner, both observational and theoretical studies predict that galaxy evolution strongly depends on the environment. When and how did these distinct properties form? Galaxy evolution is determined by diverse physical processes, which are closely interrelated. What is the most dominant process in the evolutionary history of galaxy: when or where galaxies are born? Even if galaxies in high- and low-density environments have the same evolutionary history, environmental differences between cluster and field galaxies as seen in the present universe could be caused simply because cluster galaxies are formed earlier. In contrast, it is likely that galaxies follow different growth paths due to posteriori effects following their birth; this would also be an origin of the diversity of the properties of galaxies. In high-density regions, many physical processes, such as galaxy mergers and interactions, would affect the evolutionary history. Highly evolved clusters in the local universe have been intricately affected by both these nature and nurture physical processes; thus, it is difficult to sort out which factors are more essential in our understanding of cluster and galaxy evolution. One promising approach is to directly investigate the primitive properties of galaxies in the first clusters of galaxies to appear during the early epoch.

As described above, clusters of galaxies are important targets in terms of both structure formation and galaxy evolution. The number density of clusters in the local universe is typically $10^{-6} - 10^{-7}\,\mathrm{Mpc}^{-3}$, although it depends on the richness of the cluster, as well as the number density of groups or poor clusters is $10^{-4} - 10^{-6}\,\mathrm{Mpc}^{-3}$ (Bahcall & Cen 1993). Clusters of galaxies are defined as being in dynamical equilibrium, and the deep gravitational wells contain the bulk of the very hot gases ($\mathrm{T} \geq 10^{7}\mathrm{K}$). As a result, clusters of galaxies are detected most readily from X-ray emissions (e.g., Rosati et al. 1998), or by the effects on the cosmic microwave background (e.g., Sunyaev & Zeldovich 1972; Barbosa et al. 1996); most known clusters of galaxies have been discovered during astronomical X-ray surveys (e.g., Böhringer et al. 2004; Lloyd-Davies et al. 2011; Reichardt et al. 2013). The other commonly used method to identify clusters of galaxies is using optical and infrared photometry, which can be used to determine the overdensity of massive and passive galaxies at high redshift (e.g., Gladders & Yee 2000; Eisenhardt et al. 2008). This method relies upon the observation that clusters of galaxies appear to have a red sequence, which is only available in the detection of well-evolved clusters. However, the number of mature clusters, that are detectable via X-ray or red sequence, decreases sharply beyond $z > 1$, and the fraction of star-forming galaxies in a cluster of galaxies increases at higher redshift (Butcher & Oemler 1984; Haines et al. 2009; Lerchster et al. 2011), and a higher star-formation rate (SFR) is observed in higher-density environments at $z \sim 1$ (e.g., Popesso et al. 2011). Distant mature clusters have been discovered at $z \lesssim 2$ using these methods (e.g., Stanford et al. 2006; Papovich et al. 2010; Tanaka et al. 2010; Muzzin et al.

2013). In fact, the most distant mature cluster of galaxies detected via X-ray emission has only been found at $z = 2.00$ (Gobat et al. 2011, 2013), and a cluster candidate with red sequence appears to be at $z = 2.2$ (Spitler et al. 2012). The search for more distant clusters (especially immature clusters) that cannot be identified from X-ray emissions, the Sunyaev–Zel'dovich effect, or red sequences, is required to fully understand their evolutionary history, especially during the primitive phase.

1.2. Forming Clusters: Protoclusters

Protoclusters, which are expected to be forming clusters, would provide much information on the primordial conditions of clusters at their birth; however, they are difficult to find due to their low number density. Beyond $z = 3$, star-forming galaxies, such as Lyman break galaxies (LBGs) and Lyα emitters (LAEs), are almost the only tracers that have been used to follow the evolution of large-scale structures. LBGs are selected from a comparison of the observed flux ratios in different broad-bands (Steidel et al. 1995). This technique makes use of the almost continuous absorption signature due to intergalactic HI gas, which significantly absorbs the continuum blueward part of the $\mathrm{Ly_{limit}}$ and the lines of Lyman series. Because intergalactic HI gas exists at all of the redshifts between targets and observers, the flux at all wavelengths blueward part of the Lyα can be strongly attenuated (Madau 1995; Meiksin 2006; Inoue et al. 2014). In this manner, LBGs are isolated on a color–color diagram using an optimal combination of broad-bands. On the other hand, LAEs are identified by narrow-band excess. Young hot stars produce a large flux of UV continuum photons, which ionize the surrounding interstellar hydrogen. If the galaxies are sufficiently young to be opaque to this ionizing radiation, the light is eventually converted into Lyα photons, which can then escape from the galaxy after multiple resonance scattering. This results in a strong Lyα emission line, which is observed as a narrow-band excess. However, this is expected to be observed only when there is no absorption due to dust. Therefore, LAEs are expected to be younger with lower metallicity than LBGs (e.g., Ono et al. 2010a; Finkelstein et al. 2009, 2011). Surveys of high-redshift galaxies have been performed using both techniques to detect continuum depression and prominent Lyα emission (e.g., Rhoads et al. 2000; Ouchi et al. 2003; Bouwens et al. 2007), and statistical samples of higher redshift galaxies beyond $z \sim 7$ have recently been obtained by new facilities (e.g., McLure et al. 2013; Bouwens et al. 2014; Konno et al. 2014; Ishigaki et al. 2014). Following these surveys, a number of $z \gtrsim 7$ galaxies have been spectroscopically confirmed (e.g., Fontana et al. 2010; Vanzella et al. 2011; Ono et al. 2012; Finkelstein et al. 2013).

Although massive clusters such as those seen in the local universe had not yet formed at $z > 3$, protoclusters can be searched for by identifying high surface-number density regions of star-forming galaxies, such as LBGs and LAEs. These can be confirmed as protoclusters, once they have been revealed to also be clustered on the line of sight by spectroscopic observations. There are very few clear examples of these star-forming galaxies that are strongly clustered beyond $z = 2$ (e.g., Le Fevre et al. 1996; Pentericci et al. 1997; Giavalisco et al. 1994; Venemans et al. 2005; Lee et al. 2014). Some have also been found in the overdense regions of other galaxy populations, such as Hα emitters and Extremely Red Objects (ERO) (e.g., Kuiper et al. 2011a). Although young star-forming galaxies form the majority of these protoclusters, some

red and massive galaxies certainly exist in protoclusters, suggesting that environmental effects actually occur at least up to $z \sim 2-3$ (e.g., Galametz et al. 2010; Kubo et al. 2013). It has been found that red galaxies (as selected by NIR photometry) are clustered in known protoclusters, and have already started to form red-sequence galaxies at $2 \lesssim z \lesssim 3$ (Kodama et al. 2007; Zirm et al. 2008; Lemaux et al. 2014). These color differences between protocluster and field galaxies are directly related to the differences in stellar populations, which were evaluated from a combination of multi-color photometry and spectroscopy. For example, stellar mass is a basic and readily observable property that can be used to determine details of the star-formation history; protocluster galaxies have higher stellar masses than their field counterparts (Steidel et al. 2005; Kuiper et al. 2010). Hatch et al. (2011b) reported that the total SFR density within protoclusters is greater than that of field galaxies by an order of magnitude; however, the mean SFR is similar between protocluster and field galaxies. These results imply that the environment does not greatly influence the star-formation activity of protocluster galaxies at $z \sim 2$. Based on these results, the differences in stellar mass at $z \sim 2-3$ between protocluster and field galaxies may be attributed to differences in star-formation duration or the formation epoch. On the other hand, very rare objects, such as Lyα blobs, submillimeter galaxies, and active galactic nuclei, are likely to be discovered in high-density environments (Lehmer et al. 2009; Digby-North et al. 2010; Tamura et al. 2010; Matsuda et al. 2011). Dannerbauer et al. (2014) found an excess of dusty starburst galaxies in a protocluster at $z = 2.2$ from a combination of far infrared and radio observations, implying that the properties of the dust already differed in protoclusters. Furthermore, large amounts of cold gas have been found around a $z = 2.9$ protocluster, which fell into the halo potential well of the protocluster, as an ingredient in star formation (Cucciati et al. 2014). Other differences, such as in metallicity and galaxy size, have also been ascertained (e.g., Zirm et al. 2012; Kulas et al. 2013; Shimakawa et al. 2014). In addition to revealing differences between protocluster and field galaxies, a wide variety of properties of protoclusters with the same redshift has been revealed (e.g., Valentino et al. 2014). At $z \sim 2-3$, there have been many observations revealing differences between protocluster and field galaxies; however, the causes of these differences remain unclear. To address this question, further observations of higher-redshift protoclusters are important to probe the onset of the initial environmental effects in the early universe.

Although the physical properties of protoclusters at higher redshifts are not well characterized (primarily due to the difficulties in multi-wavelength imaging as well as the limited quantity of spectroscopic data), a handful of sample protoclusters have been discovered at $z > 4$ (e.g., Ouchi et al. 2005; Venemans et al. 2007; Capak et al. 2011; Kuiper et al. 2011b), and some overdense regions have been identified without spectroscopic confirmation at higher redshifts (Malhotra et al. 2005; Stiavelli et al. 2005; Zheng et al. 2006; Kim et al. 2009). Even at $z \sim 8$, an overdense region of Y-dropout galaxies has been identified (Trenti et al. 2012). In earlier epochs, at $z \sim 4-5$, Overzier et al. (2009b) found no significant difference in the stellar mass between protocluster and field galaxies, and only found differences in the number density. In addition, Overzier et al. (2009b) showed that the total stellar mass of protocluster galaxies at $z = 4.1$ is significantly smaller than that of early type galaxies with ages of > 3.5 Gyr, indicating that these galaxies were formed at $z \gtrsim 4$, in a massive cluster at $z = 1.2$. If the protocluster is a progenitor of a massive cluster, this would suggest that we miss a large fraction of the mass that is expected to have already existed at $z \sim 4$. Many possibilities exist to explain the causes of the stellar-mass deficit. For example, protocluster members may be spread over a much wider spatial extent at $z \sim 4$, and we may fail to find a large fraction of the protocluster galax-

ies due to the small field-of-view (FoV). Alternatively, we may miss other galaxy populations, including old and passive galaxies, which could drop out from the sample selection processes that are optimized for star-forming galaxies (e.g., LBG and LAE). Some galaxies are found to have already undergone episodic star formation, even at $z \sim 5$. This is likely to be triggered by galaxy merging or interaction, which occurred frequently in high-density environments. In addition, it is also possible that protoclusters are progenitors of smaller clusters or groups. If so, we may expect that there would be other more massive protoclusters at $z \sim 4$, which will become rich clusters at $z \sim 1$.

It is important to search for protoclusters across cosmic time in order to directly investigate protoclusters at even higher redshifts. The small number of known protoclusters, especially at $z > 3$, makes it difficult to identify systematic trends in terms of the cluster formation history. Increasing the number of high-redshift protoclusters is the first step in understanding the history of cluster formation as well as the significance of environmental effects on galaxy evolution. As mentioned above, protoclusters have been found from $z \sim 2$ to $z \sim 6$; however, these are heterogeneous samples, collected with different sample selection criteria, overdensity estimates, and definitions of protoclusters. For this reason, a systematic approach with a uniform method is desirable to eliminate some difficulties in comparing protoclusters. Furthermore, follow-up spectroscopy is also important in the study of protoclusters. An analysis based only on photometric data limits a detailed understanding of physical properties in the high-density environment, such as the three-dimensional structure. In addition, samples may be contaminated by lower-redshift objects, which dilute the intrinsic properties of protoclusters.

To locate and identify rare objects such as protoclusters, wide surveys are required. Deep observations are also necessary to find faint galaxies at high redshifts. However, in practice, it is difficult to simultaneously perform both wide and deep observations due to instrumental limits: generally, large telescopes do not have a wide FoV. Protoclusters beyond $z > 3$ ($N \sim 10-20$) have been discovered in regions centered on radio galaxies (RGs) or quasars (QSOs) (Miley & De Breuck 2008, and references therein). Rhs and QSOs have been used as potentially useful probes of large-scale structure (i.e., as signposts of possible regions of galaxy overdensity). In the local universe, Mandelbaum et al. (2009) showed that the host dark matter halo of radio-loud active galactic nuclei (AGN) was massive ($> 10^{12.5}\,\mathrm{M}_{\odot}$), and furthermore, was more massive than that of normal galaxies with the same stellar mass, based on clustering and galaxy–galaxy lensing analysis. Although this result implies that radio-loud AGNs follow a different halo mass–stellar mass relation than normal galaxies, they did not find a dependence of the radio luminosity on the halo mass. Similar results have been obtained at higher redshifts of $0.4 < z < 0.8$ (e.g., Yates et al. 1989; Best 2000; Wake et al. 2008); the clustering strength of radio-loud AGNs is greater on scales of $\sim 1\,\mathrm{Mpc}$ than that of normal galaxies (Donoso et al. 2010). Therefore, at least at $z \lesssim 1$, RGs and QSOs tend to reside in more massive dark matter halos, guaranteeing that they are good probes of high-density environments. We should bear in mind, however, that it remains unclear why there is a relationship between the activity of AGNs and the environment.

Some protoclusters have been discovered at $z \gtrsim 2$ using RGs and QSOs as overdensity probes (e.g., Steidel & Hamilton 1992; Venemans et al. 2007). However, it is not always the case that RGs and QSOs occur in overdense regions of the early universe because strong radiation from RGs or QSOs may provide contradictory feedback that suppresses nearby galaxy formation, especially with low-mass galaxies (Barkana & Loeb 1999). Kashikawa et al. (2007)

found a ring-like structure of LAEs around a luminous QSO at $z \sim 5$, which is possible evidence of negative feedback on star-formation activity in galaxies neighboring QSOs. Morselli et al. (2014) reported four QSOs at $z \sim 6$ that were found possible overdense regions of LBGs; however these LBGs were not located in the vicinity of the QSOs, and were mainly distributed ~ 3 physical Mpc from the central QSOs. QSOs have similar clustering strength to normal L_* galaxies at $z \gtrsim 1.5$ (Croom et al. 2005; Coil et al. 2007). In contrast, at $1.3 < z < 2.3$, it has been found that RGs and QSOs are typically in overdense environments, which are defined by galaxy number count within a fixed aperture centered on an RG or QSO (Mayo et al. 2012; Wylezalek et al. 2013, 2014). More than half of the RG and QSO fields are overdense at the 2σ level, and 9.6% of the RG and QSO fields are overdense at the 5σ level. Hatch et al. (2014) also obtained a similar result by comparing the environments of RGs and radio-loud QSOs with those of a counter sample without AGNs, but with same stellar mass and age distributions. These results suggest that there is a relationship between the environment and the AGN activity apart from the dependence of the mass on the environment. In spite of these findings, however, there is no clear relationship between environment and the physical properties of AGNs (such as the mass of black holes, the radio luminosity, or the spectral index), and it should be noted that approximately 20% of RGs and QSOs reside in underdense regions (Hatch et al. 2014). Many contradictory results have been reported; for examplej, (Hatch et al. 2011a) investigated six RG fields at $z \sim 2.5$, three of which were in overdense regions and the others in underdense regions. Furthermore, at higher redshifts of $z \sim 4-7$, RGs and QSOs were reported in various environments from low- to high-density regions (Bañados et al. 2013; Husband et al. 2013; Simpson et al. 2014; Adams et al. 2014). A few protoclusters or large-scale structures at $z \sim 3-6$ have been discovered serendipitously by blank surveys (e.g., Steidel et al. 1998; Shimasaku et al. 2003; Ouchi et al. 2005; Capak et al. 2011), suggesting that early massive structures do not always host RGs/QSOs. The physical mechanisms for a possible correlation between RGs/QSOs and overdense environments is still veiled in mystery. We may only see biased protoclusters by relying RGs and QSOs to search for overdense regions. Whereas unbiased samples are required to study the environmental effects on galaxy evolution, due to the low number density, it has been difficult to discover protoclusters without RGs or QSOs at $z > 3$.

1.3. This Thesis

It has been established that the large-scale structure of the universe is composed of various clusters of galaxies, and galaxy evolution depends strongly on the environment. However, questions remain as to the principal mechanisms of structure formation as well as galaxy evolution in clusters of galaxies. In addition to investigations of completely developed clusters in the local universe, it is essential to gain insight into the early stages of cluster formation to understand the entire history of clustering of galaxies. The number of known protoclusters is not sufficiently large to allow detailed systematic studies of cluster formation and galaxy evolution based on statistical analysis. Furthermore, so far there have been no plausible high-redshift protoclusters beyond $z = 6$; rather, only a few photometric candidates have been found. Investigating protoclusters during the epoch of reionization may also be important in understanding the early history of the universe, because reionization processes and thermal histories in overdense

regions are expected to significantly differ from those of average density, which is due to the enhanced number of ionizing sources and grater radiative feedback (e.g., McQuinn et al. 2007; Iliev et al. 2008). Since the observed excess of the galaxy number at $z \gtrsim 7$ would be altered by the topology of HII bubbles, search for protoclusters at $z \gtrsim 7$ must also be investigated from the viewpoint of reionization processes.

Here, we present a systematic survey of protoclusters at $z \gtrsim 3$ using wide-field imaging. This forms a complementary approach to protocluster research compared to previous surveys targeting at RG/QSO fields using small FoV. This survey was performed with two unique fields of the Subaru Deep Field (SDF) and the Canada-France-Hawaii Telescope Legacy Survey (CFHTLS) Deep Fields, without high-density tracers due to RGs and QSOs. In this thesis, a total of 22 protocluster candidates were identified from $z \sim 3$ to $z \sim 6$. The series of follow-up spectroscopic observations on nine of these candidates confirms the existence of four protoclusters, including the most distant protocluster at $z = 6.01$ known to data with sufficient spectroscopic confirmation. Based on this sample, we set out to address the differences in the properties between protocluster and field galaxies across cosmic time. Higher redshift protoclusters would preserve the more primitive nature of cluster of galaxies; for this reason, they are suitable targets to study the effects of the early environment on galaxy evolution.

This thesis is organized as follows. §2 describes the imaging data used in this study and our color selection of $z \sim 3-6$ galaxies. In §3, we determine the significance of the surface number density of the $z \sim 3-6$ galaxies in the overdense region, and protocluster candidates are defined by comparing theoretical model. In §4, we show our follow-up spectroscopic observations and the evidence of a protocluster. In §5, the procedure and results of SED fitting are shown. In §6, we discuss the structure and properties of the protocluster at $z \sim 3-6$. The conclusions are given in §7. We assume the following cosmological parameters: $\Omega_{\rm M} = 0.3, \Omega_\Lambda = 0.7, {\rm H}_0 = 70\,{\rm km\,s^{-1}\,Mpc^{-1}}$. Magnitudes are given in the AB system.

2. SAMPLE SELECTION

2.1. Photometric Data

2.1.1. Subaru Deep Field

We used the SDF public data, which has limiting magnitudes of $B = 28.45$, $V = 27.74$, $R = 27.80$, $i = 27.43$, and $z = 26.62$ ($2''$ aperture, 3σ). We have also obtained new, deeper R-, i'-, and z'-band images. These images were constructed by stacking all the data taken from 2001 to 2008 in the course of a study of distant supernovae (Poznanski et al. 2007; Graur et al. 2011), containing almost 30 hours worth of integration time in total. The 3σ limiting magnitudes of these new deep images are 28.35, 27.72, and 27.09 at R-, i-, and z-bands, respectively. These are about 0.5 mag deeper than the SDF public data. The SDF was observed with several optical narrow-bands; two bands of these are used in this study. They are NB921 and NB973 centered at $\lambda_c = 9196$ and 9755 Å, respectively. All seven optical images, whose response curves are shown in Figure 1, were convolved to a common seeing size of $0''.98$. The details of these image properties are summarized in Table 1.

In addition to the optical imaging, infrared imaging are conducted in the SDF. Near-infrared (NIR) images of J-, H-, K-band were taken with the WFCAM on the UKIRT (Casali et al. 2007) in March, April, and July 2010 (Hayashi et al., in prep). As shown in Figure 2, the SDF was covered by a mosaiced J-, H-, K-band image, although the depth was not uniform from field to field and the H-band images are not entirely covered the SDF. The seeing sizes of NIR images are $1''.1$. Mid-infrared (MIR) images were obtained by the Infrared Array Camera (IRAC; Fazio et al. 2004) onboard Spitzer. IRAC uses four broad-band with central wavelengths at approximately 3.6, 4.5, 5.8, and 8.0μm. The details of these NIR and MIR image properties are summarized in Table 2 and 3, respectively, and the response curves are shown in Figure 1. While the FoV of the SDF would not be large enough to find a protocluster (actually the expected number density is $\sim 1\,\mathrm{deg}^{-2}$, see Section 3.2 for detail), the SDF would, so far, be a better field to search for protoclusters at $z \sim 6$ than any other fields due to the combination of deep and wide imaging. Therefore, only i-dropout galaxies will be investigated in the SDF. Although i-dropout galaxies are basically selected from two color diagram of $i - z$ and $z - J$, i-dropout sample is selected by only $i - z$ color in this thesis because the z-band image is much deeper than the J-band image. The J-band image will be secondarily used to reject apparent contaminations by M/L/T dwarfs.

2.1.2. CFHTLS Deep Fields

In addition to the SDF, we made use of publicly available data from the CFHTLS (T0007: Gwyn 2012), which was obtained by MegaCam mounted at the prime focus of the CFHT. The Deep Fields of the CFHTLS were used in this thesis, and it consists of four independent fields, each of which has about $1\,\mathrm{deg}^2$ area ($\sim 4\,\mathrm{deg}^2$ area in total) with u-, g-, r-, i-, and z-bands. The CFHTLS Deep Fields provide two types of stacked images: one is generated using a sigma-clipped combination algorithm, and the other is using the standard median combination. Two sets of images of u-, g-, r-, i-, and z-bands are available for each type of stacked images: the

85% and 25% best seeing images. We used the 85% best seeing images stacked by a sigma-clipped combination algorithm. The four independent fields have almost same depths within $\lesssim 0.2$ mag; therefore, the CFHTLS Deep Fields are one of the suitable fields to systematically study the large scale structure in high-redshift universe. The details, such as field centers, areas, and limiting magnitudes, of each field are summarized in Table 4. The seeing size and pixel scale of all images are $\sim 0\farcs7$ and $0\farcs186$, respectively.

The CFHTLS Deep Fields are also observed in near-infrared wavelength of J-, H-, and K_s-bands by using WIRCam on CFHT, except the D2 Field's J-band which was observed with WFCAM on UKIRT. We also used the public NIR data of the WIRCam Deep Survey (WIRDS T0002: Bielby et al. 2012). The FoV of WIRCam is $21' \times 21'$, and the pixel scale is $0\farcs3$/pixel. The publicly available images were rescaled to match the pixel scale of MegaCam and have the same image size with the optical images of CFHTLS Deep Fields in order to make it easy to run SExtractor (Bertin & Arnouts 1996) in double image mode. Only the part ($\sim 50\%$) of each of the $1^\circ \times 1^\circ$ CFHTLS Deep Fields was covered by NIR imaging; therefore, the pixel count out of the NIR FoV is set to zero in order to match the image size of CFHTLS Deep Fields. Five WIRCam pointings were taken in the D1 field, nine in D2, and three in D3 and D4 fields. The total area is $\sim 2.4\,\mathrm{deg}^2$, and each field has almost uniform depth between pointings. The effective areas and the limiting magnitudes of WIRDS are summarized in Table 5. The field coverages of WIRDS are shown in Figure 3.

Table 1. Optical imaging data in the SDF

	B	V	R	i	z	NB921	NB973
3σ limiting magnitude[a] (mag)	28.57	27.85	28.35	27.72	27.09	26.67	25.56
exposure time (hour)	10	6	27	28	31	15	15

[a]The limiting magnitudes are measured with a aperture of 2 × FWHM.

Table 2. NIR imaging data in the SDF

filter	pointing	exposure time (hour)	limiting mag.[a] (3σ)			
			detector 1	detector 2	detector 3	detector 4
J	SDF1	2.5	23.86	23.88	23.97	23.76
	SDF2	10	—	24.69	24.74	—
	SDF3	9	24.74	—	—	—
	SDF4	1.1	23.30	23.24	—	—
H	SDF1[b]			No data		
	SDF2	5	—	23.94	24.13	—
	SDF3	5	24.23	—	—	—
	SDF4[b]			No data		
K	SDF1	5	23.97	23.98	23.91	23.85
	SDF2	5	—	24.13	24.12	—
	SDF3	5	24.13	—	—	—
	SDF4	0.4	22.75	22.59	—	—

Note. — The subregions overlapped with the optical FoV are shown. The numbers of pointing and detector are the same as Figure 2.

[a]The limiting magnitudes are measured with a aperture of 2 × FWHM. Since the sensitivities of the detectors are slightly different, the depth are dependent on both pointing and detector.

[b]This subregion are not observed.

Table 3. MIR imaging data in the SDF

	3.6μm	4.5μm	5.8μm	8.0μm
3σ limiting magnitude[a] (mag)	25.67	25.90	23.98	23.64
FWHM (arcsec)	2.2	2.1	2.3	2.3

[a]The limiting magnitudes are measured with a aperture of 2 × FWHM.

Table 4. Optical imaging data in the CFHTLS Deep Fields

Field	R.A. (J2000)	Decl. (J2000)	area (arcmin^2)	u^a (mag)	g^a (mag)	r^a (mag)	i^a (mag)	z^a (mag)
D1	02:25:59	−04:29:40	3063	28.12	28.32	27.77	27.30	26.39
D2	10:00:28	+02:12:30	2902	28.07	28.19	27.70	27.30	26.45
D3	14:19:27	+52:40:56	3161	28.14	28.38	27.91	27.48	26.43
D4	22:15:31	−17:43:56	3035	27.96	28.19	27.67	27.17	26.26

[a]3σ limiting magnitude in a 1.″4 aperture.

Table 5. NIR imaging data in the CFHTLS Deep Fields

Field	area (arcmin^2)	J^a (mag)	H^a (mag)	$K_s{}^a$ (mag)
D1	1764	24.91	24.60	24.63
D2	2880	24.07	24.55	24.38
D3	1404	25.03	24.87	24.66
D4	1296	25.02	24.59	24.46

[a]3σ limiting magnitude in a 1.″4 aperture.

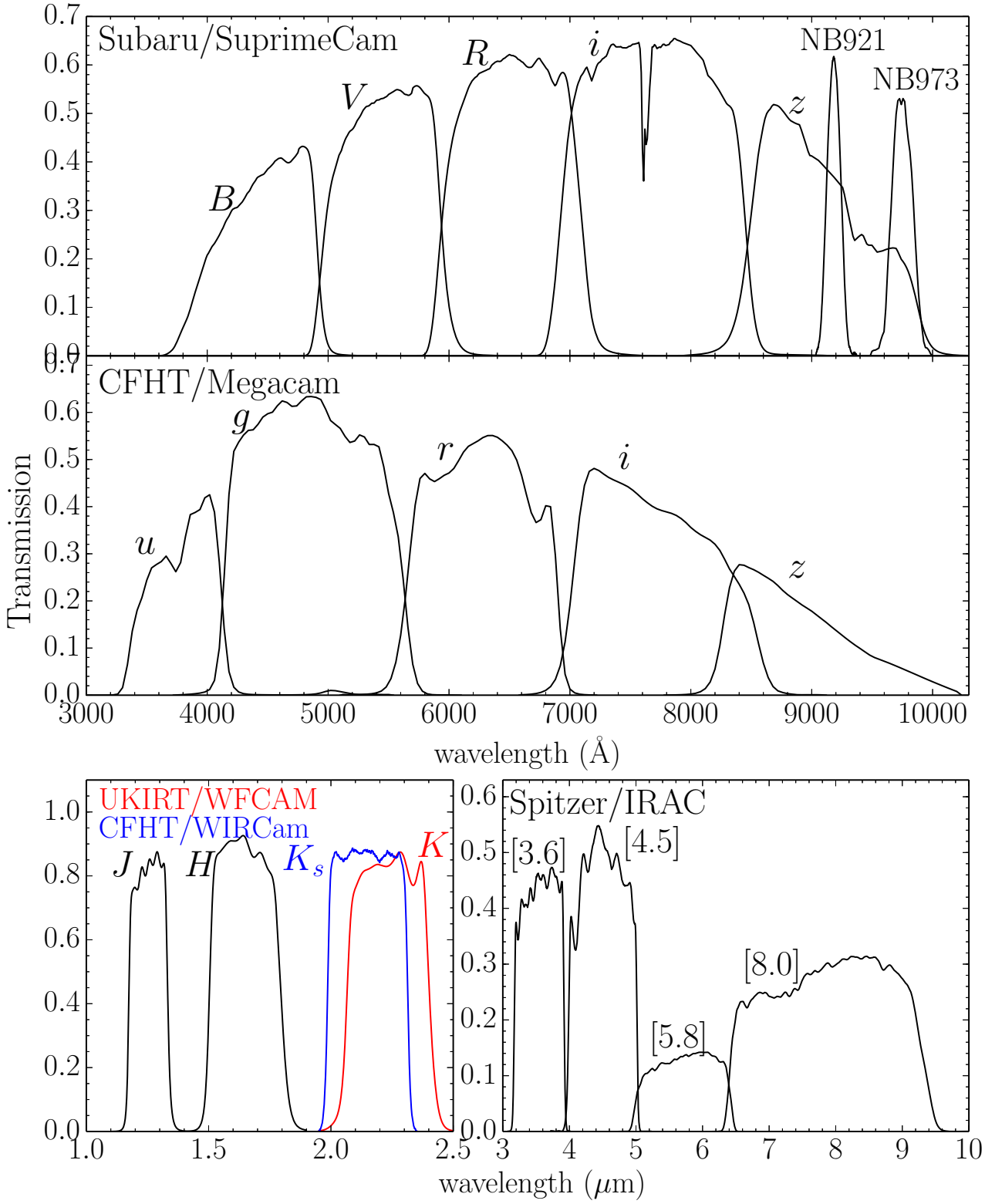

Fig. 1.— The filter transmission curves.

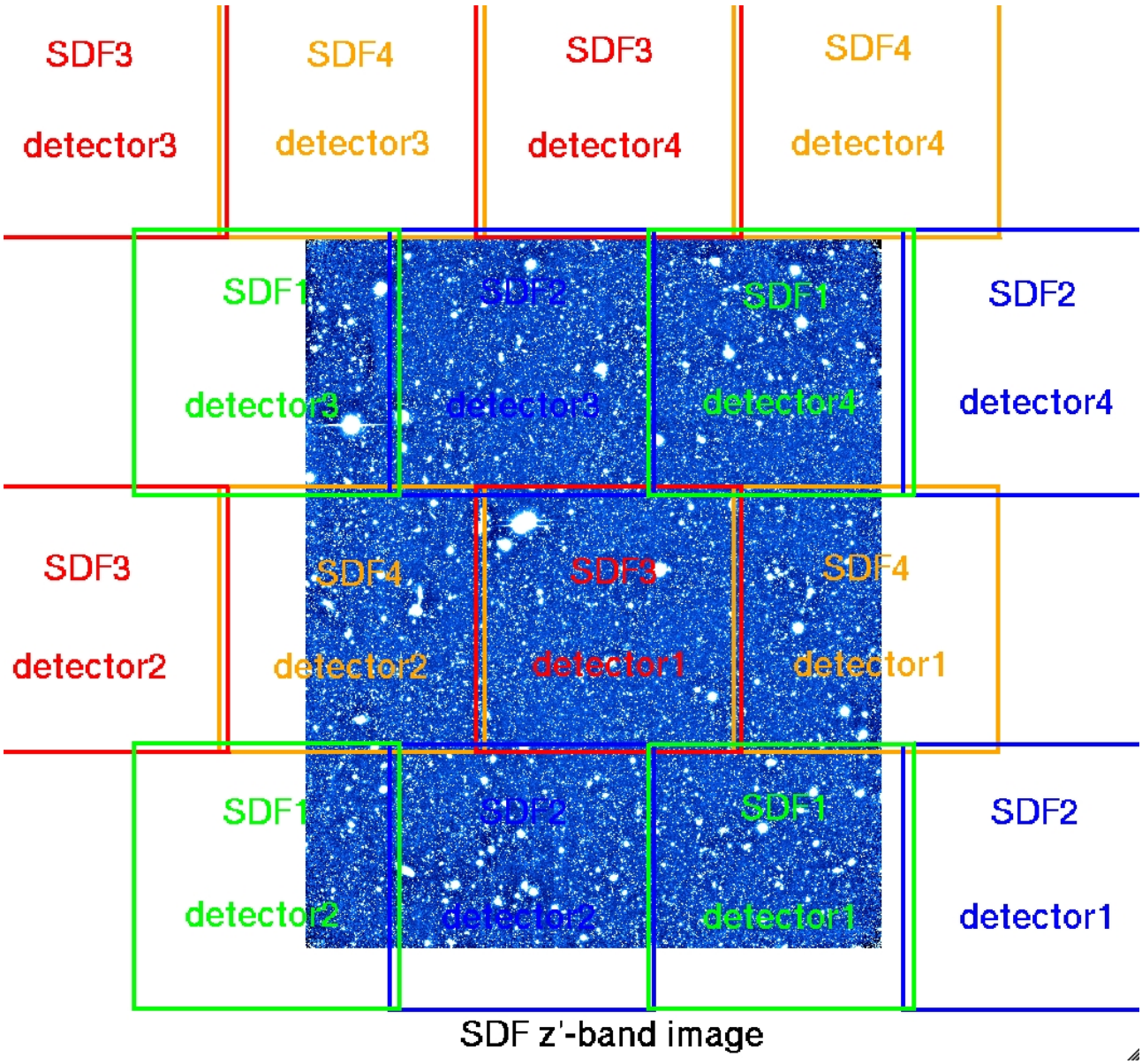

Fig. 2.— Arrangement of the individual WFCAM detectors in each pointing over the optical FoV of the SDF. Each square shows the FoV of the individual detectors, and the background image is the z'-band image.

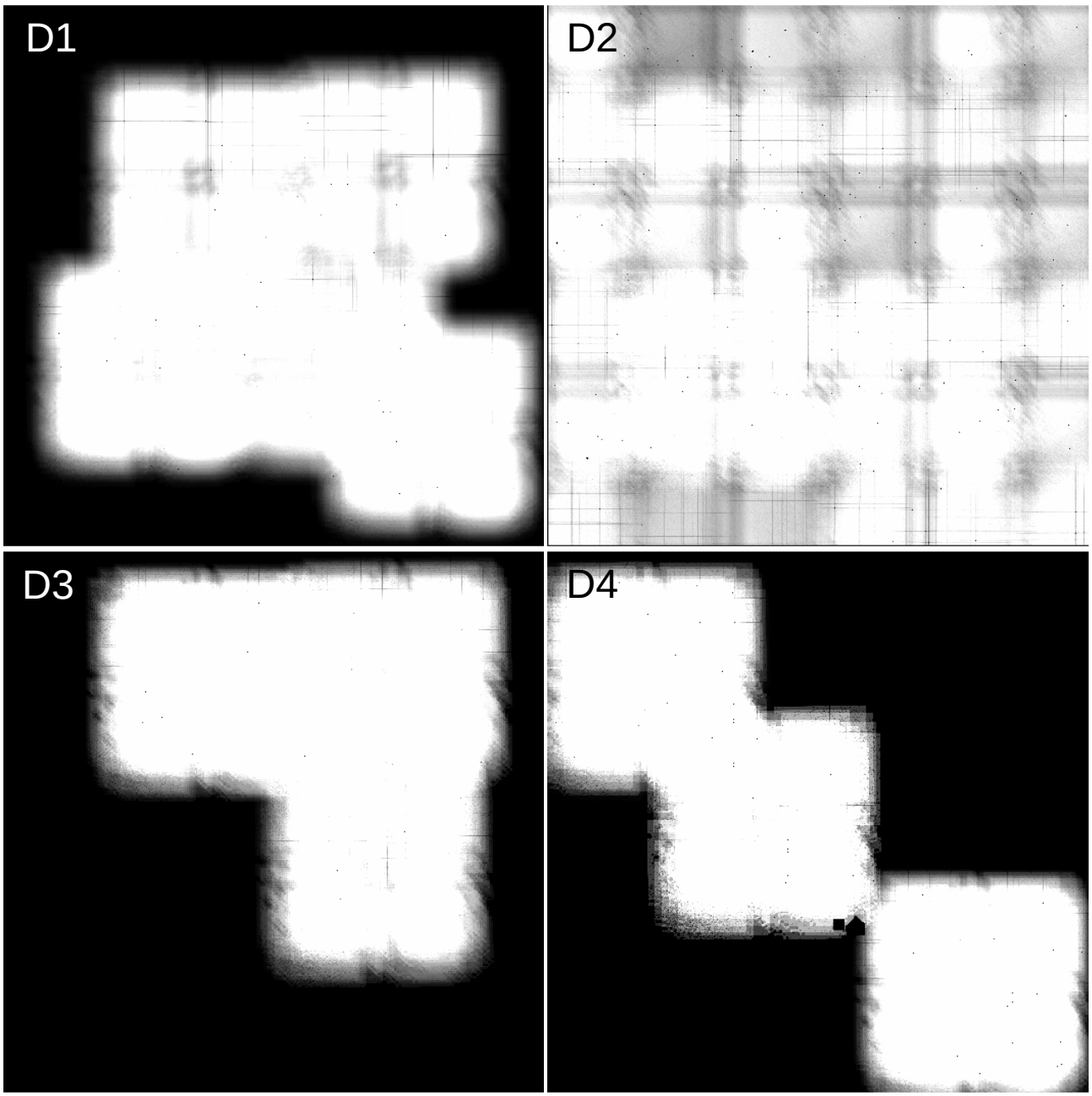

Fig. 3.— Weight maps of NIR imaging for the CFHTLS D1, D2, D3, and D4 fields.

2.2. Source Detection and Photometry

Object detection and photometry in the optical and NIR images were performed by running SExtractor with double image mode on the images. In the SDF, we will focus on i-dropout galaxies because the depth of the z-band image is much deep as shown in Table 1; thus, we will use the z-band image as a detection image. On the other hand, in the CFHTLS Deep Fields, we made i-detected catalogs for u-, g-, and r-dropout galaxies as well as z-detected one for i-dropout galaxies. We can investigate large-scale galaxy distribution from $z \sim 3$ even to $z \sim 6$ by the combination of the deep images of the SDF and the wide images of the CFHTLS Deep Fields.

In the SDF, object detections were made in the z-band, corresponding to the rest-frame wavelength of $1200-1400$ Å at $z = 6$. Then, the magnitudes, as well as photometric parameters, were measured in the other both bands at exactly the same positions and with the apertures of $2 \times$ FWHM (2.0 arcsec) as in the detection-band image. We used the task "double image mode" of the SExtractor. Objects were detected when they have five connected pixels whose signal was higher than 2σ above the sky background RMS noise. Photometric measurements were made at the 2σ level. The objects are removed when they are in the masked regions with poor image quality. These regions are around bright stars, diffraction and bleed spikes from the bright stars. The regions near the frame edges were also masked where the depths were not uniform due to the dither pattern. The remaining effective area of analysis was 876 arcmin^2. Finally, ∼102,000 objects were detected down to $z' = 27.09$ (3σ limiting magnitude).

In the CFHTLS Deep Fields, the criteria of object detection were modified in order to optimize the image quality of CFHTLS Deep Fields obtained by MegaCam. We applied a Gaussian smoothing with FWHM = 3.0 pixels to the images in order to detect faint objects. After object detection, we used unfiltered images for photometry, and objects detected in low S/N regions were removed from the catalog. In MegaCam images, stars brighter than ~ 9 mag produce a large halo, which has a radius of ~ 3.5 arcmin. This resulted in larger mask areas compared with the SDF; the effective area of the CFHTLS Deep Fields is $\sim 83\%$ of the FoV, but that of the SDF is $\sim 95\%$. Finally, ∼330,000–420,000 and 230,000–270,000 objects were listed in the i- and z-detected catalogues of CFHTLS Deep Fields down to the 3σ limiting magnitude of i- and z-bands in each field, respectively.

To estimate the detection completeness, we used the IRAF task mkobjects to create artificial objects on the original image. Artificial objects were created with the same PSF as real images, and were randomly distributed. To avoid blending artificial objects with real objects, we avoided positions close to the real objects with distances shorter than two times the FWHM of the real objects. We extracted the artificial objects using SExtractor with the same parameter set. In the z-band of the SDF, we generated 3000 artificial objects in the 23 to 29 magnitude range, and repeated this procedure 20 times. The detection completeness was more than 90% at $z' = 25$ and 70% at 3σ limiting magnitude. In the i- and z-bands of the CFHTLS Deep Fields, we generated 50,000 artificial objects in the 20–30 mag range, and extracted using SExtractor with the same parameter set. This procedure was repeated 10 times, and the detection completeness was evaluated as 70–50% at the 3σ limiting magnitude of i- and z-band in each field.

In the SDF, MIR images obtained by Spitzer/IRAC are also available. Photometry in MIR images should be performed more carefully than optical and NIR images, since PSFs in MIR

images are generally much larger than those in optical and NIR images. As a result, close objects tend to blend each other and the aperture flux of an object is likely to be contaminated by those of neighboring objects. To avoid the contamination, we conduct the following procedure to achieve an accurate photometry. First, we identified possible neighboring objects within a radius of $6\farcs0$, which corresponds to $3 \times$ FWHM of the IRAC images (Figure 4 (a)), around the targeted object in z-selected catalogue, and deblend them by using GALFIT (Peng et al. 2002). GALFIT is a software that fits 2D parametrized profile (e.g., Sérsic profile, Gaussian, and PSF) directly to the image, generating a model profile image (Figure 4 (b)) and a residual (raw − model) images. We use Sérsic profile for galaxies and PSF for stars on determining object profile in the z-band image. Then, GALFIT was rerun on each IRAC image, with the same profile parameters obtained in the z-band image. We assume that the profiles of z-band image are the same as those of the IRAC images. If close objects were too faint to fit, these objects are excluded from the fitting components in GALFIT. Finally, we obtained the residual images almost free from contamination from close objects (Figure 4 (c)). We conducted a photometry by using IRAF task phot with the aperture of $2 \times$ FWHM to measure the MIR flux of targets. Note that it would be better to use the NIR images, especially K-band, which has closer wavelength coverage to the IRAC-bands, to determine a model profile instead of the z-band image. However, the depth of the NIR images of the SDF is much shallower ($\gtrsim 1.0$ mag) than that of the MIR images, as shown in Table 2 and 3. Therefore, re-fitting in MIR images was sometimes failed based on the same profile parameters with the z-band image, especially using Sérsic profile, which has more fitting parameters (e.g., half-light radius, Sérsic index, and position angle) than PSF. In this case, we used PSF fitting instead of Sérsic profile fitting.

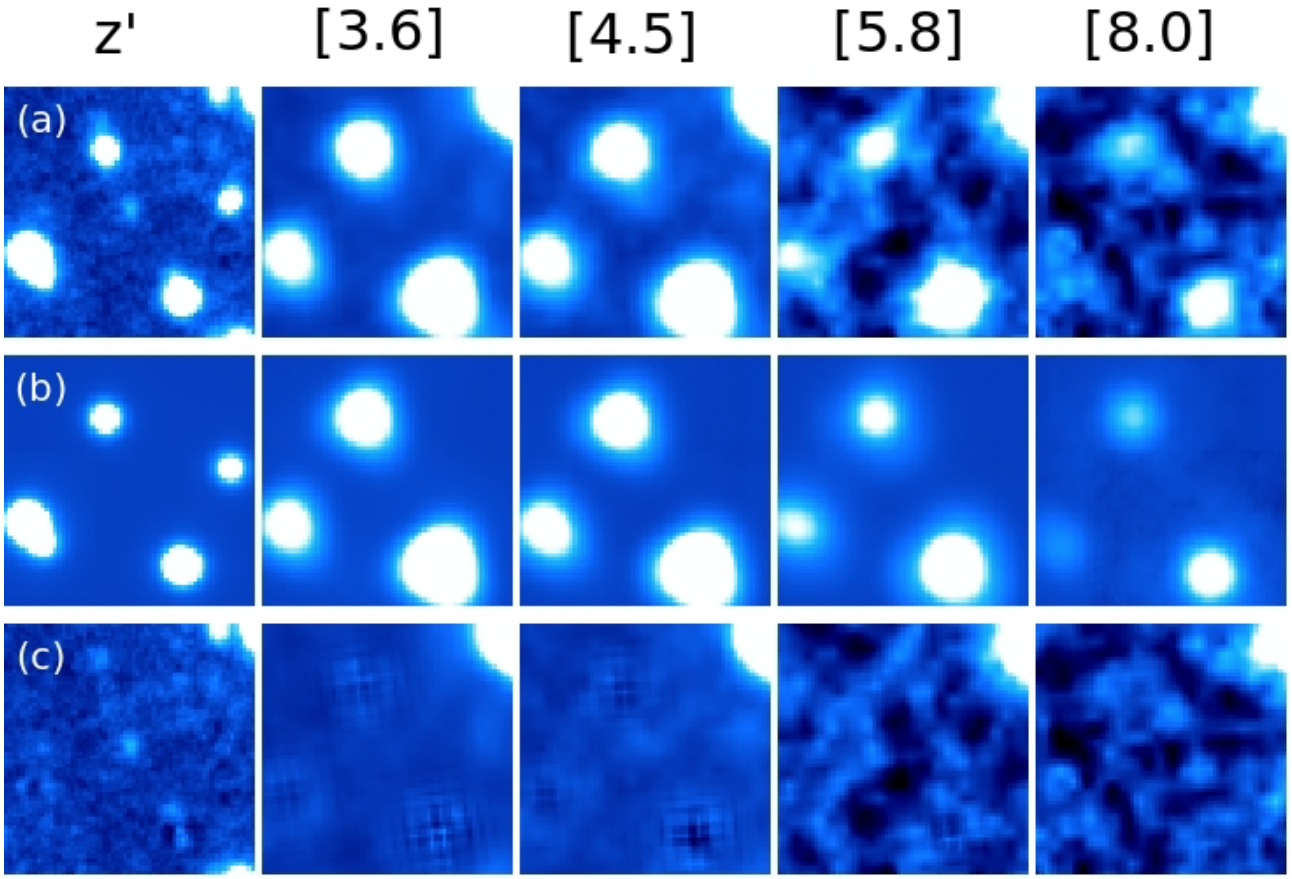

Fig. 4.— The example of the removing contamination. (a) Raw images, (b) model images simulated by GALFIT, and (c) residual images in z', [3.6], [4.5], [5.8], and [8.0], respectively. The FoV of each panel is $12'' \times 12''$.

2.3. Selection Criteria of Lyman Break Galaxies

We selected high-redshift galaxy samples by using Lyman break technique. This technique makes use of two color diagram to distinguish high-redshift galaxies from low-redshift galaxies and dwarf stars since high-redshift galaxies have unique spectral feature of Lyman break, which is caused by intergalactic medium (IGM) absorption. The selection criteria of u-, g-, r-, and i-dropout galaxies are followings (van der Burg et al. 2010):

$$
\begin{aligned}
u-\text{dropout} &: 1.0 < (u-g) \wedge -1.0 < (g-r) < 1.2 \wedge 1.5(g-r) < (u-g) - 0.75, \\
g-\text{dropout} &: 1.0 < (g-r) \wedge -1.0 < (r-i) < 1.0 \wedge 1.5(r-i) < (g-r) - 0.80 \wedge u > m_{\mathrm{lim},2\sigma}, \\
r-\text{dropout} &: 1.2 < (r-i) \wedge -1.0 < (i-z) < 0.7 \wedge 1.5(i-z) < (r-i) - 1.00 \wedge u, g > m_{\mathrm{lim},2\sigma}, \\
i-\text{dropout} &: (i-z) > 1.5 \wedge u, g, r > m_{\mathrm{lim},2\sigma} \text{ in the CFHTLS } (B, V, R > m_{\mathrm{lim},2\sigma} \text{ in the SDF}),
\end{aligned}
$$

where $m_{\mathrm{lim},2\sigma}$ is a 2σ limiting magnitude. These selection criteria of u-, g-, and r-dropout galaxies are shown on two color diagrams of Figure 5. As shown in this figure, the possible contamination of dropout selection, such as low-redshift elliptical galaxies having strong 4000Å/Balmer break and dwarf stars, are effectively separated from high-redshift galaxies according to those criteria. Based on these criteria, for u-, g-, and r-dropout galaxies, we used i-band detected catalogues down to the 3σ limiting magnitude, and z-band detected one for i-dropout galaxies. The number and number counts of dropout galaxies in each field are shown in Tabel 6 and Figure 6, respectively.

We estimated redshift distribution of these dropout galaxies by using the population synthesis model code GALAXEV (Bruzual & Charlot 2003) and IGM absorption (Madau 1995). The estimate of IGM absorption relies on the distribution function of intergalactic absorbers of Lyα forest, Lyman-limit systems, and damped Lyα systems. It should be noted that, although we employed Madau's model to estimate IGM attenuation in this thesis, some works proposed updated distribution functions based on recent observations (Meiksin 2006; Inoue et al. 2014). In GALAXEV, we simulated a large variety of galaxy spectral energy distributions (SEDs) using the Padova 1994 simple stellar population model. We assumed a Salpeter (1955) initial mass function (IMF) with lower and upper mass cutoffs $m_L = 0.1\,\mathrm{M}_\odot$ and $m_U = 100\,\mathrm{M}_\odot$, two metallicities (0.2 and $0.02\mathrm{Z}_\odot$), and two types of star formation history of instantaneous burst and constant. We extracted model spectra with ages between $\sim 5\,\mathrm{Myr}$ and $500\,\mathrm{Myr}$ and applied the reddening law of Calzetti et al. (2000) with $E(B-V)$ between 0.0 and 1.0. The expected colors of high-redshift galaxies are estimated by convolving these simulated SEDs with filter transmission curves. The redshift distribution of u-, g-, r-, and i-dropout galaxies, applying our dropout selection criteria to these simulated galaxy catalogue are shown in Figure 7. The redshift evolution tracks of these simulated young star-forming galaxies are shown in Figure 5.

We evaluated the contamination rate for these color-selection criteria. The sources of the majority of the contamination were dwarf stars and old elliptical galaxies, the latter being possible to satisfy the color criteria due to the 4000Å/Balmer break. To estimate the contamination rate of dwarf stars, we use the TRILEGAL galactic model (Girardi et al. 2005). Since this model enables us to set up various structural parameters of thin disc, thick disc, halo, and bulge, we used exponential disk model with default values of scale length and height, and Cahbrier's IMF was applied. The galactic latitudes were set to be the same as the observations ($|b| = 82^\circ$ in the SDF, $|b| \sim 50^\circ$ in the CFHTLS Deep Fields). Then, photometry of simulated dwarf stars was calculated with CFHT/Megacam's filter set. These simulated dwarf stars are

plotted in Figure 5 as green dots. Next, we simulated old galaxy SEDs using the GALAXEV, assuming two relatively high metallicities ($Z_\odot$ and $2.5Z_\odot$), and extracted model spectra with age of $1 - 32$ Gyr. The redshift evolution tracks of these simulated old galaxies are also plotted in Figure 5. As shown in this figure, the redshift tracks of old galaxies are away from all dropout selection regions. And, although a few dwarf stars are located only in the r- and i-dropout selection regions, the main locus of dwarf stars lie far from these regions. Actually, the contamination rate of dwarf stars in r-dropout samples is expected to be $2.2 - 7.8\%$ depending on the galactic latitude of the CFHTLS Deep Fields ($|b| = 40 - 60^\circ$), and the contamination rate in i-dropout samples is $3.4 - 6.4\%$ in the CFHTLS Deep Field and 1.9% in the SDF, whose galactic latitude is $+82^\circ$. Practical contamination rate would be slightly higher due to the photometric errors, as discussed later. Based on these simulation of dwarf stars and old galaxies, the dropout selection criteria used in this thesis are confirmed to be able to separate high-redshift galaxies from contaminations.

In addition to this estimate based on model predictions of dwarf stars and old galaxies, we checked the estimated contamination rate by comparing with observational works. According to the ERO catalogue by Miyazaki et al. (2003), few EROs can meet our dropout selection criteria, since the criterion of non-detection in shorter wavelength bands is effective to remove low-redshift galaxies. Actually, Malhotra et al. (2005) show that i-dropout objects with $i - z > 1.3$ do not include any EROs based on their spectroscopy. As for the contamination of dwarf stars, some dwarf stars can satisfy our dropout selection criteria based on the dwarf star catalogue by Hawley et al. (2002). Furthermore, from the combination of the star count model developed by Nakajima et al. (2000) and the luminosity function of dwarf stars from Gould et al. (1996); Zheng et al. (2001, 2004), the contamination rates are only about $1 - 6\%$ at the galactic coordinates corresponding to our survey area. These contamination rates were found to be almost consistent with model predictions. Only for the SDF, J-band data is available in whole optical survey area though it is shallower than the optical images. According to Hawley et al. (2002), dwarf stars having $i - z > 1.5$ should have a very red color in NIR wavelength ($z' - J \gtrsim 2$); therefore, typical dwarf stars can be detected even in the shallow J-band image. Therefore, we additionally imposed the criterion of $z - J < 0.8$ only on i-dropout objects detected in J-band. This would make contamination rate in i-dropout sample smaller. Based on these consideration, we assumed a contamination rate in our dropout selection of up to a few percent, mainly consisting of contamination from dwarf stars. In the subsequent analyses and discussions, we ignore the possible contamination by low-redshift galaxies.

Finally, we estimated the contamination rate resulted from photometric noise, which may scatter even lower-redshift sources to satisfy our dropout selection criteria, in addition to above intrinsic contaminations. We performed the following simple simulation, as same as in Wilkins et al. (2011a) and Bouwens et al. (2011b), to estimate the contamination rate due to the photometric noise. We first randomly choose brighter objects, and dim these bright source so as to match the magnitudes of our dropout samples by scaling the flux, then distribute these artificial objects on the original image using IRAF task mkobjects. We here assume faint objects have the same color distributions as that of bright objects whose photometric noise should be negligible. We extracted the artificial objects using SExtractor and impose our color criteria of dropout galaxies. The number of artificial objects in a given magnitude interval was chosen to be the same as the observed number of object in the same magnitude interval. We finally found $\sim 5 - 10\%$ contamination rate in u-, g- and r-dropout samples and $\sim 15 - 20\%$ in i-dropout

samples. Since the total number of i-dropout galaxies are much smaller ($N_i \sim 200$) than those of u-, g-, and r-dropout galaxies ($N \sim 10^3 - 10^4$), even a few contaminations of photometric noise have a large effect on the contaminatin rate of i-dropout galaxies. It should be noted that these contaminants appeared almost randomly over the image in the repeated simulation, suggesting the contamination rate is homogeneous over the survey field and did not change the overdensity significance estimated in the next section.

Table 6. Number of dropout galaxies

Field	area (arcmin^2)	N_u	N_g	N_r	N_i
D1	3063	17110	10416	2433	148
D2	2902	14515	11160	2539	231
D3	3161	21454	14896	2579	232
D4	3035	10484	11288	1926	188
SDF	876	–	–	–	258

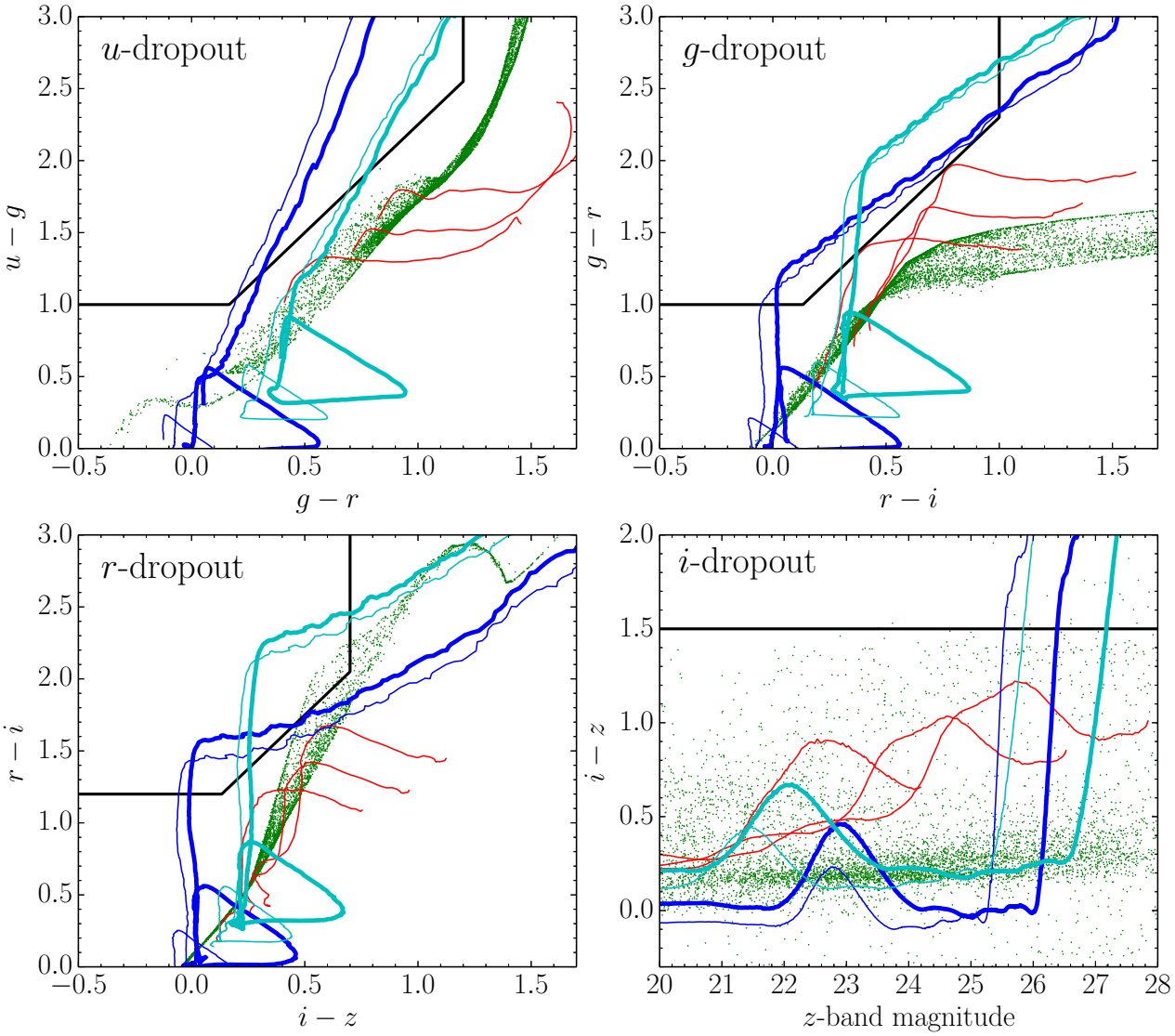

Fig. 5.— Demonstration of dropout galaxy selection on two color and color-magnitude diagrams. Thick black lines show the borders of dropout galaxy selection, and blue and cyan lines indicate redshift evolution tracks of young star-forming galaxies like LBGs (thin blue: age = 10 Myr and E(B − V) = 0.1, thick blue: age = 250 Myr and E(B − V) = 0.1, thin cyan: age = 10 Myr and E(B − V) = 0.4, and thick cyan: age = 250 Myr and E(B − V) = 0.4). Three red lines are redshift evolution tracks of elliptical galaxies at $z \sim$ 0-1.5 with ages of 1, 7, and 22Gyr, and green dots are dwarf stars estimated by the TRILEGAL galactic model (Girardi et al. 2005). Note that redshift evolution tracks in the i-dropout panel can shift horizontally depending assumption of stellar mass since the x-axis of the i-dropout panel is magnitude not color.

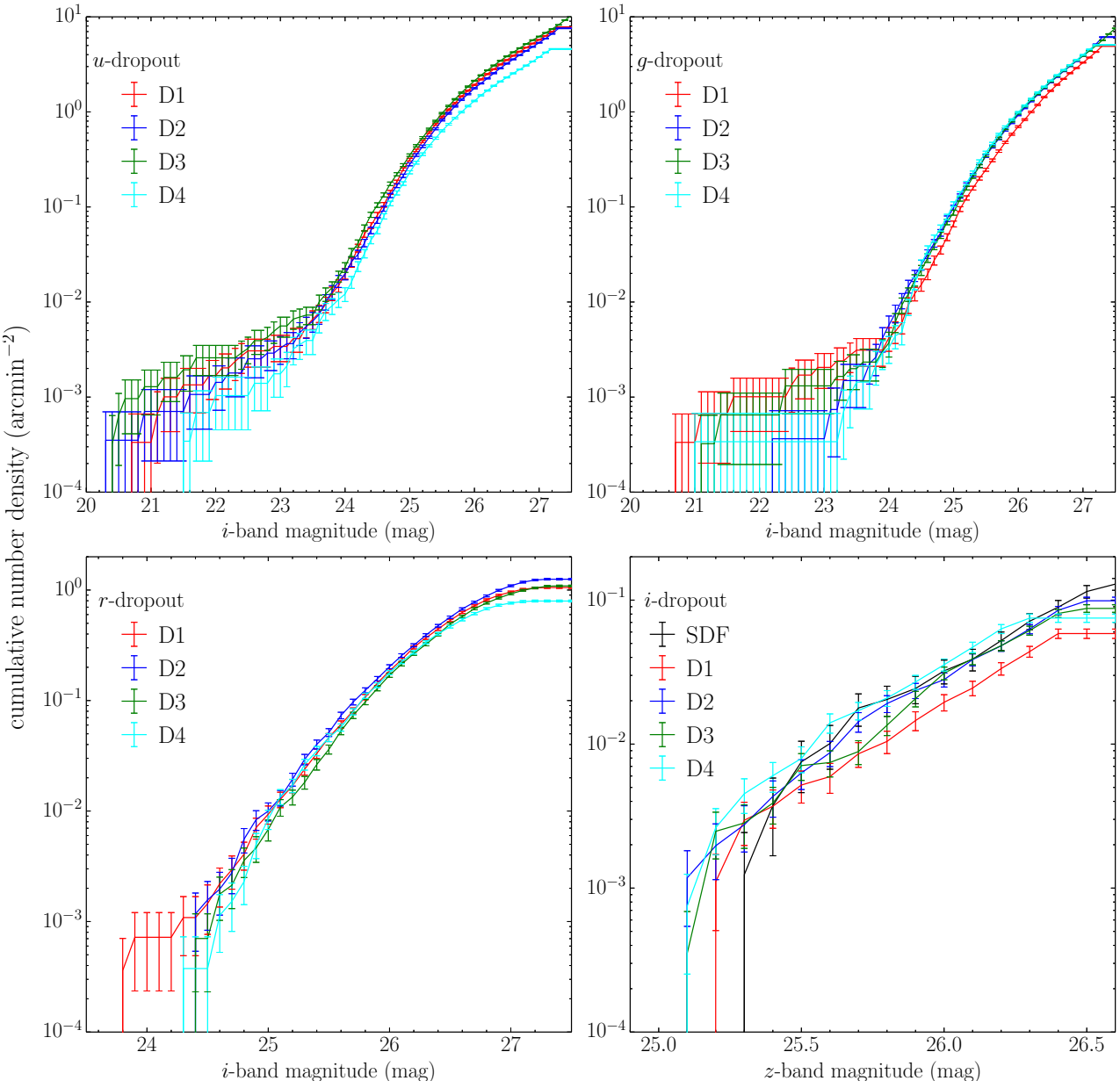

Fig. 6.— Cumulative number counts of the u-, g-, r-, and i-dropout galaxies. The detection completeness was corrected. Although, in the SDF, i-dropout galaxies were selected down to the 3σ limiting magnitude of 27.09 mag, the drawing range of z-band is limited to 26.5 mag in order to make it clearer to check consistency between the SDF and the CFHTLS.

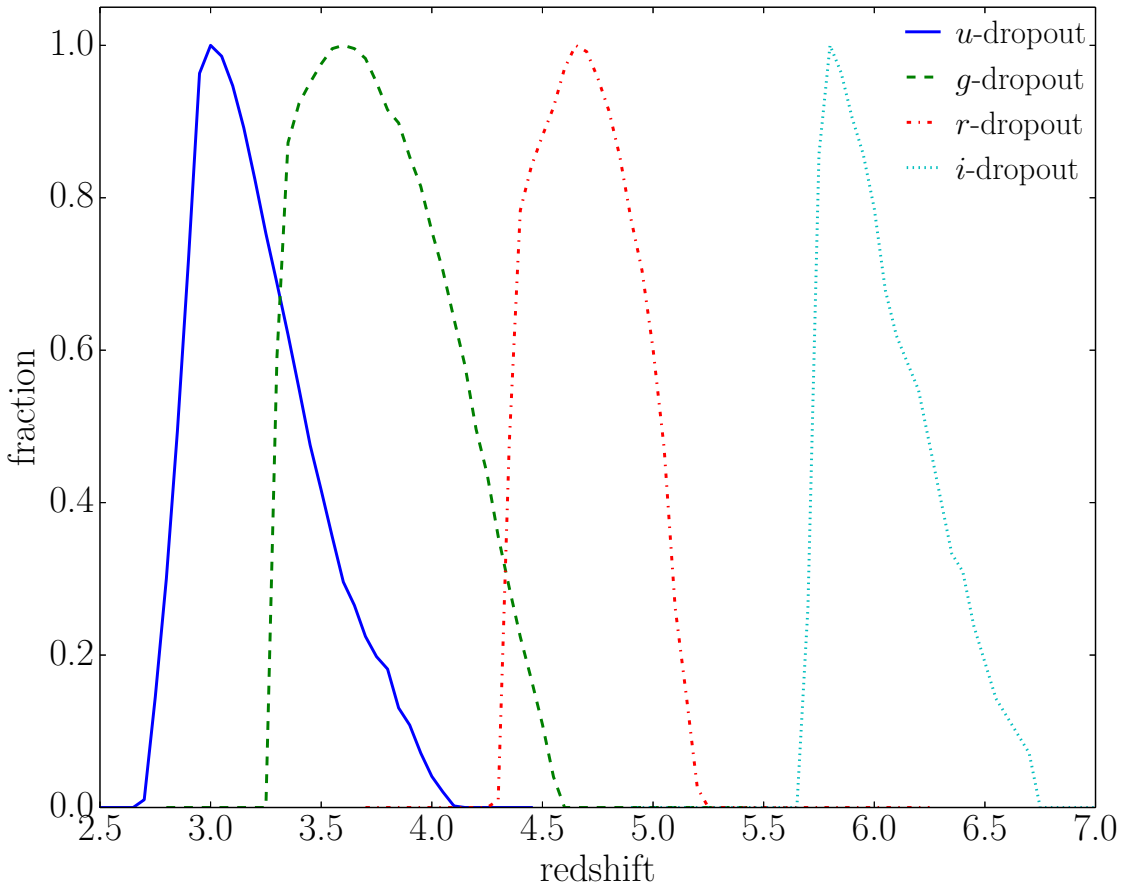

Fig. 7.— Expected redshift distribution of u-, g-, r-, and i-dropout galaxies.

3. PROTOCLUSTER CANDIDATES

3.1. Sky Distribution and Overdensity

There are various methods to quantify galaxy distribution and clustering in the literature. Although spectroscopic observations would be the most direct and accurate methods to reveal three-dimensional structure of galaxies, they usually require a lot of telescope time. It is also suffers from incompleteness in a redshift space due to OH sky emissions and bias to easily identified emission line galaxies. To overcome these problems, many methods to use projected two-dimensional distributions of galaxies have been proposed. In the local universe, many effective methods are available based on rich data sets, such as tests of the asymmetry, the angular separation, and density contrasts of the structure (West et al. 1988), the adaptive-kernel based DEDICA algorithm (Pisani 1993, 1996; Ramella et al. 2007), the average two-point correlation function statistic (Salvador-Sole et al. 1993), and wavelet analysis (Flin & Krywult 2006). Using N-body simulation of dark matter, Aragón-Calvo et al. (2007) have proposed the multiscale morphology filter to identify cosmic web and to extract galaxy distribution. While there are many sophisticated methods to quantify structures in the local universe, they are almost impossible to apply to the high-redshift universe where most of faint galaxies would be missed, and even if galaxies were detected down to faint end, its survey area is usually too small.

Simple methods to measure the local number density are commonly used to define environments in the high-redshift universe: defined by the separation from Nth nearest neighbour or the number of galaxies in a fixed aperture. Muldrew et al. (2012) have studied these two methods' advantage and disadvantage by using mock galaxy catalogue. Nearest neighbour method probes the internal properties of the halo, when neighbour number, N, is small enough. In contrast, fixed aperture method can probe the halo as a whole: larger overdensity values indicate that massive halos are embedded. The comparison between nearest neighbour and fixed aperture methods were expanded to higher redshift by Shattow et al. (2013). They have found that nearest neighbour method tends to show larger scatter in the correlation between projected real (three-dimensional) overdensity. Fixed aperture method indicates better correlation between projected overdensities at $z = 2$ and real overdensity at $z = 0$.. From these considerations, fixed aperture method would be better to search protoclusters.

Based on the dropout samples described in Section 2.3, we have estimated the local surface number density by counting dropout galaxies within a fixed aperture in order to determine the overdensity significance quantitatively. A radius of a aperture has to be properly set according to the spatial scale of protoclusters. In the local universe, typical value of R_{200} for X-ray clusters is 0.5 Mpc. This indicates that, at least, > 0.5 Mpc radius is required to enclose most of protocluster members since it is expected that the distribution of protocluster members is wider than that of local clusters based on hierarchical structure formation model. On the other hand, Aragón-Calvo et al. (2010) have predicted that galaxies are falling on clusters non-spherically through the filaments of cosmic web; thus, too large aperture will wash out the overdensity signal of protoclusters. Chiang et al. (2013) have estimated the typical radius of protoclusters at $2 \lesssim z \lesssim 5$ by using the combination N-body simulation (Springel et al. 2005) and the semi-analytic galaxy formation model (Guo et al. 2011). Their defined radius corresponds to the size in which about 65% of the mass in bound halos and 40% of total

mass of protocluster are included. Although it is based on the three-dimensional distribution of protocluster galaxies, this would be a good guide to determine a radius to calculate local surface number density. The radius of $\sim 0.8 - 1.0$ physical Mpc at $2 \lesssim z \lesssim 5$ is expected to be almost consistent with the typical size of progenitors of $> 10^{14}\,M_{\odot}$ halos.

In this study, for u-, g-, and r-dropout galaxies, the radius of 0.75 physical Mpc was used, which corresponds to 1.6, 1.8, and 1.9 arcmin, respectively. The same radius (2.1 arcmin) is used for i-dropout galaxies in the SDF. On the other hand, we used slightly larger radius of 1.0 physical Mpc (2.9 arcmin) for i-dropout galaxies in the CFHTLS Deep Fields, whose z-band images are > 0.5 mag shallower than that of the SDF, because small number density within an aperture would cause large Poisson error. These apertures were distributed over the CFHTLS Deep fields and the SDF in a grid pattern at intervals of ~ 20 arcsec. In masked regions, the local surface number density was assumed to be the same as the mean surface number density. Based on the mean and the dispersion, σ, of the number of dropout galaxies in an aperture, surface number density contours of u-, g-, r-, and i-dropout galaxies in the CFHTLS Deep Fields are plotted in Figure 8, 9, 10, and 11, respectively. Figure 12 is for i-dropout galaxies in the SDF. Although we can find some overdense regions in the CFHTLS Deep Fields and the SDF, it is not easy to find plausible protocluster candidates since the large redshift uncertainty, which is $\Delta z \sim 1$ ($\sim 230 - 60$ physical Mpc at $z \sim 3.1 - 6.0$), of dropout technique dilutes the clustering signal in two-dimensional space. The overdensity resulted from the real protoclusters could be weakened by fore/background galaxies; on the other hand, the alignment of the large-scale structure, such as filaments, would make high significance of surface overdensity by chance. Therefore, we will compare our results with theoretical predictions to understand the relation between surface overdensity and the probability to include real protoclusters in the following subsection.

At first, we check the dependence of overdensity contrast on the aperture sizes. We re-calculated local surface number density of u-, g-, and r-dropout galaxies in the CFHTLS Deep Fields with the radii of 0.5, 1.0, 1.5 physical Mpc, instead of 0.75 physical Mpc. Even using the smallest radius of 0.5 physical Mpc for r-dropout galaxies, large enough number of r-dropout galaxies are included in an aperture (average number in an aperture is about three or four). We found that $> 4\sigma$ overdense regions identified by using the radius of 0.75 physical Mpc remained as the highest overdensity regions even if the aperture radius was changed, though the peak of overdensity significances slightly fluctuated between $\sim 3\sigma$ and $\sim 5\sigma$. As for i-dropout galaxies, although it was difficult to replace with smaller radius due to low number density, highest overdense regions with more than 6σ kept as the highest overdensity region. Second, we also check the robustness of the overdensity estimate on the color selection criteria of i-dropout galaxies. As described in Section 2.3, i-dropout samples could include non-negligible contaminations due to the photometric noise. The overdensity significances were re-calculated by using i-dropout samples when changing the $i - z$ color criterion from 1.3 to 1.7 in the SDF, and from 1.3 to 1.5 in the CFHTLS Deep Fields because the number of i-dropout galaxies selected by $i - z > 1.7$ in the CFHTLS Deep Fields is too small to investigate sky distribution quantitatively. Two (in the SDF and CFHTLS Deep 3) of three overdense regions with more than 6σ significance were still significant overdense regions even changing the selection criteria, while the other overdense region found in the CFHTLS D1 was lost its highest significance. Although the 6σ overdense region in the CFHTLS D1 may be caused by chance due to serious contaminations, most of overdense regions kept their high overdensity even with $i - z > 1.3$ and 1.7. Since the contam-

ination rate of photometric noise strongly depends on $i - z$ color criterion, this result can be interpreted that overdensity significance would not be largely affected by the contamination. From these two checks, therefore, the overdensity significance can be statistically robust.

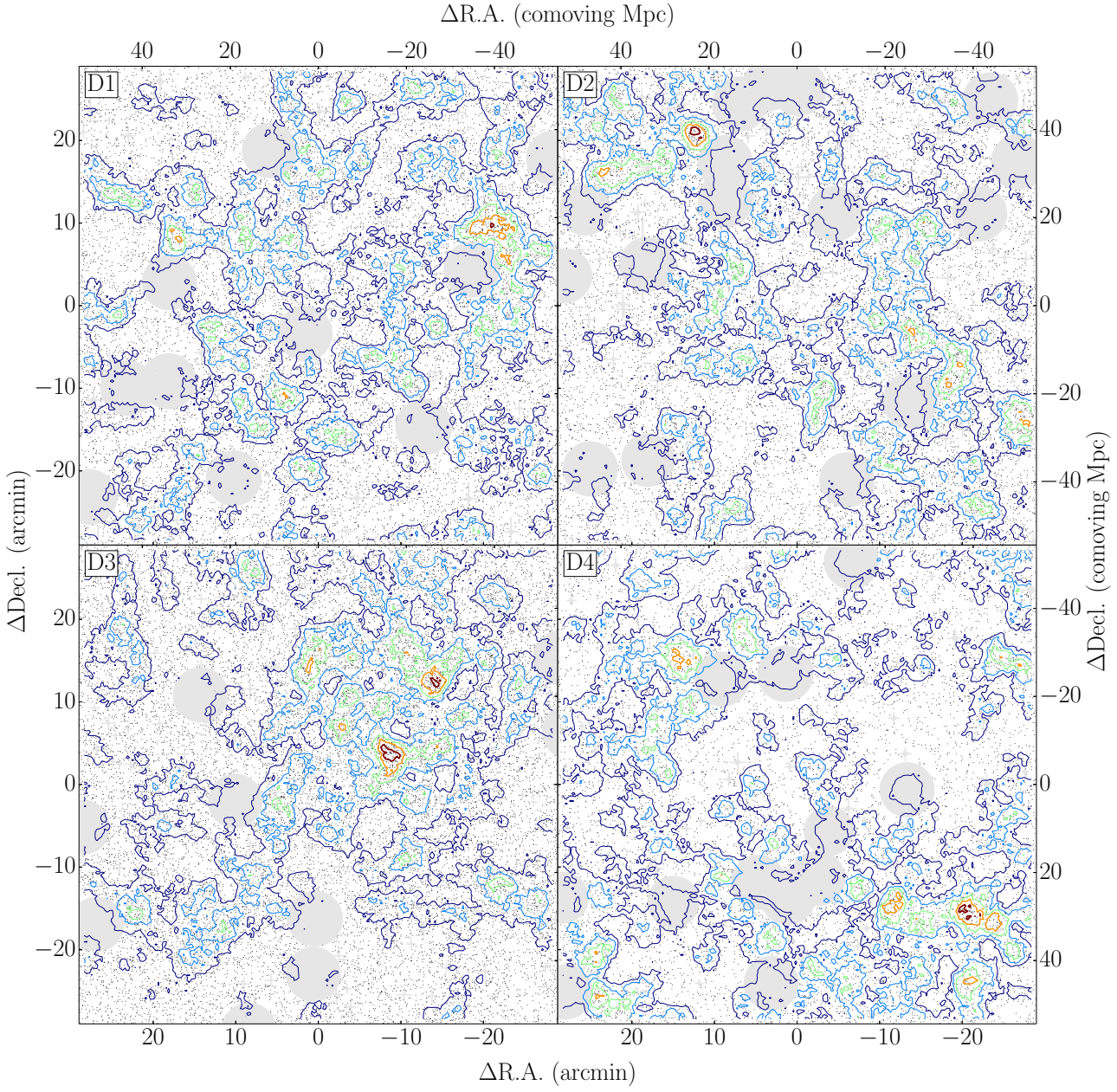

Fig. 8.— Sky distribution of u-dropout galaxies (dots) with surface number density contours (lines) in the D1 (upper left), D2 (upper right), D3 (lower left), and D4 (lower right) field. The lines correspond to contours of surface overdense significance from 4σ to 0σ (mean) with a step of 1σ. North is up, and east is to left. The comoving scale projected to $z = 3.1$ is shown along the axes, and masked regions are also shown by gray region.

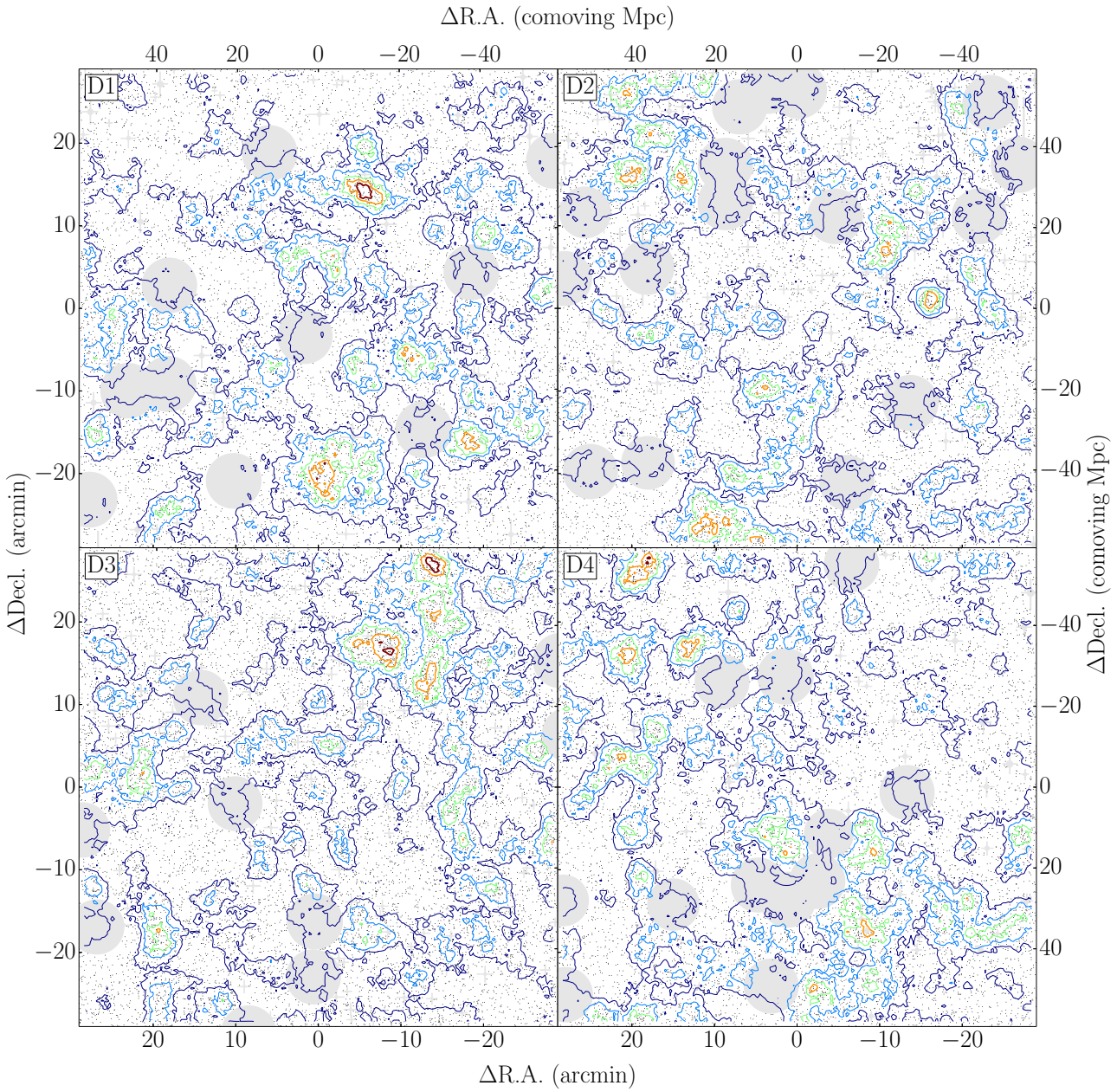

Fig. 9.— Same as Figure 8, but for the g-dropout galaxies.

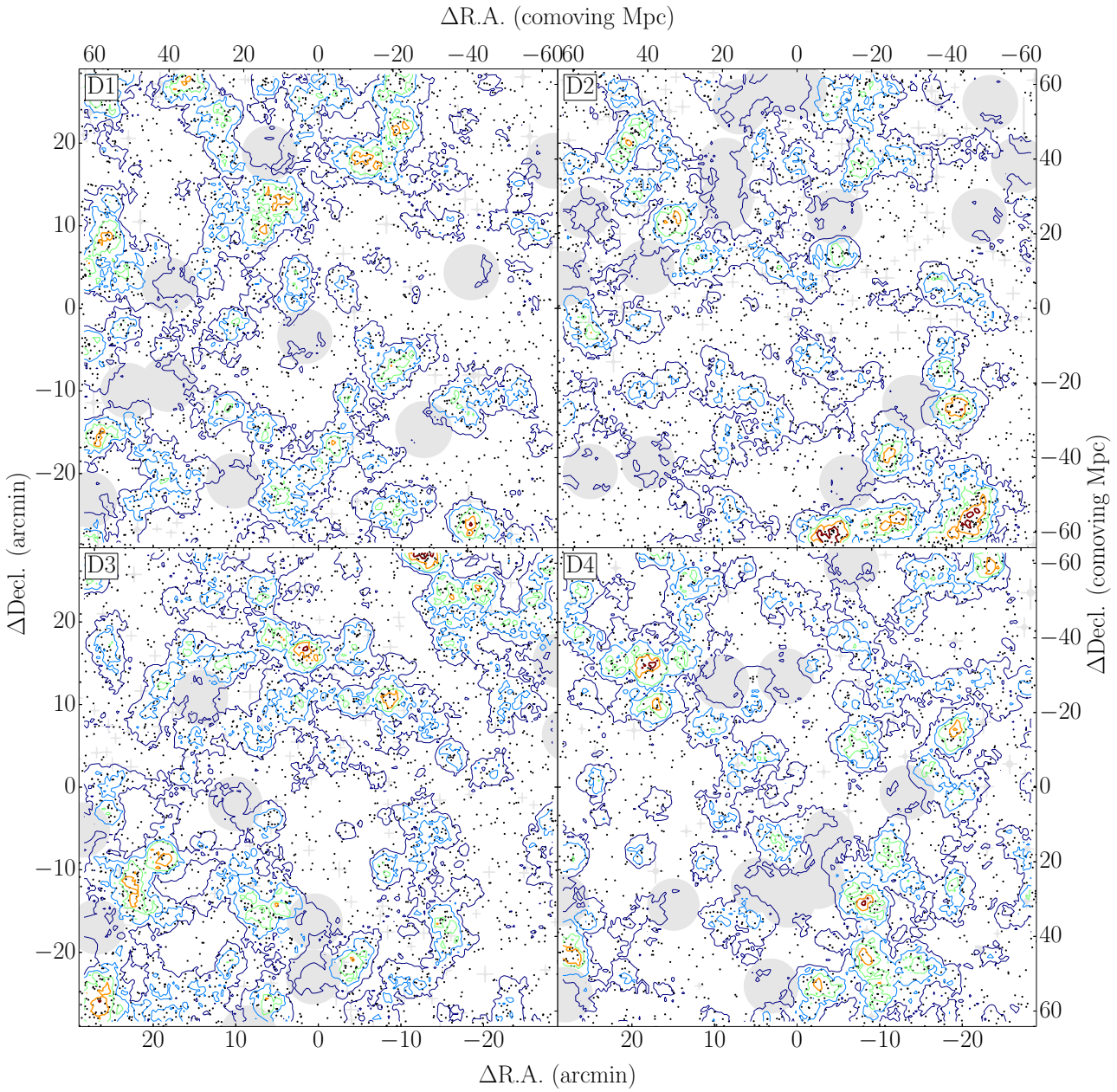

Fig. 10.— Same as Figure 8, but for the r-dropout galaxies.

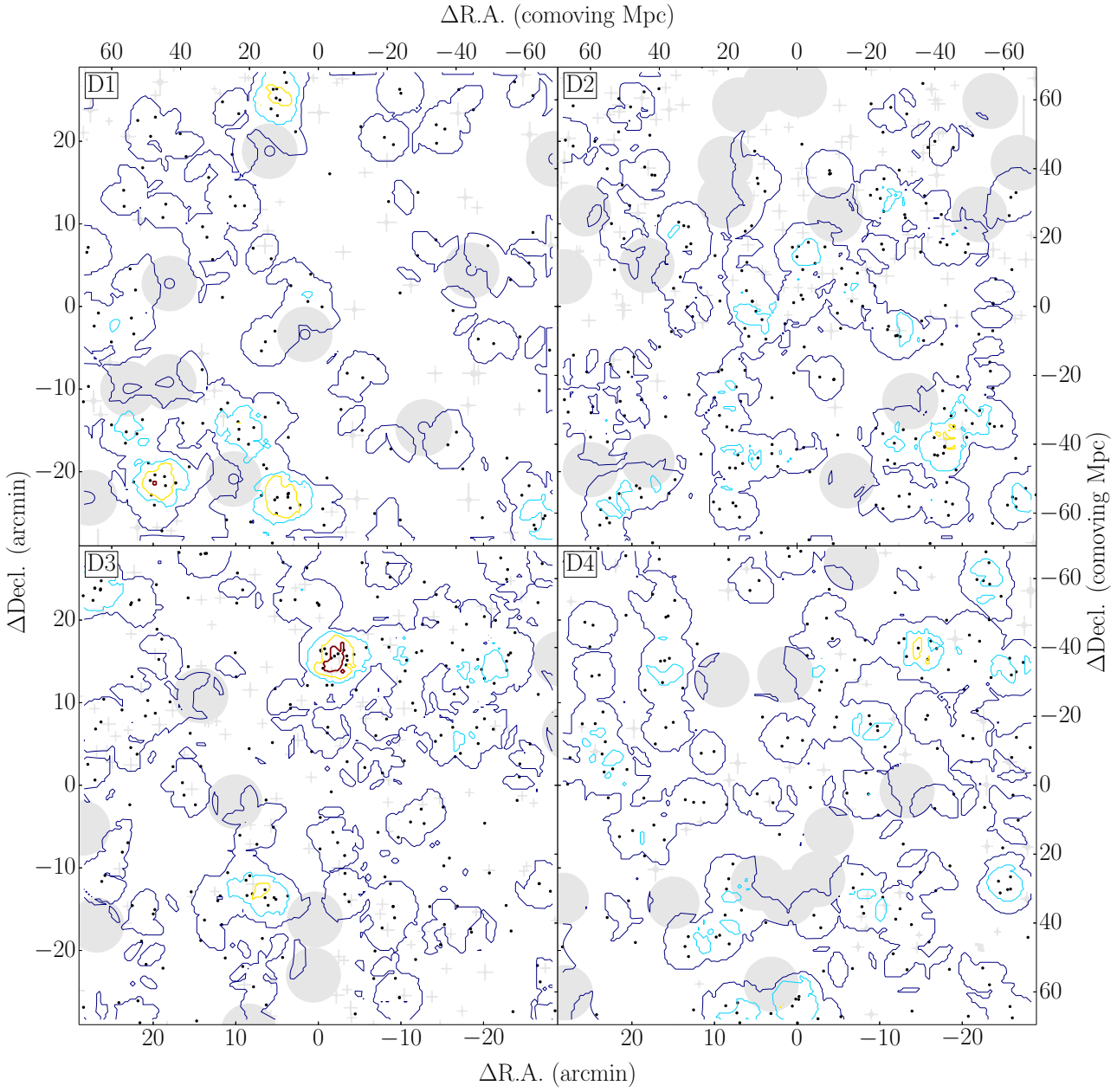

Fig. 11.— Same as Figure 8, but for the i-dropout galaxies in the CFHTLS Deep Fields, and the lines show overdensity significance from 6σ to 0σ (mean) with a step of 2σ.

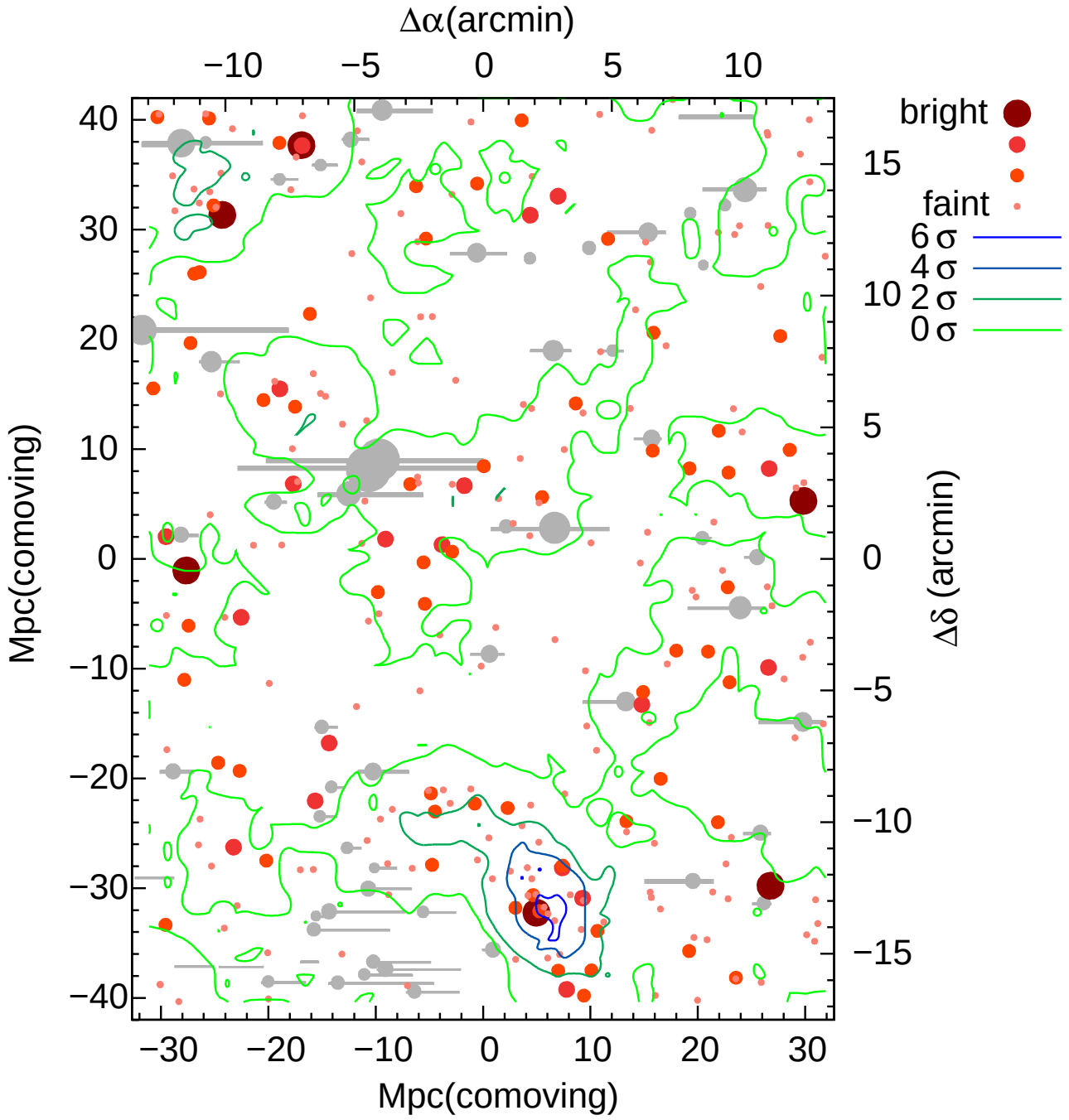

Fig. 12.— Sky distribution of i-dropout galaxies in the SDF, with surface number density contours. i-dropout galaxies are represented by filled circles whose size is proportional to the z-band magnitude.

3.2. Comparison with Model Predictions

We found statistically significant overdense regions from $z \sim 3$ to $z \sim 6$, but are these regions really protoclusters? And, how massive dark matter halo they will evolve into at $z = 0$? To answer these questions, it is necessary to compare our observations with theoretical predictions about the descendants of high redshift overdensities by tracing hierarchical merging histories. Overzier et al. (2009a) and Chiang et al. (2013) investigated the relation between galaxy overdensity at high redshift and dark matter halo mass at $z = 0$ by using a combination of N-body dark matter simulations and semi-analytic galaxy formation models. They systematically studied cluster development from $z \sim 5$ to $z = 0$ and found clear correlations between overdensity at high redshift and halo mass at $z = 0$, depending on e.g., the sample selection, search volume, and redshift accuracy of the tracer galaxies, as well as the mass of the clusters. Here, we perform a new simulation specifically designed to match the observational details of our dropout galaxy survey as closely as possible. The simulation specific to our sample is important because we used u-, g-, r-, and i-dropout galaxy selection, which is different from Chiang et al. (2013). We connect directly the observed quantity, the significance of the overdensity of the surface number density, to the dark matter halo mass at $z = 0$.

We used the light-cone model made by Henriques et al. (2012). A brief outline of the construction of light-cone models is presented below. First, the assembly history of the dark matter halos was traced using an N-body simulation (Springel et al. 2005), in which the length of the simulation box was $500\,h^{-1}\,\mathrm{Mpc}$ and the particle mass was $8.6 \times 10^8\,h^{-1}\,\mathrm{M}_\odot$. The distributions of dark matter halos were stored at discrete epochs. Next, the processes of baryonic physics were added to dark matter halos at each epoch using a semi-analytic galaxy formation model (Guo et al. 2011). Based on the intrinsic parameters of galaxies predicted by the semi-analytic model, such as stellar mass, star formation history, metallicity, and dust content, the photometric properties of simulated galaxies were estimated from the stellar population synthesis models developed by Bruzual & Charlot (2003). Then, these simulated galaxies in boxes at different epochs were projected along the line-of-sight, and intergalactic medium (IGM) absorption was applied in order to mimic a pencil-beam survey using the Madau (1995) IGM light-cone set from Overzier et al. (2013). Finally, 24 light-cone models with $1.4 \times 1.4\,\mathrm{deg}^2$ FoV were extracted using these procedures.

From these light-cone models, we made simulated u-, g-, r-, and i-dropout galaxy catalogs to with the same limiting magnitude with observations. Since the mock catalogue of Henriques et al. (2012) could not completely reproduce galaxies' colors yet, we could not directly apply the same color selection criteria to the simulated catalogue. Instead, we randomly selected galaxies so as to match the expected redshift distribution (Figure 7) of each observed dropout galaxy sample. It should be noted that it is difficult to fairly compare protocluster galaxy properties between observation and model. Based on these catalogs, we investigated the sky distribution and calculated local number density in the same way as in the SDF and the CFHTLS Deep Fields. The examples of sky distribution and contour map of some light-cone models are shown in Figure 13 and 14. From contour maps in the 24 light-cone models, overdense regions were picked up by local maximum of number density in 6 arcmin radius. We first selected the strongest peak in the redshift distribution for that region. Next, we identified the halo ID of the most massive halo in that redshift peak. Finally, the descendant halos at $z = 0$ were identified by tracing the halo merger tree of those high-redshift halos. Figure 15 shows the relation between

the significance of the overdensities of dropout galaxies and the corresponding halo mass at $z = 0$. Despite a large scatter, these two quantities are correlated quite closely. According to the Spearman's rank correlation test, the probability of no correlation is < 0.01. We found that $\gtrsim 85\%$ of $> 4\sigma$ overdense regions are expected to include progenitors of $> 10^{14}\,\mathrm{M}_{\odot}$ dark matter halos and to averagely grow into $\sim 5 - 8 \times 10^{14}\,\mathrm{M}_{\odot}$ at $z = 0$. This result suggests that we can detect a real protocluster with high confidence by measuring the overdensity significance if it is more than 4σ away from the observed surface number density. We can infer its descendant halo mass at $z = 0$ based on Figure 15.

Based on the comparison with model predictions, the criterion of protocluster candidate can be defined as more than 4σ overdensity significance for u-, g-, r-, and i-dropout galaxies. From $4\,\mathrm{deg}^2$ CFHTLS Deep Fields, we found five u-dropout, five g-dropout, six r-dropout, and five i-dropout protocluster candidates. These numbers are roughly consistent with model predictions, in which 0.7, 0.7, 1.3, and 1.6 candidates per $1\,\mathrm{deg}^2$ are expected to be found in u-, g-, r-, and i-dropout galaxies, respectively. Furthermore, one i-dropout protocluster candidate was serendipitously found only in the $0.25\,\mathrm{deg}^2$ SDF.

Table 7. Number of protocluster candidates

Field	N_u	N_g	N_r	N_i
D1	1	2	1	2
D2	1	0	2	1
D3	2	2	1	1
D4	1	1	2	1
SDF	–	–	–	1
Total	5	5	6	6

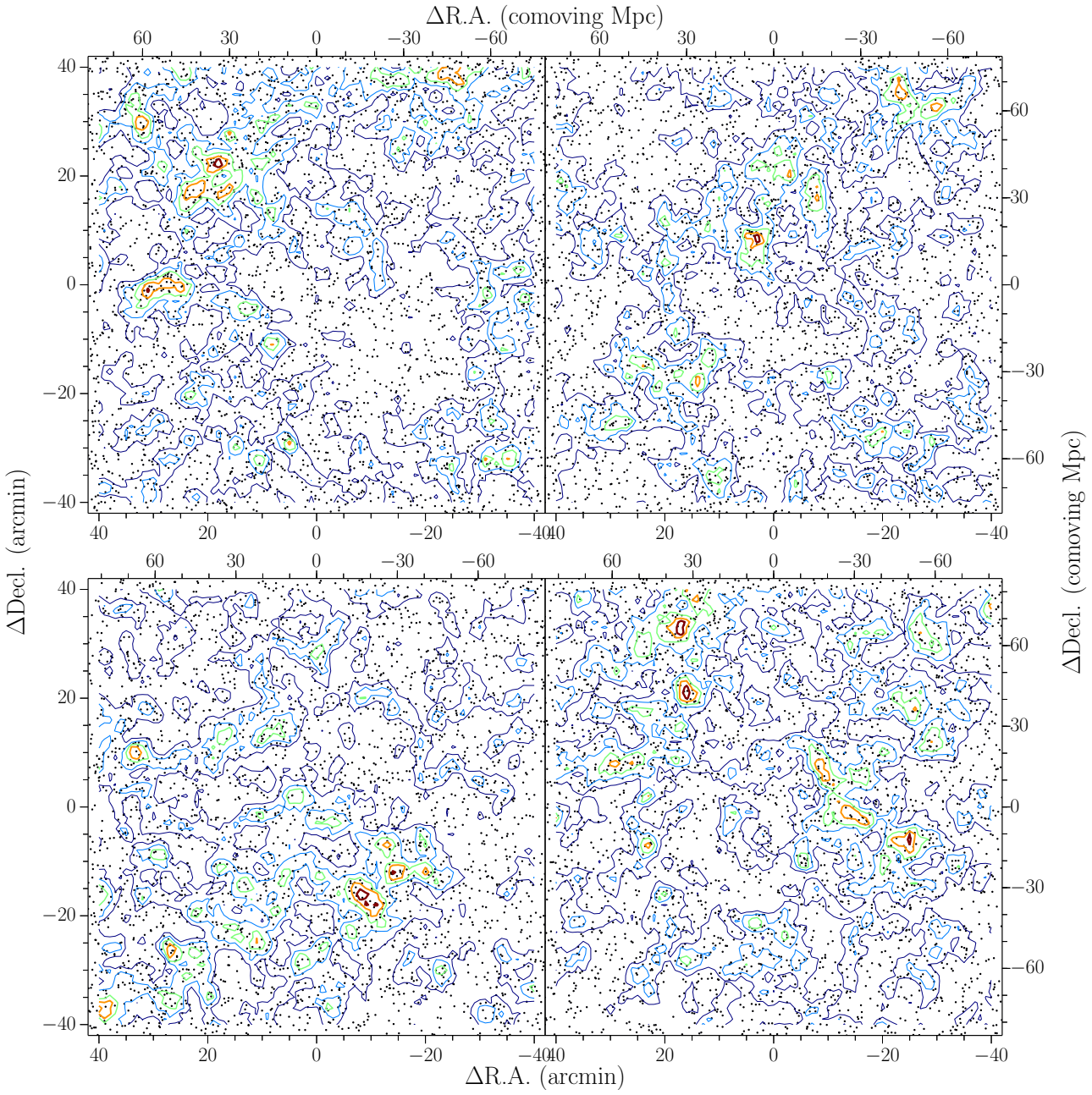

Fig. 13.— Examples of sky distribution of u-dropout (upper) and g-dropout (lower) galaxies in the two different light-cone models, with surface number density contours. Local surface number density was estimated by the same way as in the observation.

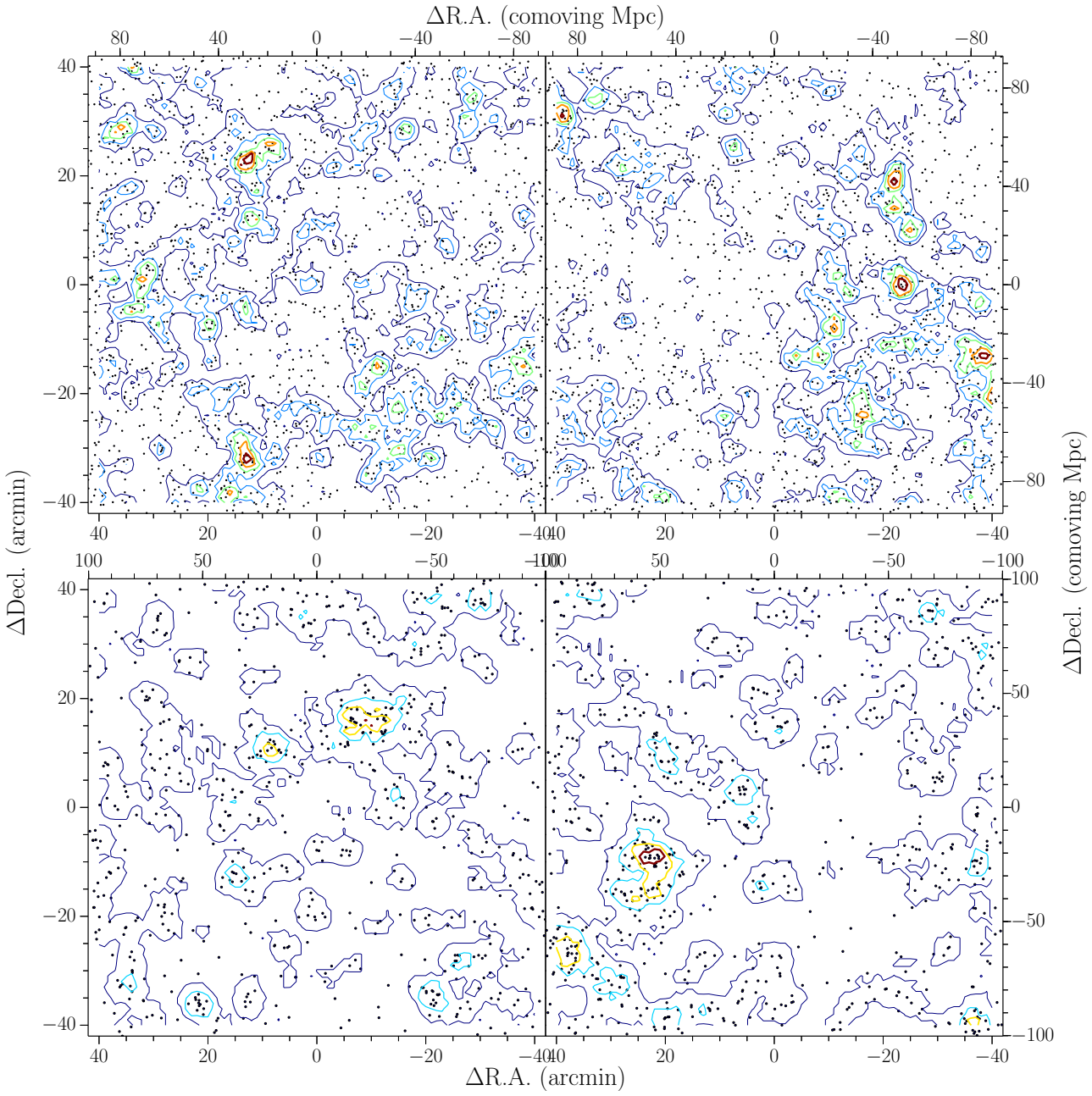

Fig. 14.— Same as Figure 13, but for r-dropout (upper) and i-dropout (lower) galaxies.

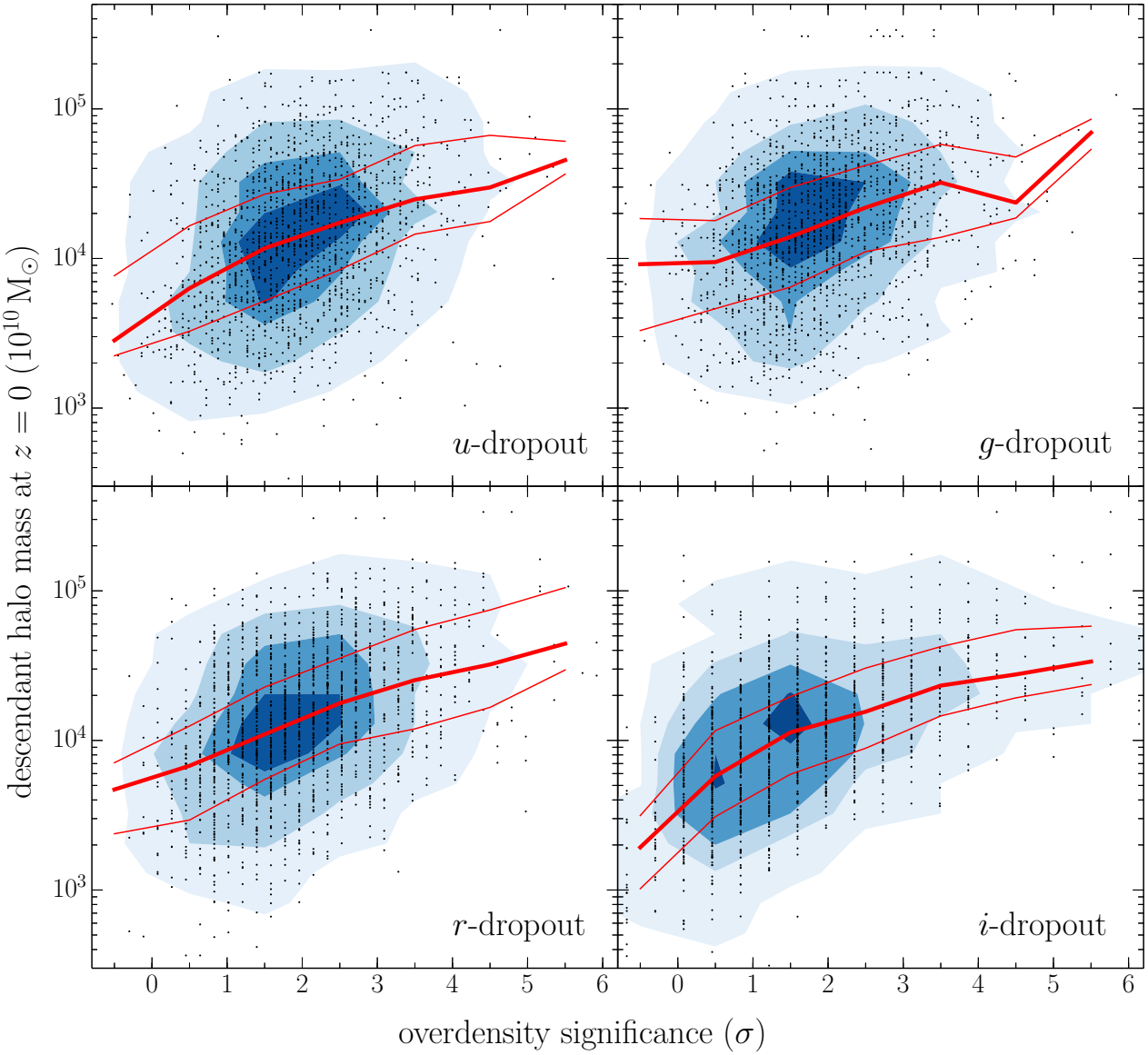

Fig. 15.— Relation between surface overdensity of u-, g-, r-, and i-dropout galaxies and descendant halo mass at $z = 0$ (upper left: u-dropout galaxies, upper right: g-dropout galaxies, lower right: r-dropout galaxies, lower right: i-dropout galaxies) The points represent descendant halo masses in each overdense region. The thick and thin red lines are the median, upper, and lower quartiles. The background contours show the 25, 50, 75, and 95% region from dark to light.

4. FOLLOW-UP SPECTROSCOPY

4.1. How to Confirm Protocluster

Our discovery of overdense regions might be attributed to a mere chance of alignment along the line-of-sight, because the dropout technique samples a broad range of redshifts. It might also be an incidental result of highly clustered contaminating populations. In order to confirm real protoclusters, we have to find three-dimensionally clustering galaxies. Since our protocluster candidates, described in Table 7, were identified as surface overdense regions of dropout galaxies, further confirmation of clustering in redshift space are only required to know whether our candidates are real or not.

Before spectroscopic observation, we investigated how large protocluster members are spread from the center, using the light-cone model (Henriques et al. 2012), in which overdense regions were selected by the same method and criteria with the observations. In the model, protocluster members are defined as galaxies whose descendants at $z = 0$ reside in $> 10^{14}\,\mathrm{M}_{\odot}$ halos. The center of protocluster in three-dimensional space was estimated by the median R.A./Decl./redshift of protocluster members. If the protocluster center of R.A. and Decl. is defined by the peak of surface overdensity, the difference of the center position is typically less than 0.5 arcmin or less than 2 arcmin at worst. Then, we investigated how large protocluster members are spread from the center. We investigated the three-dimensional distribution of protocluster members in the overdense regions. Although each protocluster has a different structural morphology, such as filamentary or sheet-like, we estimated the probability of protocluster member as a function of the distance to the center by counting the numbers of both protocluster members and non-members at a certain distance. We finally derive the probability map by taking the median stack of the probability maps of all protocluster region at a certain redshift. Figure 16 shows the probability map of protocluster members of u-, g-, r-, and i-dropout galaxies. From this model comparison, the distribution of protocluster members is expected to be $R_{\mathrm{sky}} < 4 - 6$ arcmin and $R_z < 0.010 - 0.025$ at $z \sim 3 - 6$. Galaxies lying within this volume will be protocluster members with a probability of $> 80\%$. Therefore, we can define the protocluster region in the scale of 2 physical Mpc and line-of-sight velocity of $|v| < 1000\,\mathrm{km\,s^{-1}}$.

The continuum flux of our galaxy sample were too faint to be detected; therefore, our follow-up spectroscopic observations were mainly aimed at detecting Lyα emission lines from the protocluster member candidates to determine their redshifts. According to Stark et al. (2011); Cassata et al. (2015), the fraction of Lyα emitters in LBG population is $\sim 10\%$ at $z \sim 3$ and $\sim 25\%$ at $z \sim 6$ for bright LBGs ($-21.75 < M_{\mathrm{UV}} < -20.25$). The fraction is increasing in fainter LBGs ($-20.25 < M_{\mathrm{UV}} < -18.75$), in which the fraction become $\sim 30\%$ at $z \sim 3$ and $\sim 55\%$ at $z \sim 6$. Curtis-Lake et al. (2012) derived higher fraction at $z \sim 6$. Therefore, it is feasible to detect Lyα emission lines from a part of our sample. However, it is difficult to predict how many galaxies should be identified in the expected volume of protocluster due to a large variety of the protocluster richness. Furthermore, galaxy population in a protocluster may be different from that in field, implying that Lyα fraction itself is under debate. Follow-up spectroscopic observations are often incomplete. Thus, it should be noted that relative number of confirmed galaxies in the expected volume of protocluster is important rather than the absolute number.

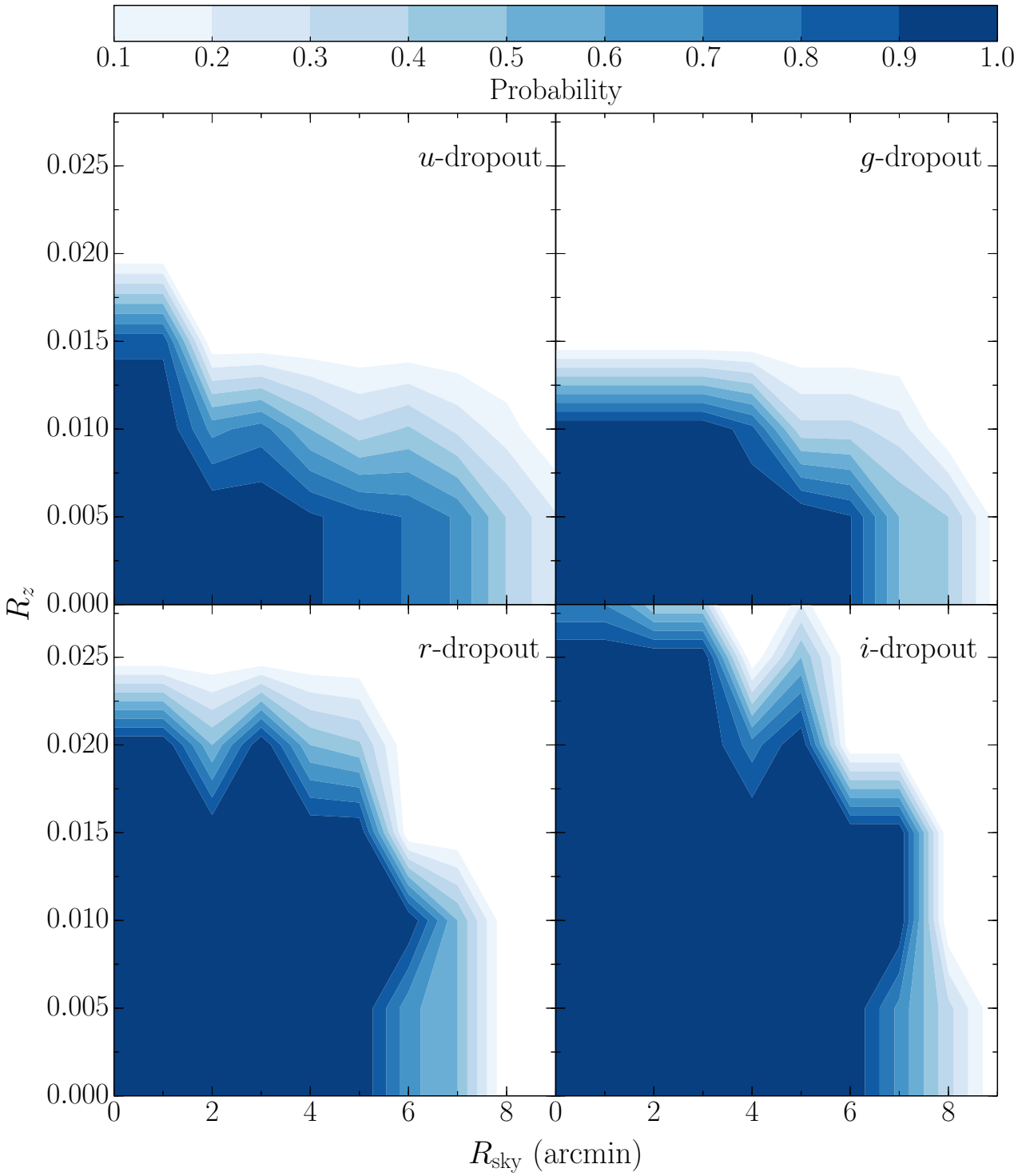

Fig. 16.— probability of protocluster member as a function of distance from the center of a protocluster. The horizontal and vertical axes indicate spatial and redshift directions, and color contours show the probability. The upper left, upper right, lower left, and lower right panels show the probability maps of u-, g-, r-, and i-dropout galaxies, respectively.

4.2. Observations

We carried out spectroscopic observations using Subaru/FOCAS (Kashikawa et al. 2002), KeckII/DEIMOS (Faber et al. 2003), and Gemini-N/GMOS (Hook et al. 2004). In these observations, totally nine protocluster candidates were observed. The detail of protocluster candidates is described in Table 8, and, hereafter, we refer to each protocluster candidates as the "Name" in Table 8 (Column 1). A summary of our spectroscopic observations is given in Table 9. All these observations were conducted with Multi-Object Spectroscopy (MOS) mode. The slits typically had a length of 6−8 arcsec and a width of 0.8−1.0 arcsec. The used grism were selected in order to have highest efficiency at the wavelength of the redshifted Lyα line of targeted dropout galaxies and the spectral resolution of $< 2.8(1 + z_{[\mathrm{OII}]})$ Å, where 2.8 Å is the wavelength separation of [OII] doublet ($\lambda = 3726.0$, 3728.8 Å) in the rest-frame. Therefore, our spectroscopic observations were set up to have high resolution enough to resolve [OII] emission line as doublet. In FOCAS observations, the telescope was dithered along the slit to enable more accurate sky subtraction between exposures. In GMOS observations, we used Nod-and-Shuffle mode, which allows increasing the accuracy of sky subtraction by real-time flipping to the sky position. In MOS slits design, higher priority was given to brighter galaxies in i-band for u-, g-, r-dropout galaxies and in z-band for i-dropout galaxies. Long slit exposures of one of following spectroscopic standard stars HZ44, BD+28d4211, and G191-B2B were used for the flux calibration. The data taken by FOCAS and GMOS were reduced in a standard manner with IRAF, and the pipeline spec2d[1] was used for the reduction of the data taken by DEIMOS. As for the follow-up spectroscopy in the SDF, we also obtained some spectra of i-dropout galaxies through previous MOS observations on several different projects (Nagao et al. 2007; Ota et al. 2008; Kashikawa et al. 2011; Jiang et al. 2011; Shibuya et al. 2012).

[1]The data reduction pipeline was developed at the University of California, Berkeley, with support from National Science Foundation grant AST 00-71048.

Table 8. Overview of the overdense regions observed in our spectroscopic observations

Name	R.A.	Decl.	Field	Population	Overdensity
SDF-*i*drop	13:24:26.0	+27:15:58.3	SDF	*i*-dropout	6.5σ
D1-*i*drop	02:27:19.0	−04:51:08.2	CFHTLS D1	*i*-dropout	6.1σ
D3-*i*drop	14:19:13.9	+52:55:21.9	CFHTLS D3	*i*-dropout	7.6σ
D1-*r*drop	02:24:45.3	−04:55:56.5	CFHTLS D1	*r*-dropout	4.4σ
D4-*r*drop	22:16:44.8	−17:29:16.8	CFHTLS D4	*r*-dropout	4.1σ
D1-*g*drop	02:25:36.3	−04:15:57.4	CFHTLS D1	*g*-dropout	5.5σ
D4-*g*drop	22:16:47.3	−17:16:52.8	CFHTLS D4	*g*-dropout	4.3σ
D1-*u*drop	02:24:35.4	−04:19:58.9	CFHTLS D1	*u*-dropout	4.2σ
D4-*u*drop	22:14:03.4	−17:58:43.4	CFHTLS D4	*u*-dropout	4.4σ

Table 9. Overview of our spectroscopic observations

Data	Instrument	Target	Grism	Resolution	$t_{\rm exp}$ (min.)	$N_{\rm mask}$
2010 Mar. 19 & 20	FOCAS	SDF-*i*drop	VPH900	5.7	240	2
2012 May 13 & 14	GMOS	D3-*i*drop	R600	4.5	330	1
2012 Oct. 21	FOCAS	D1-*i*drop	VPH900	5.7	220	1
2013 Apr. 8	DEIMOS	SDF-*i*drop	830G	2.5	450	1
2014 Aug. 24	DEIMOS	D1-*g*drop	600ZD	3.5	120	1
		D4-*g*drop	600ZD	3.5	120	1
2014 Oct. 20 & 21	FOCAS	D1-*r*drop	VPH650	5.5	280	1
		D1-*g*drop	VPH520	2.5	100	1
		D1-*u*drop	VPH520	2.5	60	4
		D4-*g*drop	VPH520	2.5	120	2
		D4-*u*drop	VPH520	2.5	60	3
2014 Oct. 24 & 25	FOCAS	D4-*r*drop	VPH650	5.5	120	1

4.3. Line Contaminations

Before describing the detail results of follow-up spectroscopy for protocluster candidates, we consider the possible contaminations in our spectroscopic observation. All emission lines we detected are single emission lines, which are not likely to be Hβ or [O III] emission lines because the wavelength coverage of our observation is wide enough to detect all these multiple lines simultaneously. However, only [O III]λ5007 emission, which is generally the strongest emission among them, may resemble to be a single emission line if the other emissions are too faint to be detected. We investigated the possibility that Hα, [O II], and [O III]λ5007 emission lines might have contaminated to our sample, based on both imaging and spectroscopic data. Haines et al. (2008) demonstrated that $\sim 30\%$ of red-sequence galaxies in the field have ongoing star-formation activity with EW(Hα) > 2 Å, but they also found that these galaxies disappear at an absolute r-band magnitude of $M_r \gtrsim -18$. Our samples are much fainter (> 3 mag) than this magnitude, if they were at $z \lesssim 0.3$ based on the photometry of our samples. Regarding [O II] doublet emission lines, it is possible to distinguish between Lyα and [O II] emission lines based on the line profile. The spectral resolution of our spectroscopic observation was set to be high enough to resolve [O II] emission lines as doublets ($\Delta\lambda = 3.8 - 6.3$ Å at $z \sim 0.3 - 1.3$), although it would be practically difficult to resolve these in most cases due to low signal-to-noise ratio (S/N). In this case, the [O II] emission line should be skewed to blueward, while Lyα emission lines from high redshift galaxies should be skewed to redward. We also calculated weighted skewness, S_w, which is a good indicator of the line asymmetry (Kashikawa et al. 2006). The asymmetric emission lines with $S_w > 3$ are evidence of Lyα emission from high redshift galaxies, though it would be more difficult to distinguish them from nearby emission line galaxies only from S_w at $z \sim 3$, where IGM attenuation is weaker than higher redshift. Some emission lines of this study have $S_w < 3$, strong sky lines and low S/N data prevent the accurate determination of skewness in these cases. The red optical color criterion to detect Lyman break could contaminate passive or dustier galaxies, while [O II] and [O III]λ5007 emissions contradict with the observed prominent emission lines as the sign of star-formation activity. Actually, the expected color of passive galaxies based on BC03 is well separated from the selection region, as shown in Figure 5. Thus, it would be difficult even for passive galaxies to mimic the much red color produced by Lyman break. Furthermore, according to Ly et al. (2007, 2012), [O II] emitters at $z \sim 1.5$ and [O III] emitters at $z \sim 0.7$ typically have $i - z \sim 0.2$, and almost all have $i - z < 1.0$, much bluer than the selection criterion of our i-dropout sample ($i - z > 1.5$). Therefore, it is unlikely that Hα, [O II], and [O III]λ5007 emission lines contaminate our sample, and Lyα is the most plausible interpretation for these single emission lines. From these considerations, we can regard all single emission lines detected from our dropout sample as Lyα emission lines. Finally, we did not detect any apparent contaminant objects by our spectroscopic observations.

4.4. Results

We carefully discriminated real emission lines from sky lines or noise by examining two-dimensional and one-dimensional spectra. As discussed in Section 4.3, we regard all single emission lines detected from our dropout galaxy sample as Lyα emission. We estimate the observed properties of the spectroscopically confirmed galaxies, such as UV absolute magnitude ($M_{\rm UV}$), Lyα luminosity ($L_{{\rm Ly}\alpha}$), and rest-frame Lyα equivalent width ($EW_{\rm rest}$). The redshifts were derived by the peak wavelength of the Lyα emission line, assuming the rest wavelength of Lyα to be 1215.6Å. These measurements could be overestimated if there was a galactic outflow. When emission lines are located near strong sky lines, the position of the peak could be shifted. These effects of sky lines and the wavelength resolution are taken into account estimating the error. Observed line flux, $f_{{\rm Ly}\alpha}$, corresponds to the total amount of the flux within the line profile, and its error was estimated from the noise level at wavelengths blueward of Lyα. Since continuum flux was too faint to be detected in the observed spectra, $M_{\rm UV}$ was estimated from the on-band magnitude (g-, r-, i-, and z-band for u-, g-, r-, and i-dropout galaxies) by subtracting the spectroscopically measured Lyα flux and assuming flat UV continuum spectra (f_ν = constant) and IGM absorption. Since the limiting magnitude of z-band is much shallower ($\sim$ 1 mag) than that of i-band, it would be difficult, especially for faint g-dropout galaxies, to accurately estimate $M_{\rm UV}$ by the extrapolation from i- and z-band magnitudes. Only for u-dropout galaxies, $M_{\rm UV}$ can also be estimated by the extrapolation from r- and i-band magnitudes. Furthermore, we also checked the consistency between two methods using u-dropout galaxies, and these two methods derived almost same value (Figure 17). The standard deviation of the difference is 0.19 mag. Although we assume the fixed UV slope, the variation of the $M_{\rm UV}$ derived by single-band magnitude is a few percent at maximum even if the UV slope, β ($f_\lambda \propto \lambda^\beta$), was largely varied from -3.0 to -1.0. In addition, equivalent width, EW, was estimated by combining $f_{{\rm Ly}\alpha}$ and $M_{\rm UV}$. The results of each region are described in the following.

- The i-dropout candidate in the SDF

The follow-up spectroscopic observations on the SDF-$i$drop region were divided into two parts: the one was short exposures to detect bright Lyα emission using FOCAS with the integration time of four hours, and the other was long exposures for faint Lyα emission using DEIMOS with the integration time of 7.5 hours. Combining these two observations, we observed 53 i-dropout galaxies in/around the SDF-$i$drop region. The DEIMOS pointing of this observation was set to also cover 2σ overdense region around the central 6σ region. The sky distribution of i-dropout galaxies and spectroscopically observed galaxies are shown in Figure 18. It should be noted that all of the i-dropout galaxies in the 2σ significant overdense region were completely observed with spectroscopy. From these observations, 28 single emission lines are identified.

The spectra and observed properties of all these galaxies are provided in Figure 19 and Table 10. The redshift distribution is shown in Figure 20. It is clear that ten galaxies are clustered in a narrow redshift range between $z = 5.984$ and $z = 6.047$ ($\Delta z \lesssim 0.06$), corresponding to the radial distance of 3.7 Mpc in physical scale. The central redshift of the protocluster is estimated to be $z = 6.01$ using biweight (Beers et al. 1990) of ten galaxies. This concentration is about 4.5 times higher than the number expected from a homogeneous distribution in redshift

space. Therefore, we have confirmed the existence of a protocluster at $z = 6.01$, which includes ten member galaxies (ID=3-10, 21, 22).

- The i-dropout candidate in the CFHTLS D1

We have observed eight i-dropout galaxies in the D1-$i$drop region out of ten candidates. Almost all i-dropout galaxies in the D1-$i$drop region were spectroscopically observed, as shown in Figure 21. Three galaxies clearly have single emission lines, shown in Figure 22. These lines can be considered as Lyα emission lines of $z \sim 6$ galaxies. Their photometric and spectroscopic properties are summarized in Table 10. Two of three galaxies (ID=1 and 2) have close redshifts with difference of $\Delta z = 0.08$, corresponding to the radial distance of 4.7 Mpc in physical scale. From our selection criteria, we can expect $\sim 0.2-0.4$ galaxy in a $\Delta z = 0.1$ bin if they were homogeneously distributed in redshift space. The possibility to have two galaxies within $\Delta z < 0.1$ is 16%. Although their distribution is more of concentrated than homogeneous, these two galaxies don't seem to merge into a single halo by $z = 0$ compared with the possible separation of protocluster members at $z \sim 6$ (Figure 16). We concluded that there is no clear evidence of a protocluster in the D1-$i$drop region.

- The i-dropout candidate in the CFHTLS D3

As for the D3-$i$drop region, eight i-dropout galaxies were observed out of sixteen candidates. The completeness of spectroscopic observation is smaller ($\sim$ 50%) than the D1-$i$drop region, which has less protocluster member candidates. Many faint i-dropout galaxies are still to be observed because we assigned brighter i-dropout galaxies to be higher priorities. Lyα emission lines were detected from two of eight spectroscopic targets. The sky distribution of the targets of spectroscopic observation and the one-/two-dimensional spectra are shown in Figure 23 and 24, respectively. Table 10 describes the properties of spectroscopically confirmed galaxies. These two galaxies have almost the same redshift with the difference of $\Delta z < 0.01$ (< 0.5 Mpc in physical scale). The possibility that two galaxies have this small redshift separation is 1.2%, and these two galaxies can certainly be expected to be in the same halo at $z = 0$ based on this small separation. While we could not make a clear conclusion due to a small number of confirmed galaxies, the discovery of close galaxy-pair at $z \sim 6$ could imply the existence of a protocluster.

These small number of confirmed clustering galaxies can be attributed to observational limit since our spectroscopic samples are biased to brighter galaxies. Only $M_{UV} < -20.75$ galaxies were spectroscopically observed. Stark et al. (2011) have showed that fainter LBGs tend to have strong Lyα emissions, and the Lyα fraction with $EW_{rest} > 25$ Å is 20 ± 8.1% in the bright sample ($M_{UV} < -20.75$). Although our sample is ~ 0.5 mag brighter than that of Stark et al. (2011) and spectroscopic completeness is not good at the faint-end, the Lyα fraction is found to be 2/16 (12.5 ± 9.0%) in our sample, and it is comparable to that of Stark et al. (2011) within the error. Thus, when our observations are deeper, more i-dropout galaxies could be spectroscopically confirmed and redshift concentrations could be appeared more clearly.

Next, we compared our confirmed galaxies with clear samples of $z \sim 6$ protocluster in the SDF. In this protocluster, the number of confirmed member galaxies with $M_{UV} < -20.75$ was only two. Furthermore, Ouchi et al. (2005) reported the discovery of two protoclusters at $z \sim 5.7$. These were discovered by the narrow-band survey, and six and four LAEs are included

in each protocluster. Although LAE selection is different from our dropout selection, it is useful to check the distribution of the UV continuum and the Lyα luminosity of protocluster galaxies. Based on our observational limits of UV continuum and Lyα luminosity, only ~ 2 LAEs can be identified from these protoclusters. Therefore, it was reasonable to confirm only two member galaxies in our observation even if there is a real protocluster.

- The r-dropout candidate in the CFHTLS D1

We have spectroscopically observed fifteen r-dropout galaxies in the D1-$r$drop region, and detected single emission lines from six galaxies. The sky distribution of the observed galaxies and the one-/two-dimensional spectra are shown in Figure 25 and 26, respectively. In the $> 1\sigma$ overdense region, there are ~ 40 galaxies; thus, only $\sim 38\%$ r-dropout galaxies were observed by the follow-up spectroscopy. Two galaxies (ID=5 and 6) out of six are clustering both in spatial (Δsky $= 33$ arcsec) and redshift space ($\Delta z = 0.004$) at $z = 4.89$, whose three-dimensional separation is 0.7 Mpc in physical scale. Considering the observed volume ($r = 3$ arcmin aperture and $\Delta z \sim 0.8$), probability is very low ($< 1\%$) that the close pair is reproduced by uniform random distribution of six galaxies in three-dimensional space. Although the number of confirmed galaxies is too small to confirm a protocluster, the close galaxy-pair indicates the existence of a protocluster; at least, these two galaxies are expected to merge into a single halo by $z = 0$. Since there are many spectroscopically unobserved galaxies, further follow-up observation will enable to clearly confirm a protocluster.

- The r-dropout candidate in the CFHTLS D4

In the D4-$r$drop region, the total integration time of follow-up spectroscopic observation was only two hours, which was half of that in the D1-$r$drop region. Thus, although twelve r-dropout galaxies were observed, Lyα emission lines were detected from only three galaxies. The sky distribution of the observed galaxies and the one-/two-dimensional spectra are shown in Figure 27 and 28, respectively. These three galaxies are largely separated in redshift space. Since about 20 r-dropout galaxies remain to be spectroscopically observed, further follow-up observation will be necessary to make a conclusion. At present, we could not find any clustering galaxies based only on the confirmed three galaxies.

- The g-dropout candidate in the CFHTLS D1

Combining the DEIMOS and FOCAS follow-up observations, 123 g-dropout galaxies were observed, and the redshifts of 36 galaxies were determined by detecting Lyα emission lines. The sky distribution of the observed galaxies and the one-/two-dimensional spectra are shown in Figure 29 and 30, respectively. Figure 31 shows the redshift distribution of confirmed galaxies. Although galaxies seems to be clustering at $z \sim 3.8$, these galaxies are spread over wide spatial area, as shown in Figure 29. DEIMOS has a wide FoV ($\sim 16.7 \times 5.0$ arcmin^2), which is larger than the are of the D1-$g$drop region; therefore, we also targeted g-dropout galaxies that are not in the overdense region. The red-line histogram in Figure 31 shows the redshift distribution of confirmed galaxies only in the overdense region. The halves of galaxies in the peak at $z = 3.80$ disperse in redshift space as shown in the inset of Figure 31. Although protocluster members are expected to be clustering within $\Delta v < 1000$ km/s, there are only three galaxies within the range. From these considerations, we concluded that there is not a protocluster in the D1-$g$drop

region.

- The g-dropout candidate in the CFHTLS D4

Combining the DEIMOS and FOCAS follow-up observations, 144 g-dropout galaxies were spectroscopically observed, and the redshifts of 42 galaxies were determined by detecting Lyα emission lines. The sky distribution of the observed galaxies and the one-/two-dimensional spectra are shown in Figure 32 and 33, respectively. The redshift distribution is shown in Figure 34. There is a clear excess at $z = 3.67$, and, in this peak, eleven galaxies are clustering in narrow redshift range of $\Delta z = 0.016$, corresponding to 2.6 Mpc in physical scale. We confirmed that galaxies are clustering both in spatial and redshift space. Based on a strong evidence, we concluded that there is a protocluster at $z = 3.67$, which includes eleven member galaxies (ID=10-20).

In addition, it should be noted that an AGN was found in this region at (ΔR.A., ΔDecl.) = $(-1.9, 6.8)$ arcmin in Figure 32. The redshift was derived to be $z = 3.72$ based on its HeII and CIII] emission lines (Figure 35). According to this estimation, the redshift separation between the AGN and the center of the protocluster is $\Delta z = 0.05$, which corresponds to the radial velocity of $v \sim 3000\,\mathrm{km\,s^{-1}}$. Therefore, it is unlikely that this AGN is one of protocluster members and will merge with the protocluster into a single halo by $z = 0$.

- The u-dropout candidate in the CFHTLS D1

We have spectroscopically observed 95 u-dropout galaxies in the D1-$u$drop region, and 30 galaxies have single emission lines. The sky distribution of the observed galaxies and the one-/two-dimensional spectra are shown in Figure 36 and 37, respectively. The redshift distribution is shown in Figure 38. There is a excess at $z = 3.13$, including five galaxies within $\Delta z = 0.008$. The spatial and redshift separations among these five galaxies are small enough to merge into a single halo by $z = 0$ compared with the model prediction; therefore we confirmed a protocluster at $z = 3.13$, which includes five member galaxies (ID=6-10).

- The u-dropout candidate in the CFHTLS D4

We have spectroscopically observed 57 u-dropout galaxies in the D4-$u$drop region, and 16 galaxies have single emission lines. The sky distribution of the observed galaxies and the one-/two-dimensional spectra are shown in Figure 39 and 40, respectively. The redshift distribution is shown in Figure 41. There is a peak at $z = 3.24$, including five galaxies within $\Delta z = 0.008$. These five galaxies are expected to merge into a single halo by $z = 0$ compared with the model prediction. Therefore, we confirmed a protocluster at $z = 3.24$, which includes five member galaxies (ID=7-11).

- Summary of protocluster confirmation

From these follow-up spectroscopic observations, we confirmed four protoclusters in the SDF-$i$drop, D4-$g$drop, D1-$u$drop, and D4-$u$drop regions. The overdense region of the D1-$g$drop region was found not to be a protocluster. Thus, we observationally confirmed that the success rate of protocluster finding is almost consistent with that of model prediction ($\lesssim 85\%$ of 4σ overdense regions are expected to be real protoclusters). Although we found two possible

protoclusters in the D3-$i$drop and D1-$r$drop regions, it is unclear that the other overdense regions of the D1/3-$i$drop and D1/4-$r$drop are real protoclusters or not because of small number of spectroscopically confirmed galaxies. The summary of protocluster confirmation is described in Table 11. The radial velocity dispersion of the protoclusters were calculated by the redshifts of protocluster members using the biweight variance (Beers et al. 1990). The uncertainty of radial velocity dispersion was estimated by bootstrapping, in which bootstrap sample was added the random error determined by the velocity resolution of our spectroscopic observations.

Table 10. Observed properties of all spectroscopic confirmed dropout galaxies.

ID	R.A. (J2000)	Decl. (J2000)	m^{a} (mag)	redshift	$M_{\rm UV}$ (mag)	$f_{{\rm Ly}\alpha}$ ($10^{-18}\,{\rm erg\,s^{-1}\,cm^{-2}}$)	$L_{{\rm Ly}\alpha}$ ($10^{42}\,{\rm erg\,s^{-1}}$)	$EW_{\rm rest}$ (Å)	S_w (Å)
SDF-*i*drop (28 galaxies)									
1	13:24:31.8	+27:18:44.2	25.91 ± 0.04	$5.758^{+0.001}_{-0.001}$	-20.74 ± 0.04	4.39 ± 0.86	1.59 ± 0.31	7.7 ± 1.4	5.61 ± 1.36
2	13:24:18.4	+27:16:32.6	25.69 ± 0.03	$5.916^{+0.002}_{-0.002}$	-20.97 ± 0.03	12.49 ± 0.36	4.82 ± 0.14	19.0 ± 0.8	5.66 ± 1.14
3	13:24:25.2	+27:16:12.2	27.02 ± 0.09	$5.984^{+0.006}_{-0.002}$	-19.60 ± 0.10	4.95 ± 0.51	1.96 ± 0.20	29.6 ± 4.1	3.41 ± 4.03
4	13:24:30.2	+27:14:13.5	26.81 ± 0.08	$5.991^{+0.002}_{-0.002}$	-19.51 ± 0.11	15.42 ± 0.63	6.12 ± 0.25	107.5 ± 12.2	5.26 ± 1.21
5	13:24:26.0	+27:16:03.0	26.50 ± 0.06	$5.992^{+0.002}_{-0.002}$	-20.11 ± 0.10	8.16 ± 0.58	3.24 ± 0.23	31.4 ± 3.8	10.01 ± 0.93
6	13:24:21.3	+27:13:04.8	25.91 ± 0.04	$5.999^{+0.002}_{-0.006}$	-20.79 ± 0.04	7.59 ± 0.68	3.02 ± 0.27	15.3 ± 1.5	12.28 ± 1.84
7	13:24:29.0	+27:19:18.0	26.50 ± 0.06	$6.012^{+0.002}_{-0.002}$	-20.11 ± 0.07	7.87 ± 1.50	3.15 ± 0.60	30.7 ± 6.2	5.06 ± 1.84
8	13:24:28.1	+27:19:32.8	26.10 ± 0.04	$6.012^{+0.002}_{-0.002}$	-20.32 ± 0.06	21.34 ± 0.57	8.54 ± 0.23	70.8 ± 4.5	4.07 ± 0.73
9	13:24:26.5	+27:15:59.7	25.47 ± 0.03	$6.025^{+0.003}_{-0.004}$	-21.03 ± 0.05	29.94 ± 2.63	12.04 ± 1.06	50.9 ± 5.1	8.00 ± 0.21
10	13:24:31.5	+27:15:08.8	25.91 ± 0.06	$6.027^{+0.002}_{-0.002}$	-20.43 ± 0.10	27.36 ± 2.95	11.02 ± 1.19	95.7 ± 14.2	8.12 ± 0.23
11	13:24:26.1	+27:18:40.5	26.59 ± 0.06	$6.131^{+0.003}_{-0.003}$	-19.87 ± 0.11	12.38 ± 1.19	5.19 ± 0.50	67.0 ± 9.5	4.24 ± 0.35
12	13:24:31.6	+27:19:58.2	26.47 ± 0.06	$6.190^{+0.002}_{-0.002}$	-19.36 ± 0.19	24.48 ± 0.69	10.49 ± 0.29	213.1 ± 40.3	4.69 ± 0.88
13	13:24:44.3	+27:19:50.0	26.43 ± 0.06	$6.211^{+0.004}_{-0.007}$	-20.23 ± 0.09	15.01 ± 0.74	6.48 ± 0.32	58.7 ± 6.1	7.24 ± 1.24
14	13:24:20.6	+27:16:40.5	27.01 ± 0.09	$6.271^{+0.002}_{-0.005}$	-19.35 ± 0.22	14.28 ± 0.94	6.30 ± 0.42	136.4 ± 32.1	6.25 ± 0.62
15	13:24:32.6	+27:19:04.0	25.54 ± 0.03	$6.278^{+0.005}_{-0.002}$	-21.75 ± 0.03	4.00 ± 0.50	1.77 ± 0.22	2.2 ± 0.3	2.35 ± 3.20
16	13:24:44.8	+27:17:48.8	26.10 ± 0.04	$5.764^{+0.001}_{-0.001}$	-20.55 ± 0.04	7.08 ± 0.72	2.57 ± 0.26	16.0 ± 1.8	6.82 ± 0.71
17	13:24:44.5	+27:20:23.4	26.70 ± 0.07	$5.791^{+0.001}_{-0.001}$	-19.95 ± 0.07	6.18 ± 0.71	2.27 ± 0.26	26.6 ± 3.3	2.80 ± 1.39
18	13:24:27.4	+27:17:17.4	26.62 ± 0.06	$5.797^{+0.001}_{-0.001}$	-20.03 ± 0.06	5.67 ± 0.70	2.09 ± 0.26	23.3 ± 2.9	2.15 ± 0.42
19	13:24:26.6	+27:16:41.7	26.84 ± 0.08	$5.844^{+0.001}_{-0.001}$	-19.84 ± 0.08	1.26 ± 0.33	0.47 ± 0.12	6.3 ± 1.5	-0.66 ± 0.67
20	13:24:12.7	+27:16:33.3	25.99 ± 0.04	$5.914^{+0.001}_{-0.001}$	-20.67 ± 0.04	13.17 ± 0.74	5.08 ± 0.29	30.2 ± 2.2	2.51 ± 0.27
21	13:24:10.8	+27:19:04.0	26.61 ± 0.06	$6.039^{+0.001}_{-0.001}$	-19.88 ± 0.09	10.95 ± 0.99	4.43 ± 0.40	54.6 ± 8.3	6.04 ± 0.57
22	13:24:05.9	+27:18:37.7	26.87 ± 0.08	$6.047^{+0.001}_{-0.001}$	-19.84 ± 0.09	3.97 ± 0.72	1.61 ± 0.29	20.9 ± 4.5	4.53 ± 0.82
23	13:24:30.2	+27:16:10.8	26.15 ± 0.05	$6.125^{+0.001}_{-0.001}$	-20.61 ± 0.06	9.37 ± 0.60	3.92 ± 0.25	28.4 ± 2.4	0.93 ± 0.19
24	13:24:37.3	+27:20:08.5	26.00 ± 0.04	$6.224^{+0.001}_{-0.001}$	-20.93 ± 0.06	13.46 ± 1.37	5.85 ± 0.59	26.9 ± 3.9	30.20 ± 6.33
25	13:24:51.7	+27:19:55.3	26.84 ± 0.08	$6.252^{+0.001}_{-0.001}$	-19.99 ± 0.12	8.90 ± 0.57	3.90 ± 0.25	43.1 ± 6.6	0.87 ± 0.90
26	13:24:06.6	+27:16:46.4	26.81 ± 0.08	$6.267^{+0.001}_{-0.001}$	-20.28 ± 0.09	4.99 ± 0.40	2.20 ± 0.18	19.3 ± 2.5	2.00 ± 0.11
27	13:24:24.5	+27:15:56.9	26.69 ± 0.07	$6.359^{+0.001}_{-0.001}$	-20.25 ± 0.12	14.07 ± 0.71	6.41 ± 0.32	58.1 ± 8.4	8.28 ± 2.03
28	13:24:06.5	+27:16:34.3	26.97 ± 0.09	$6.549^{+0.001}_{-0.001}$	-20.92 ± 0.10	4.39 ± 0.64	2.14 ± 0.31	9.3 ± 2.0	3.86 ± 1.35
D1-*i*drop (three galaxies)									
1	02:27:18.8	-04:50:08.3	25.45 ± 0.06	$5.966^{+0.002}_{-0.003}$	-21.57 ± 0.06	2.66 ± 0.41	1.05 ± 0.16	2.41 ± 0.46	2.25 ± 1.21
2	02:27:21.0	-04:50:49.3	25.97 ± 0.10	$6.044^{+0.002}_{-0.002}$	-20.85 ± 0.13	19.55 ± 0.72	7.92 ± 0.29	40.05 ± 6.13	5.21 ± 0.72
3	02:27:19.0	-04:53:48.0	26.30 ± 0.13	$6.325^{+0.002}_{-0.002}$	-20.76 ± 0.24	31.73 ± 0.46	14.29 ± 0.21	81.79 ± 24.95	7.85 ± 0.59
D3-*i*drop (two galaxies)									
1	14:19:22.5	+52:57:22.5	25.21 ± 0.05	$5.749^{+0.002}_{-0.002}$	-21.49 ± 0.05	5.80 ± 0.88	2.09 ± 0.32	3.79 ± 0.84	5.41 ± 1.16
2	14:19:17.2	+52:56:14.4	25.74 ± 0.08	$5.756^{+0.002}_{-0.002}$	-20.94 ± 0.08	8.16 ± 1.10	2.95 ± 0.40	10.84 ± 2.14	5.38 ± 3.85

Table 10—Continued

ID	R.A. (J2000)	Decl. (J2000)	m^{a} (mag)	redshift	$M_{\rm UV}$ (mag)	$f_{{\rm Ly}\alpha}$ ($10^{-18}\,{\rm erg\,s^{-1}\,cm^{-2}}$)	$L_{{\rm Ly}\alpha}$ ($10^{42}\,{\rm erg\,s^{-1}}$)	$EW_{\rm rest}$ (Å)	S_w (Å)
				D1-$r$drop (six galaxies)					
1	02:24:45.467	-04:58:52.83	26.37 ± 0.06	$4.431^{+0.002}_{-0.002}$	-19.85 ± 0.14	1.60 ± 0.39	0.31 ± 0.08	4.09 ± 1.14	3.08 ± 5.41
2	02:24:45.957	-04:56:57.69	26.14 ± 0.05	$4.602^{+0.002}_{-0.002}$	-20.14 ± 0.12	2.75 ± 0.46	0.59 ± 0.10	5.84 ± 1.17	0.72 ± 4.11
3	02:24:42.586	-04:58:36.00	26.81 ± 0.09	$4.742^{+0.002}_{-0.002}$	-19.49 ± 0.21	5.22 ± 0.46	1.20 ± 0.10	21.69 ± 5.06	6.73 ± 2.10
4	02:24:38.212	-04:57:15.05	26.16 ± 0.05	$4.840^{+0.002}_{-0.002}$	-20.21 ± 0.13	5.67 ± 0.73	1.37 ± 0.18	12.79 ± 2.28	15.74 ± 5.69
5	02:24:45.964	-04:54:34.80	26.12 ± 0.05	$4.890^{+0.002}_{-0.002}$	-20.35 ± 0.12	1.73 ± 0.31	0.43 ± 0.08	3.52 ± 0.74	3.11 ± 2.06
6	02:24:43.757	-04:54:31.19	26.32 ± 0.05	$4.894^{+0.002}_{-0.002}$	-20.19 ± 0.14	1.56 ± 0.29	0.39 ± 0.07	3.69 ± 0.85	0.58 ± 6.76
				D4-$r$drop (three galaxies)					
1	22:16:46.722	-17:28:02.00	26.00 ± 0.05	$4.630^{+0.002}_{-0.002}$	-20.27 ± 0.12	1.27 ± 0.17	0.28 ± 0.04	2.44 ± 0.43	3.47 ± 21.52
2	22:16:39.959	-17:31:34.58	25.94 ± 0.04	$4.865^{+0.002}_{-0.002}$	-20.41 ± 0.12	10.31 ± 0.45	2.52 ± 0.11	19.51 ± 2.48	14.12 ± 2.55
3	22:16:45.765	-17:29:19.89	26.07 ± 0.05	$4.952^{+0.002}_{-0.002}$	-20.36 ± 0.14	9.98 ± 0.35	2.54 ± 0.09	20.67 ± 2.93	15.00 ± 2.88
				D1-$g$drop (36 galaxies)					
1	02:25:28.536	-04:17:14.12	26.93 ± 0.07	$3.435^{+0.001}_{-0.001}$	-18.85 ± 0.15	12.50 ± 1.49	1.34 ± 0.16	43.82 ± 8.47	3.32 ± 8.74
2	02:25:30.408	-04:15:56.70	26.92 ± 0.07	$3.623^{+0.001}_{-0.001}$	-18.92 ± 0.16	6.94 ± 0.92	0.84 ± 0.11	25.90 ± 5.31	2.74 ± 2.46
3	02:25:32.014	-04:17:03.56	27.17 ± 0.09	$3.705^{+0.001}_{-0.001}$	-18.66 ± 0.21	6.85 ± 1.01	0.88 ± 0.13	34.18 ± 8.92	8.91 ± 4.93
4	02:25:25.565	-04:17:12.58	27.15 ± 0.09	$3.717^{+0.001}_{-0.001}$	-18.73 ± 0.20	4.51 ± 0.90	0.58 ± 0.12	21.26 ± 6.04	1.08 ± 1.34
5	02:26:12.550	-04:18:41.23	26.69 ± 0.06	$3.733^{+0.001}_{-0.001}$	-18.94 ± 0.17	21.41 ± 1.71	2.79 ± 0.22	83.76 ± 15.69	-0.32 ± 3.13
6	02:25:17.290	-04:14:02.23	25.40 ± 0.02	$3.738^{+0.001}_{-0.001}$	-20.49 ± 0.04	21.57 ± 1.23	2.82 ± 0.16	20.45 ± 1.43	6.11 ± 0.86
7	02:25:51.739	-04:14:37.26	26.07 ± 0.03	$3.744^{+0.001}_{-0.001}$	-19.91 ± 0.07	3.07 ± 0.79	0.40 ± 0.10	4.97 ± 1.32	0.23 ± 2.27
8	02:25:39.708	-04:14:20.73	25.22 ± 0.01	$3.754^{+0.001}_{-0.001}$	-20.76 ± 0.04	9.32 ± 1.58	1.23 ± 0.21	6.97 ± 1.20	9.41 ± 9.42
9	02:26:11.563	-04:19:21.65	25.88 ± 0.03	$3.755^{+0.001}_{-0.001}$	-19.82 ± 0.08	39.82 ± 2.21	5.27 ± 0.29	70.40 ± 6.78	8.13 ± 1.98
10	02:26:10.246	-04:18:18.50	26.81 ± 0.06	$3.759^{+0.001}_{-0.001}$	-18.69 ± 0.21	25.61 ± 1.08	3.40 ± 0.14	128.41 ± 28.60	5.91 ± 0.54
11	02:25:33.011	-04:14:45.24	25.28 ± 0.02	$3.766^{+0.001}_{-0.001}$	-20.53 ± 0.04	47.32 ± 2.23	6.30 ± 0.30	43.78 ± 2.74	12.15 ± 1.04
12	02:26:07.202	-04:17:12.22	26.73 ± 0.06	$3.793^{+0.001}_{-0.001}$	-19.17 ± 0.15	9.89 ± 1.63	1.34 ± 0.22	32.77 ± 7.27	3.60 ± 4.24
13	02:25:59.907	-04:15:45.42	26.23 ± 0.04	$3.797^{+0.001}_{-0.001}$	-19.74 ± 0.09	10.03 ± 2.29	1.36 ± 0.31	19.73 ± 4.83	7.09 ± 4.96
14	02:25:57.460	-04:18:10.27	26.01 ± 0.03	$3.799^{+0.001}_{-0.001}$	-19.99 ± 0.07	7.82 ± 1.38	1.06 ± 0.19	12.24 ± 2.32	8.82 ± 4.36
15	02:25:42.923	-04:15:38.74	26.41 ± 0.04	$3.800^{+0.001}_{-0.001}$	-19.44 ± 0.12	17.61 ± 1.24	2.40 ± 0.17	45.41 ± 6.08	9.85 ± 1.19
16	02:25:44.405	-04:14:11.81	25.32 ± 0.02	$3.803^{+0.001}_{-0.001}$	-20.64 ± 0.04	24.22 ± 2.34	3.30 ± 0.32	20.78 ± 2.16	10.09 ± 2.61
17	02:25:34.147	-04:14:21.23	26.40 ± 0.04	$3.809^{+0.001}_{-0.001}$	-19.59 ± 0.11	8.27 ± 1.39	1.13 ± 0.19	18.65 ± 3.66	6.15 ± 4.06
18	02:25:56.529	-04:17:27.85	26.77 ± 0.06	$3.818^{+0.001}_{-0.001}$	-19.15 ± 0.16	10.76 ± 1.85	1.48 ± 0.25	36.77 ± 8.52	3.17 ± 8.69
19	02:25:30.087	-04:15:15.84	25.85 ± 0.03	$3.827^{+0.001}_{-0.001}$	-20.20 ± 0.06	6.02 ± 0.94	0.83 ± 0.13	7.83 ± 1.30	8.59 ± 1.02
20	02:25:49.845	-04:14:53.42	26.57 ± 0.05	$3.829^{+0.001}_{-0.001}$	-19.35 ± 0.13	13.03 ± 1.37	1.81 ± 0.19	37.33 ± 6.22	13.66 ± 4.39
21	02:25:41.772	-04:16:06.53	25.70 ± 0.02	$3.843^{+0.001}_{-0.001}$	-20.30 ± 0.06	21.31 ± 1.34	2.98 ± 0.19	25.65 ± 2.14	-0.62 ± 0.96
22	02:25:56.593	-04:15:15.20	26.89 ± 0.07	$3.859^{+0.001}_{-0.001}$	-18.85 ± 0.21	19.31 ± 1.22	2.73 ± 0.17	88.80 ± 19.46	5.15 ± 0.78
23	02:25:39.324	-04:14:40.82	26.79 ± 0.06	$3.866^{+0.001}_{-0.001}$	-19.12 ± 0.17	13.16 ± 1.11	1.87 ± 0.16	47.68 ± 8.84	5.37 ± 0.92
24	02:26:11.555	-04:17:39.51	26.38 ± 0.04	$3.886^{+0.001}_{-0.001}$	-19.35 ± 0.14	33.92 ± 2.51	4.87 ± 0.36	100.23 ± 15.93	1.63 ± 1.82
25	02:25:27.362	-04:16:43.59	27.28 ± 0.10	$3.891^{+0.001}_{-0.001}$	-18.37 ± 0.32	17.16 ± 1.63	2.47 ± 0.24	125.83 ± 44.70	2.87 ± 0.77

Table 10—Continued

ID	R.A. (J2000)	Decl. (J2000)	m^{a} (mag)	redshift	$M_{\rm UV}$ (mag)	$f_{{\rm Ly}\alpha}$ (10^{-18} erg s^{-1} cm^{-2})	$L_{{\rm Ly}\alpha}$ (10^{42} erg s^{-1})	$EW_{\rm rest}$ (Å)	S_w (Å)
26	02:25:25.816	-04:16:38.94	27.61 ± 0.13	$3.927^{+0.001}_{-0.001}$	-18.04 ± 0.43	13.14 ± 1.83	1.93 ± 0.27	133.94 ± 67.59	-1.16 ± 6.97
27	02:26:01.853	-04:14:41.24	27.73 ± 0.15	$4.000^{+0.001}_{-0.001}$	-17.65 ± 0.61	15.71 ± 2.24	2.41 ± 0.34	238.11 ± 183.28	5.40 ± 1.71
28	02:25:31.239	-04:15:49.81	26.37 ± 0.04	$4.054^{+0.001}_{-0.001}$	-19.76 ± 0.12	18.39 ± 1.82	2.92 ± 0.29	41.22 ± 6.28	5.63 ± 2.24
29	02:25:35.470	-04:14:15.68	26.25 ± 0.04	$4.119^{+0.001}_{-0.001}$	-19.94 ± 0.11	23.18 ± 1.90	3.82 ± 0.31	45.59 ± 6.16	3.35 ± 4.05
30	02:25:34.433	-04:15:05.46	26.37 ± 0.04	$4.185^{+0.001}_{-0.001}$	-19.83 ± 0.13	25.45 ± 1.46	4.35 ± 0.25	57.91 ± 8.23	8.31 ± 0.57
31	02:25:39.830	-04:14:53.33	26.20 ± 0.04	$4.236^{+0.001}_{-0.001}$	-20.19 ± 0.11	23.32 ± 2.01	4.11 ± 0.35	39.12 ± 5.27	6.86 ± 1.12
32	02:25:11.525	-04:16:20.17	25.91 ± 0.03	$4.276^{+0.001}_{-0.001}$	-19.10 ± 0.29	107.86 ± 2.43	19.42 ± 0.44	505.39 ± 153.02	2.40 ± 0.33
33	02:25:57.659	-04:14:24.90	26.54 ± 0.05	$4.385^{+0.001}_{-0.001}$	-18.83 ± 0.40	61.69 ± 2.19	11.79 ± 0.42	393.36 ± 177.53	5.26 ± 0.81
34	02:25:21.473	-04:16:01.50	27.04 ± 0.08	$4.391^{+0.001}_{-0.001}$	-19.20 ± 0.30	23.76 ± 2.33	4.55 ± 0.45	107.90 ± 36.20	5.27 ± 1.87
35	02:25:08.716	-04:15:24.74	27.10 ± 0.08	$4.395^{+0.001}_{-0.001}$	-19.34 ± 0.27	52.76 ± 2.69	10.13 ± 0.52	210.28 ± 60.76	7.74 ± 0.99
36	02:25:28.097	-04:14:54.46	27.68 ± 0.14	$4.442^{+0.001}_{-0.001}$	-18.01 ± 0.78	22.59 ± 2.06	4.45 ± 0.41	316.27 ± 334.36	4.13 ± 1.99
					D4-*g*drop (42 galaxies)				
1	22:16:55.191	-17:25:51.91	24.53 ± 0.01	$3.568^{+0.001}_{-0.001}$	-21.32 ± 0.02	11.47 ± 1.23	1.34 ± 0.14	4.54 ± 0.50	7.39 ± 2.56
2	22:17:00.190	-17:25:06.37	26.39 ± 0.05	$3.569^{+0.001}_{-0.001}$	-19.45 ± 0.11	9.05 ± 1.27	1.06 ± 0.15	20.01 ± 3.48	4.83 ± 1.81
3	22:16:55.670	-17:20:49.98	27.16 ± 0.10	$3.581^{+0.001}_{-0.001}$	-18.67 ± 0.21	6.39 ± 0.65	0.76 ± 0.08	29.05 ± 6.79	1.78 ± 1.80
4	22:16:49.872	-17:21:53.02	25.42 ± 0.02	$3.622^{+0.001}_{-0.001}$	-20.44 ± 0.05	14.01 ± 1.24	1.70 ± 0.15	12.85 ± 1.26	5.97 ± 4.29
5	22:17:01.326	-17:20:52.55	26.81 ± 0.07	$3.624^{+0.001}_{-0.001}$	-19.04 ± 0.15	5.40 ± 1.15	0.66 ± 0.14	17.95 ± 4.70	-0.73 ± 2.60
6	22:16:54.811	-17:28:37.91	26.93 ± 0.08	$3.626^{+0.001}_{-0.001}$	-18.89 ± 0.18	10.59 ± 1.15	1.29 ± 0.14	40.75 ± 8.47	3.86 ± 1.26
7	22:16:58.872	-17:28:33.27	26.33 ± 0.04	$3.628^{+0.001}_{-0.001}$	-19.53 ± 0.10	6.92 ± 1.32	0.84 ± 0.16	14.68 ± 3.15	5.65 ± 3.60
8	22:17:07.296	-17:28:45.15	26.22 ± 0.04	$3.654^{+0.001}_{-0.001}$	-19.61 ± 0.10	16.61 ± 1.61	2.06 ± 0.20	33.43 ± 4.49	4.80 ± 3.23
9	22:16:51.756	-17:24:57.97	26.26 ± 0.04	$3.666^{+0.001}_{-0.001}$	-19.59 ± 0.10	11.90 ± 0.89	1.49 ± 0.11	24.67 ± 3.00	1.03 ± 2.79
10	22:16:42.993	-17:15:53.36	26.96 ± 0.08	$3.669^{+0.001}_{-0.001}$	-18.90 ± 0.18	4.98 ± 0.89	0.62 ± 0.11	19.56 ± 4.98	7.49 ± 2.83
11	22:16:50.981	-17:18:49.87	26.71 ± 0.06	$3.670^{+0.001}_{-0.001}$	-19.10 ± 0.15	11.16 ± 2.01	1.40 ± 0.25	36.23 ± 8.51	5.17 ± 4.24
12	22:16:53.509	-17:19:06.60	25.74 ± 0.03	$3.671^{+0.001}_{-0.001}$	-20.08 ± 0.06	23.63 ± 1.76	2.96 ± 0.22	31.08 ± 2.99	5.67 ± 2.85
13	22:16:49.716	-17:17:00.96	26.45 ± 0.05	$3.671^{+0.001}_{-0.001}$	-19.41 ± 0.12	8.69 ± 1.12	1.09 ± 0.14	21.37 ± 3.67	7.45 ± 1.80
14	22:16:53.576	-17:19:07.20	24.96 ± 0.01	$3.671^{+0.001}_{-0.001}$	-20.92 ± 0.03	17.97 ± 1.17	2.25 ± 0.15	10.92 ± 0.77	14.77 ± 4.05
15	22:16:51.410	-17:17:50.44	26.02 ± 0.03	$3.672^{+0.001}_{-0.001}$	-19.83 ± 0.08	14.83 ± 1.31	1.86 ± 0.16	24.75 ± 2.90	4.22 ± 1.98
16	22:16:54.326	-17:18:34.98	25.95 ± 0.03	$3.675^{+0.001}_{-0.001}$	-19.95 ± 0.07	6.62 ± 0.81	0.83 ± 0.10	9.85 ± 1.39	5.83 ± 2.25
17	22:16:57.890	-17:21:51.88	26.42 ± 0.05	$3.675^{+0.001}_{-0.001}$	-19.37 ± 0.12	18.62 ± 1.19	2.34 ± 0.15	47.33 ± 6.39	4.28 ± 0.83
18	22:16:51.591	-17:18:12.00	26.30 ± 0.04	$3.681^{+0.001}_{-0.001}$	-19.61 ± 0.10	4.78 ± 0.95	0.60 ± 0.12	9.83 ± 2.17	4.43 ± 2.62
19	22:16:55.554	-17:20:14.08	26.66 ± 0.06	$3.681^{+0.001}_{-0.001}$	-19.14 ± 0.15	12.33 ± 1.31	1.55 ± 0.17	38.80 ± 7.05	5.73 ± 2.17
20	22:16:48.909	-17:15:31.09	26.51 ± 0.05	$3.685^{+0.001}_{-0.001}$	-19.35 ± 0.12	8.96 ± 1.38	1.13 ± 0.17	23.36 ± 4.59	-3.55 ± 6.95
21	22:16:55.005	-17:21:00.75	25.78 ± 0.03	$3.717^{+0.001}_{-0.001}$	-20.06 ± 0.07	22.37 ± 1.51	2.89 ± 0.19	31.09 ± 2.93	9.26 ± 1.83
22	22:16:46.962	-17:21:06.42	25.93 ± 0.03	$3.719^{+0.001}_{-0.001}$	-19.74 ± 0.09	41.34 ± 1.66	5.35 ± 0.21	77.34 ± 7.55	5.17 ± 0.88
23	22:16:46.961	-17:17:10.24	27.19 ± 0.10	$3.720^{+0.001}_{-0.001}$	-18.64 ± 0.24	6.30 ± 0.94	0.81 ± 0.12	32.32 ± 9.19	3.09 ± 2.67
24	22:16:42.903	-17:17:35.09	25.47 ± 0.02	$3.721^{+0.001}_{-0.001}$	-20.44 ± 0.05	14.86 ± 1.46	1.92 ± 0.19	14.53 ± 1.58	2.22 ± 2.25
25	22:16:50.522	-17:18:22.62	26.00 ± 0.03	$3.723^{+0.001}_{-0.001}$	-19.87 ± 0.08	15.39 ± 1.44	2.00 ± 0.19	25.62 ± 3.13	11.86 ± 2.51
26	22:16:49.533	-17:16:44.13	26.38 ± 0.05	$3.728^{+0.001}_{-0.001}$	-19.50 ± 0.11	8.94 ± 1.05	1.16 ± 0.14	20.82 ± 3.35	10.33 ± 3.45

Table 10—Continued

ID	R.A. (J2000)	Decl. (J2000)	m^{a} (mag)	redshift	$M_{\rm UV}$ (mag)	$f_{{\rm Ly}\alpha}$ (10^{-18} erg s^{-1} cm^{-2})	$L_{{\rm Ly}\alpha}$ (10^{42} erg s^{-1})	$EW_{\rm rest}$ (Å)	S_w (Å)
27	22:17:09.126	-17:28:52.31	26.73 ± 0.06	$3.730^{+0.001}_{-0.001}$	-19.07 ± 0.17	11.89 ± 1.54	1.55 ± 0.20	41.26 ± 8.65	3.25 ± 1.57
28	22:16:56.467	-17:17:20.11	26.68 ± 0.06	$3.831^{+0.001}_{-0.001}$	-19.12 ± 0.17	19.18 ± 0.72	2.66 ± 0.10	67.69 ± 11.99	4.13 ± 0.77
29	22:17:01.475	-17:23:58.97	27.01 ± 0.08	$3.837^{+0.001}_{-0.001}$	-18.82 ± 0.23	13.81 ± 1.17	1.92 ± 0.16	64.73 ± 16.19	5.90 ± 1.67
30	22:17:04.114	-17:29:22.86	26.57 ± 0.06	$3.839^{+0.001}_{-0.001}$	-19.29 ± 0.16	19.06 ± 1.23	2.66 ± 0.17	58.23 ± 9.70	3.59 ± 1.20
31	22:16:59.785	-17:26:15.22	25.50 ± 0.02	$3.852^{+0.001}_{-0.001}$	-20.57 ± 0.05	12.90 ± 1.35	1.81 ± 0.19	12.16 ± 1.40	4.41 ± 1.16
32	22:17:00.167	-17:27:32.72	26.70 ± 0.06	$3.854^{+0.001}_{-0.001}$	-19.03 ± 0.19	23.89 ± 1.47	3.36 ± 0.21	93.40 ± 19.22	3.68 ± 2.03
33	22:16:44.680	-17:17:48.48	25.93 ± 0.03	$3.856^{+0.001}_{-0.001}$	-19.49 ± 0.13	75.34 ± 1.29	10.62 ± 0.18	192.60 ± 24.90	1.53 ± 0.42
34	22:16:49.846	-17:17:16.49	26.41 ± 0.05	$4.026^{+0.001}_{-0.001}$	-19.11 ± 0.22	48.03 ± 2.06	7.50 ± 0.32	193.21 ± 43.99	8.03 ± 0.93
35	22:16:51.997	-17:26:10.95	25.85 ± 0.03	$4.076^{+0.001}_{-0.001}$	-20.35 ± 0.08	27.36 ± 1.87	4.40 ± 0.30	36.05 ± 3.71	5.22 ± 1.24
36	22:16:53.458	-17:20:03.45	27.06 ± 0.09	$4.093^{+0.001}_{-0.001}$	-19.19 ± 0.22	7.49 ± 0.66	1.22 ± 0.11	29.18 ± 6.98	7.24 ± 1.49
37	22:16:52.593	-17:29:00.63	26.89 ± 0.08	$4.109^{+0.001}_{-0.001}$	-19.17 ± 0.23	17.48 ± 1.22	2.86 ± 0.20	70.02 ± 17.27	5.76 ± 1.73
38	22:16:59.778	-17:22:16.93	25.75 ± 0.03	$4.126^{+0.001}_{-0.001}$	-20.12 ± 0.11	68.15 ± 2.28	11.28 ± 0.38	115.08 ± 12.30	4.28 ± 0.67
39	22:17:03.102	-17:25:52.33	25.23 ± 0.02	$4.170^{+0.001}_{-0.001}$	-20.63 ± 0.07	120.44 ± 3.00	20.43 ± 0.51	130.16 ± 9.74	11.81 ± 0.64
40	22:16:48.708	-17:15:41.17	26.41 ± 0.05	$4.182^{+0.001}_{-0.001}$	-19.79 ± 0.15	25.01 ± 1.35	4.27 ± 0.23	59.09 ± 9.28	1.45 ± 0.88
41	22:16:49.635	-17:15:26.63	27.50 ± 0.13	$4.220^{+0.001}_{-0.001}$	-18.24 ± 0.54	17.35 ± 1.48	3.03 ± 0.26	173.91 ± 113.30	6.64 ± 1.53
42	22:16:56.050	-17:24:57.12	26.65 ± 0.06	$4.258^{+0.001}_{-0.001}$	-19.59 ± 0.19	22.63 ± 1.57	4.03 ± 0.28	66.48 ± 13.79	6.99 ± 1.76
					D1-*u*drop (30 galaxies)				
1	02:24:33.775	-04:22:05.64	27.48 ± 0.08	$2.730^{+0.001}_{-0.001}$	-17.14 ± 0.33	36.73 ± 4.16	2.26 ± 0.26	357.30 ± 132.78	6.12 ± 1.92
2	02:24:24.047	-04:19:30.14	26.75 ± 0.04	$2.936^{+0.001}_{-0.001}$	-18.82 ± 0.09	11.49 ± 1.98	0.84 ± 0.15	28.27 ± 5.46	5.96 ± 3.75
3	02:24:38.501	-04:19:31.91	25.96 ± 0.02	$2.954^{+0.001}_{-0.001}$	-19.63 ± 0.04	24.14 ± 1.82	1.80 ± 0.14	28.80 ± 2.48	5.79 ± 1.33
4	02:24:32.251	-04:20:05.64	26.36 ± 0.03	$2.961^{+0.001}_{-0.001}$	-19.18 ± 0.07	24.91 ± 1.67	1.87 ± 0.13	45.24 ± 4.18	10.26 ± 1.40
5	02:24:30.247	-04:20:25.53	24.45 ± 0.01	$2.977^{+0.001}_{-0.001}$	-21.21 ± 0.01	52.64 ± 3.69	3.99 ± 0.28	14.85 ± 1.05	11.87 ± 1.47
6	02:24:35.414	-04:20:32.25	26.00 ± 0.02	$3.124^{+0.001}_{-0.001}$	-19.61 ± 0.05	58.84 ± 2.09	5.01 ± 0.18	81.48 ± 5.02	8.38 ± 1.17
7	02:24:32.181	-04:18:52.41	27.00 ± 0.05	$3.127^{+0.001}_{-0.001}$	-18.75 ± 0.12	11.77 ± 2.07	1.01 ± 0.18	36.17 ± 7.54	12.53 ± 5.35
8	02:24:26.931	-04:18:09.40	25.10 ± 0.01	$3.130^{+0.001}_{-0.001}$	-20.77 ± 0.02	16.28 ± 1.97	1.39 ± 0.17	7.81 ± 0.95	1.18 ± 1.96
9	02:24:32.111	-04:19:01.04	26.73 ± 0.04	$3.131^{+0.001}_{-0.001}$	-19.09 ± 0.09	9.38 ± 1.71	0.80 ± 0.15	21.03 ± 4.21	7.64 ± 2.41
10	02:24:32.361	-04:18:33.93	27.32 ± 0.07	$3.132^{+0.001}_{-0.001}$	-18.45 ± 0.15	8.49 ± 1.34	0.73 ± 0.12	34.32 ± 7.41	0.35 ± 3.73
11	02:24:38.052	-04:17:50.69	25.76 ± 0.02	$3.150^{+0.001}_{-0.001}$	-20.08 ± 0.04	18.81 ± 2.10	1.64 ± 0.18	17.21 ± 2.00	6.70 ± 2.73
12	02:24:36.424	-04:20:40.01	27.41 ± 0.08	$3.193^{+0.001}_{-0.001}$	-18.27 ± 0.18	17.26 ± 1.44	1.55 ± 0.13	86.42 ± 17.51	-1.63 ± 4.53
13	02:24:39.007	-04:17:25.43	26.14 ± 0.02	$3.200^{+0.001}_{-0.001}$	-19.77 ± 0.05	14.54 ± 1.65	1.31 ± 0.15	18.37 ± 2.25	6.27 ± 1.62
14	02:24:35.609	-04:19:31.99	27.32 ± 0.07	$3.220^{+0.001}_{-0.001}$	-18.46 ± 0.16	14.64 ± 1.81	1.34 ± 0.17	62.97 ± 12.76	3.07 ± 2.45
15	02:24:36.250	-04:19:11.89	25.81 ± 0.02	$3.258^{+0.001}_{-0.001}$	-20.04 ± 0.04	56.13 ± 2.21	5.29 ± 0.21	57.99 ± 3.23	12.49 ± 1.98
16	02:24:36.988	-04:18:09.47	25.44 ± 0.01	$3.274^{+0.001}_{-0.001}$	-20.53 ± 0.03	42.95 ± 2.36	4.10 ± 0.23	28.53 ± 1.73	14.83 ± 2.07
17	02:24:27.725	-04:17:48.50	27.03 ± 0.06	$3.284^{+0.001}_{-0.001}$	-18.83 ± 0.13	20.07 ± 1.68	1.93 ± 0.16	64.53 ± 9.60	5.80 ± 1.54
18	02:24:35.157	-04:17:00.64	26.61 ± 0.04	$3.344^{+0.001}_{-0.001}$	-19.48 ± 0.08	8.56 ± 1.33	0.86 ± 0.13	15.65 ± 2.68	7.98 ± 2.43
19	02:24:28.399	-04:20:01.41	26.27 ± 0.03	$3.351^{+0.001}_{-0.001}$	-19.77 ± 0.06	23.60 ± 1.80	2.38 ± 0.18	33.30 ± 3.16	10.49 ± 1.71
20	02:24:38.367	-04:17:16.11	27.34 ± 0.07	$3.357^{+0.001}_{-0.001}$	-18.71 ± 0.15	7.92 ± 1.12	0.80 ± 0.11	29.73 ± 6.09	3.94 ± 1.62
21	02:24:41.996	-04:18:59.15	27.01 ± 0.05	$3.400^{+0.001}_{-0.001}$	-19.11 ± 0.11	12.78 ± 1.57	1.33 ± 0.16	34.43 ± 5.69	10.15 ± 2.55

Table 10—Continued

ID	R.A. (J2000)	Decl. (J2000)	m^{a} (mag)	redshift	$M_{\rm UV}$ (mag)	$f_{{\rm Ly}\alpha}$ (10^{-18} erg s^{-1} cm^{-2})	$L_{{\rm Ly}\alpha}$ (10^{42} erg s^{-1})	$EW_{\rm rest}$ (Å)	S_w (Å)
22	02:24:37.488	-04:19:20.22	26.12 ± 0.02	$3.426^{+0.001}_{-0.001}$	-20.02 ± 0.05	34.92 ± 1.95	3.71 ± 0.21	41.50 ± 3.12	9.26 ± 0.97
23	02:24:28.416	-04:21:30.12	26.78 ± 0.04	$3.435^{+0.001}_{-0.001}$	-19.32 ± 0.10	23.86 ± 1.70	2.55 ± 0.18	54.13 ± 6.44	3.95 ± 0.73
24	02:24:36.548	-04:18:26.31	26.56 ± 0.04	$3.454^{+0.001}_{-0.001}$	-19.61 ± 0.08	21.02 ± 1.16	2.28 ± 0.13	37.07 ± 3.42	7.23 ± 1.34
25	02:24:35.602	-04:16:54.03	27.31 ± 0.07	$3.455^{+0.001}_{-0.001}$	-18.60 ± 0.19	26.89 ± 1.59	2.92 ± 0.17	119.80 ± 23.53	3.58 ± 1.71
26	02:24:44.626	-04:19:35.65	26.24 ± 0.03	$3.463^{+0.001}_{-0.001}$	-19.95 ± 0.06	30.63 ± 1.60	3.34 ± 0.17	39.74 ± 3.03	7.64 ± 2.19
27	02:24:38.037	-04:22:12.46	27.49 ± 0.08	$3.529^{+0.001}_{-0.001}$	-18.67 ± 0.19	20.88 ± 1.47	2.38 ± 0.17	91.63 ± 19.14	9.51 ± 2.56
28	02:24:29.531	-04:21:43.03	26.83 ± 0.05	$3.550^{+0.001}_{-0.001}$	-19.45 ± 0.10	29.51 ± 2.19	3.41 ± 0.25	64.39 ± 8.00	3.44 ± 2.08
29	02:24:35.608	-04:21:10.87	27.10 ± 0.06	$3.551^{+0.001}_{-0.001}$	-19.25 ± 0.12	14.71 ± 1.57	1.70 ± 0.18	38.72 ± 6.21	11.86 ± 3.78
30	02:24:24.653	-04:19:31.71	26.99 ± 0.05	$3.555^{+0.001}_{-0.001}$	-19.40 ± 0.11	11.07 ± 1.24	1.29 ± 0.14	25.39 ± 3.88	3.50 ± 3.09
				D4-$u$drop (16 galaxies)					
1	22:14:03.642	-18:00:09.90	26.61 ± 0.04	$2.973^{+0.001}_{-0.001}$	-19.05 ± 0.08	6.08 ± 1.27	0.46 ± 0.10	12.47 ± 2.79	3.65 ± 6.22
2	22:13:58.570	-17:59:30.91	27.05 ± 0.06	$3.008^{+0.001}_{-0.001}$	-18.60 ± 0.13	7.66 ± 1.28	0.60 ± 0.10	24.50 ± 5.14	0.09 ± 1.53
3	22:14:11.265	-17:59:56.51	25.84 ± 0.02	$3.037^{+0.001}_{-0.001}$	-19.70 ± 0.05	57.83 ± 2.77	4.61 ± 0.22	68.72 ± 4.69	7.67 ± 0.97
4	22:13:53.488	-17:56:54.74	26.56 ± 0.04	$3.046^{+0.001}_{-0.001}$	-18.95 ± 0.10	33.35 ± 2.43	2.67 ± 0.19	80.04 ± 9.72	5.06 ± 1.72
5	22:13:51.171	-17:57:18.84	26.66 ± 0.04	$3.138^{+0.001}_{-0.001}$	-19.15 ± 0.09	11.14 ± 1.56	0.96 ± 0.13	23.74 ± 3.92	4.81 ± 1.76
6	22:13:53.773	-17:57:40.48	27.09 ± 0.06	$3.210^{+0.001}_{-0.001}$	-18.79 ± 0.13	9.29 ± 1.75	0.84 ± 0.16	29.27 ± 6.72	4.17 ± 1.95
7	22:13:54.597	-17:59:06.04	26.79 ± 0.05	$3.241^{+0.001}_{-0.001}$	-19.12 ± 0.10	13.84 ± 1.33	1.29 ± 0.12	32.89 ± 4.58	2.97 ± 4.01
8	22:13:55.114	-17:59:55.62	26.26 ± 0.03	$3.242^{+0.001}_{-0.001}$	-19.68 ± 0.06	16.00 ± 1.44	1.49 ± 0.13	22.77 ± 2.46	3.70 ± 2.06
9	22:14:04.835	-17:57:44.20	26.93 ± 0.06	$3.243^{+0.001}_{-0.001}$	-18.81 ± 0.14	27.86 ± 1.96	2.60 ± 0.18	88.14 ± 13.39	9.82 ± 1.41
10	22:14:04.154	-18:00:05.58	26.72 ± 0.05	$3.243^{+0.001}_{-0.001}$	-19.11 ± 0.11	23.82 ± 1.90	2.22 ± 0.18	56.94 ± 7.36	7.18 ± 1.45
11	22:14:03.430	-17:59:22.71	26.03 ± 0.02	$3.249^{+0.001}_{-0.001}$	-19.90 ± 0.05	24.84 ± 1.88	2.32 ± 0.18	28.98 ± 2.62	5.89 ± 1.17
12	22:14:09.396	-17:57:58.56	26.98 ± 0.06	$3.336^{+0.001}_{-0.001}$	-19.12 ± 0.11	3.32 ± 0.73	0.33 ± 0.07	8.44 ± 2.09	4.28 ± 10.94
13	22:14:16.330	-17:57:22.22	27.54 ± 0.10	$3.341^{+0.001}_{-0.001}$	-18.46 ± 0.21	9.19 ± 1.56	0.92 ± 0.16	43.24 ± 11.65	6.27 ± 2.88
14	22:14:09.371	-17:58:15.61	26.99 ± 0.06	$3.341^{+0.001}_{-0.001}$	-19.02 ± 0.13	13.93 ± 1.74	1.39 ± 0.17	39.00 ± 6.87	4.65 ± 2.26
15	22:13:58.117	-17:59:46.75	26.92 ± 0.06	$3.560^{+0.001}_{-0.001}$	-19.48 ± 0.11	12.41 ± 1.54	1.44 ± 0.18	26.50 ± 4.40	5.63 ± 1.58
16	22:14:07.173	-18:00:24.05	26.48 ± 0.04	$3.635^{+0.001}_{-0.001}$	-20.03 ± 0.08	37.94 ± 2.08	4.65 ± 0.26	51.22 ± 4.73	8.40 ± 1.04

[a]The apparent magnitude of detection-band: i-band for u-, g-, and r-dropout, and z-band for i-dropout galaxies.

Table 11. Results of the protocluster confirmation

Name	$N_{\rm obs}$	$N_{\rm det}$	Protocluster?	$N_{\rm member}$	redshift	σ_v (km s^{-1})
SDF-*i*drop	53	28	Yes	10	6.01	906 ± 188
D1-*i*drop	8	3	unclear	—	—	—
D3-*i*drop	8	2	possible	2	5.75	—
D1-*r*drop	15	6	possible	2	4.89	—
D4-*r*drop	12	3	unclear	—	—	—
D1-*g*drop	123	36	No	—	—	—
D4-*g*drop	144	42	Yes	11	3.67	352 ± 140
D1-*u*drop	95	30	Yes	5	3.13	235 ± 75
D4-*u*drop	57	16	Yes	5	3.24	61 ± 105

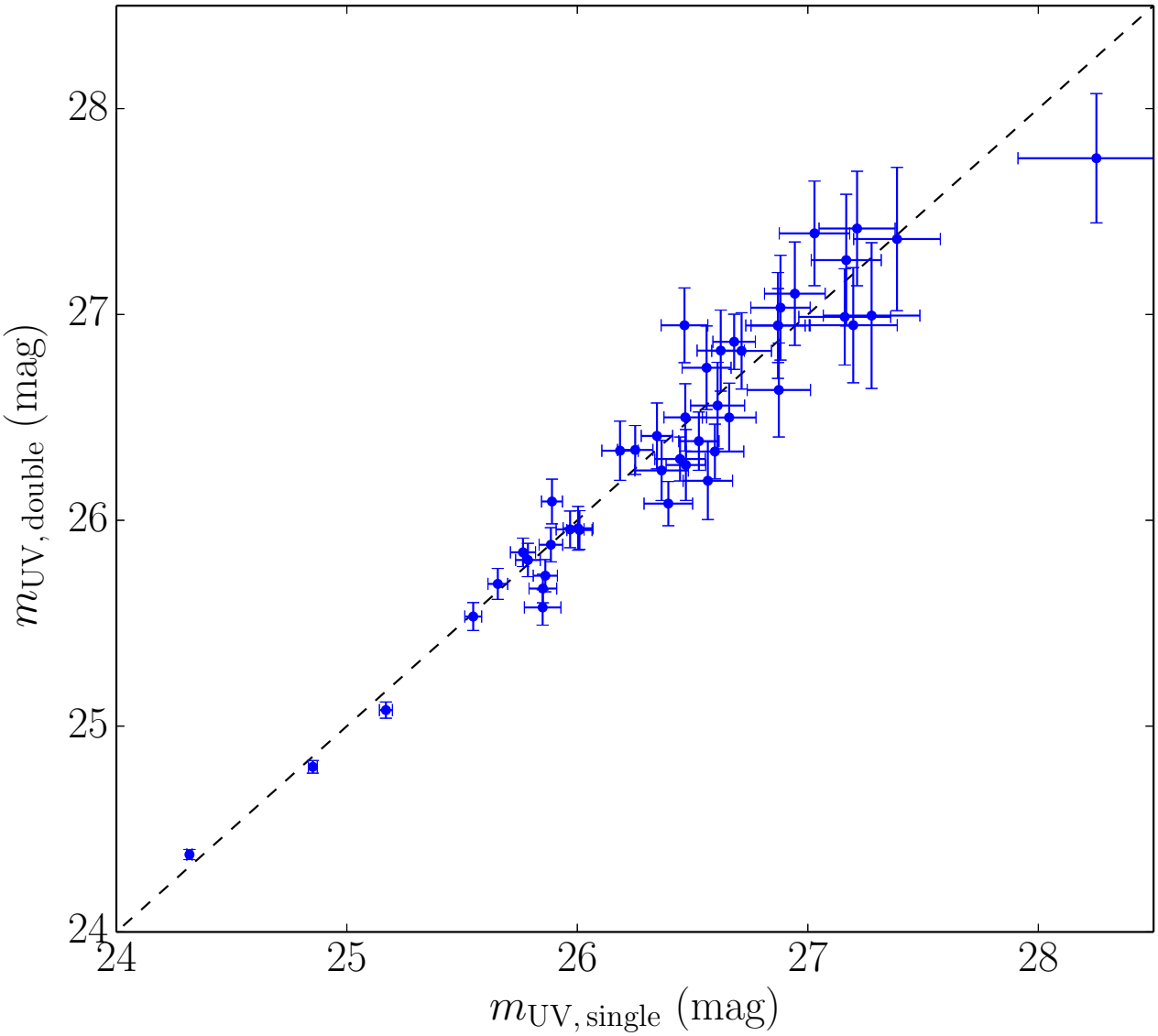

Fig. 17.— Consistency check between two different methods of estimating UV luminosity for u-dropout galaxies. The $m_{\mathrm{UV,single}}$ is the UV luminosity derived by g-band magnitude corrected Lyα flux and IGM absorption. The $m_{\mathrm{UV,double}}$ is the UV luminosity derived by the extrapolation of $r-i$ color.

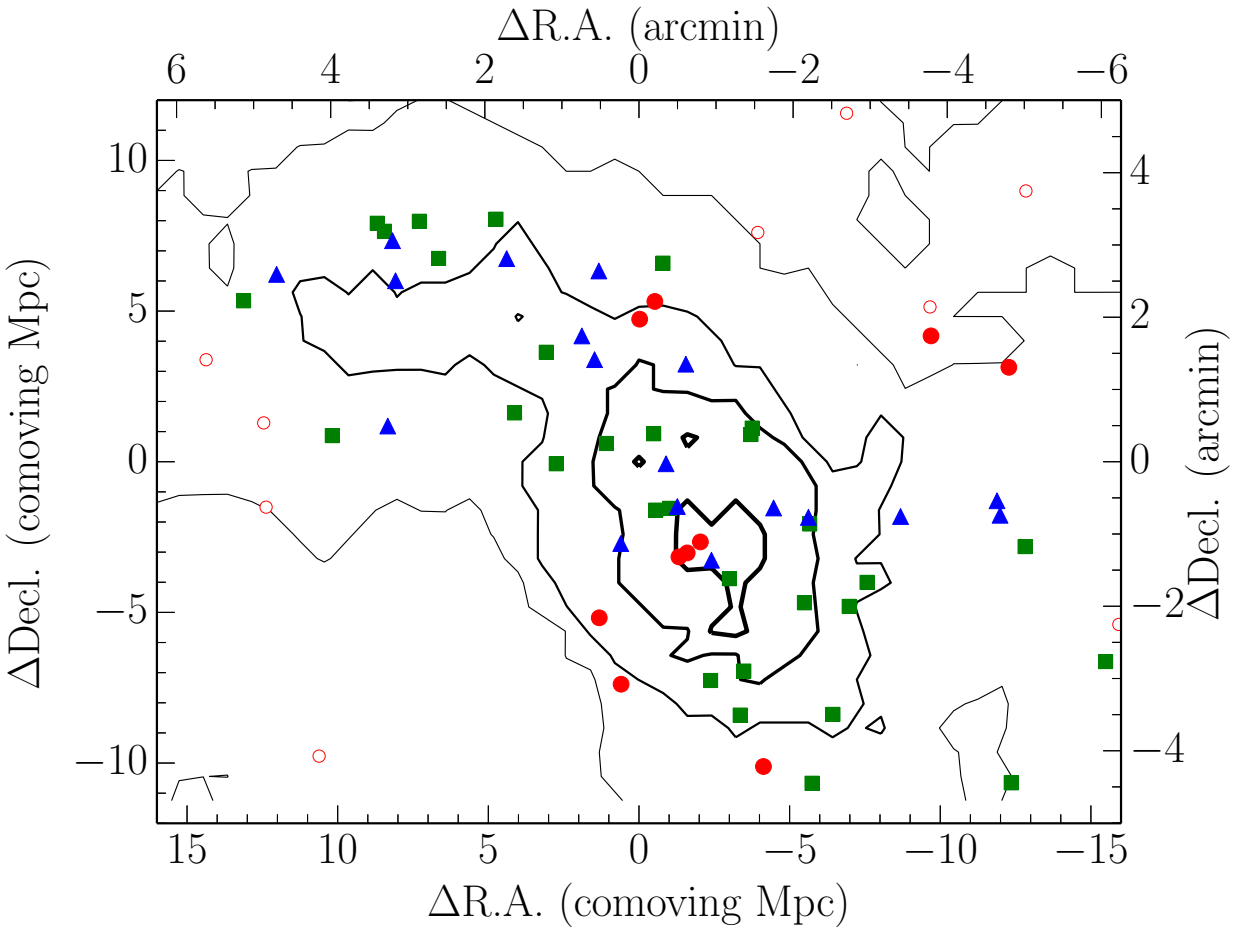

Fig. 18.— Sky distribution of the i-dropout galaxies and number density contours in/around the SDF-$i$drop region. Spectroscopically observed galaxies are marked by filled symbols (red circles: protocluster galaxies, blue triangles: field galaxies, green squares: Lyα undetected objects), and spectroscopically unobserved galaxies are shown by open circles. The origin (0,0) is (R.A., Decl.) = $(13:24:29.0, +27:17:19.1)$, which is defined as the center of the figure. The lines show the number density contours of i-dropout galaxies from 6σ to 0σ with a step of 2σ. It can be clearly seen that all i-dropout galaxies in/around the overdense region were spectroscopically observed.

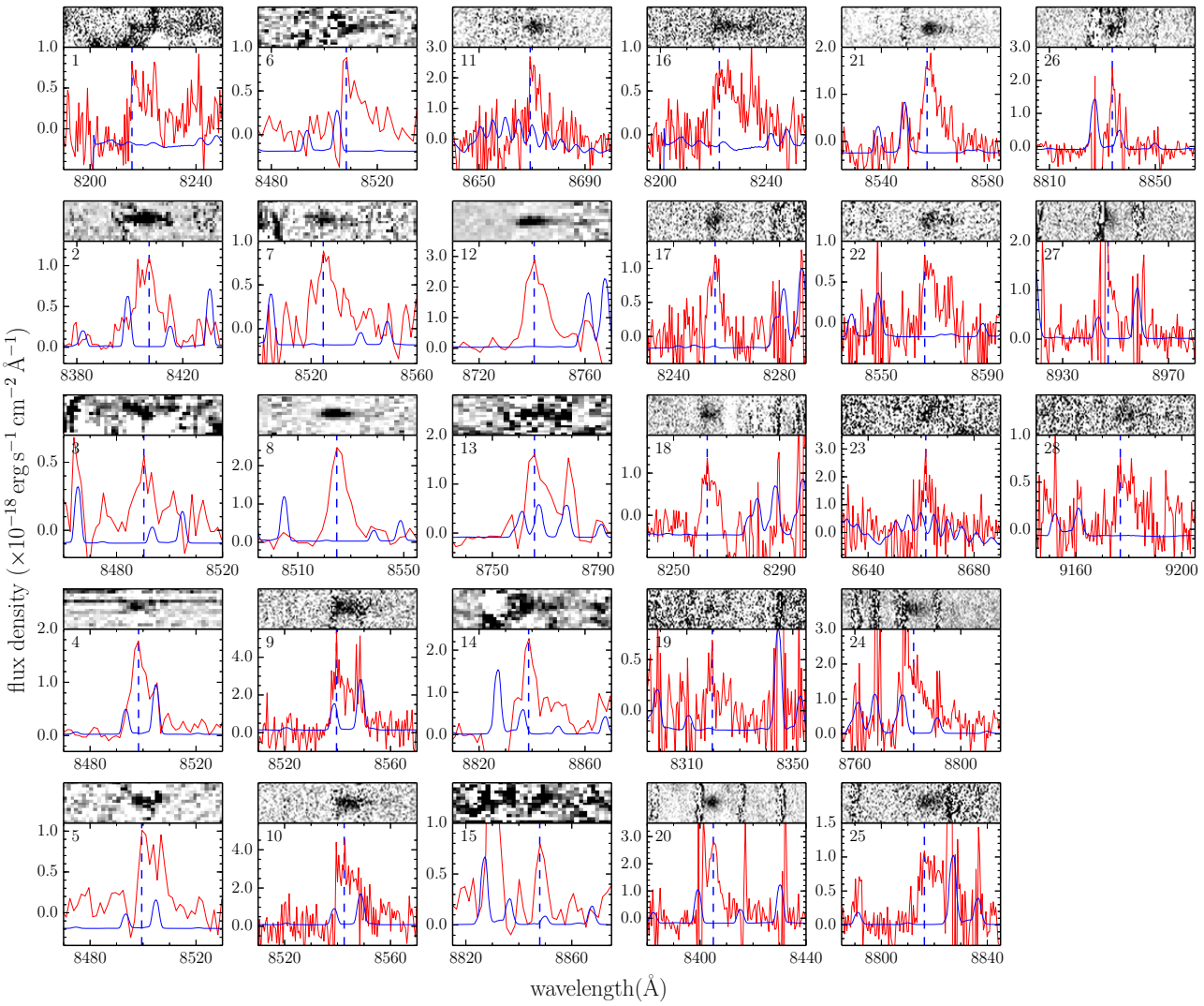

Fig. 19.— Spectra of 28 galaxies having a Lyα emission line in/around the SDF-*i*drop region. The vertical dashed lines indicate the peak of the Lyα emission line. The blue solid lines represent the sky lines. The object IDs are indicated at the upper left corner (Column 1 of Table 10).

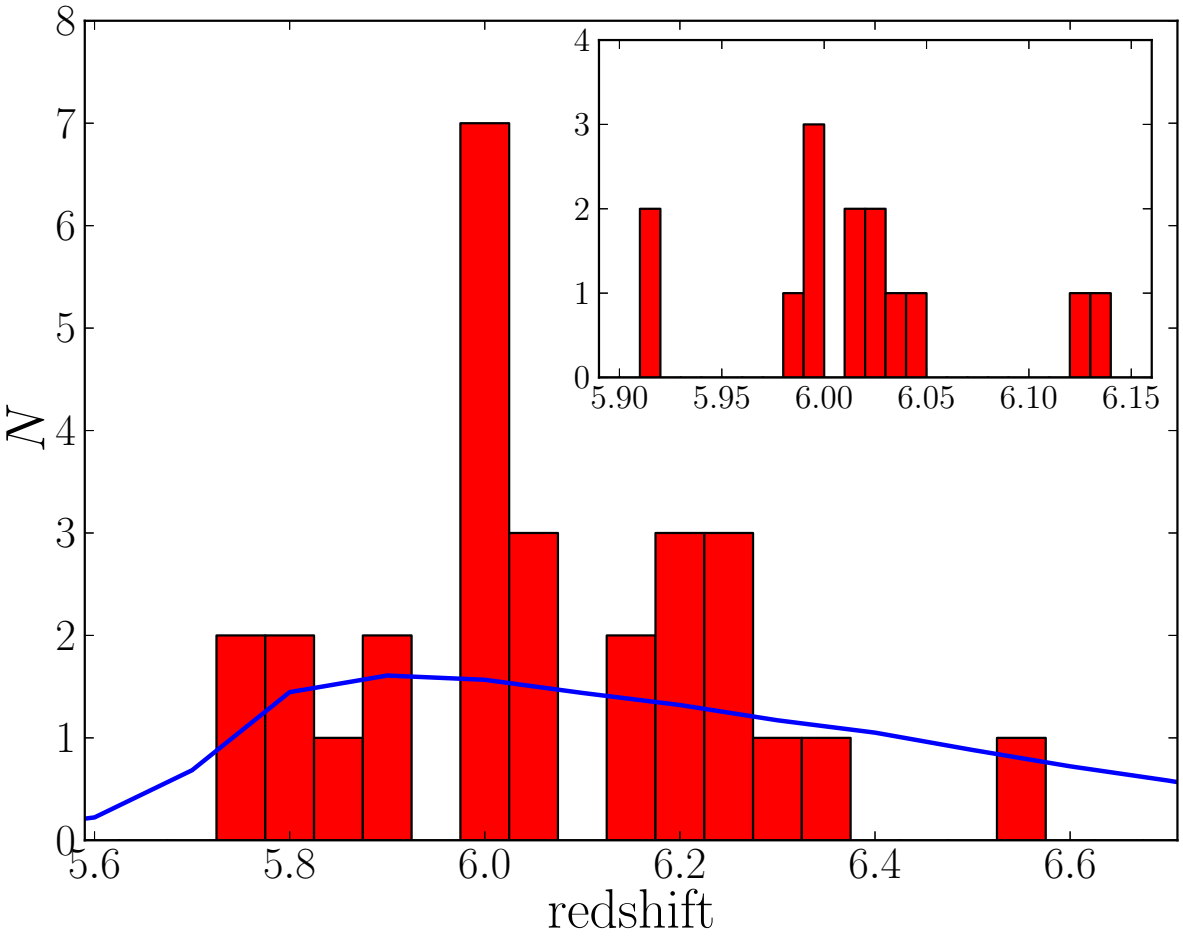

Fig. 20.— Redshift distribution of the 28 spectroscopically confirmed galaxies in/around the SDF-*i*drop region. The bin size is $\Delta z = 0.05$. The solid (blue) line shows the selection function of our *i*-dropout selection assuming a uniform distribution normalized to the total number of confirmed emitters. The inset is a close-up of the protocluster redshift range, with a bin size of $\Delta z = 0.01$.

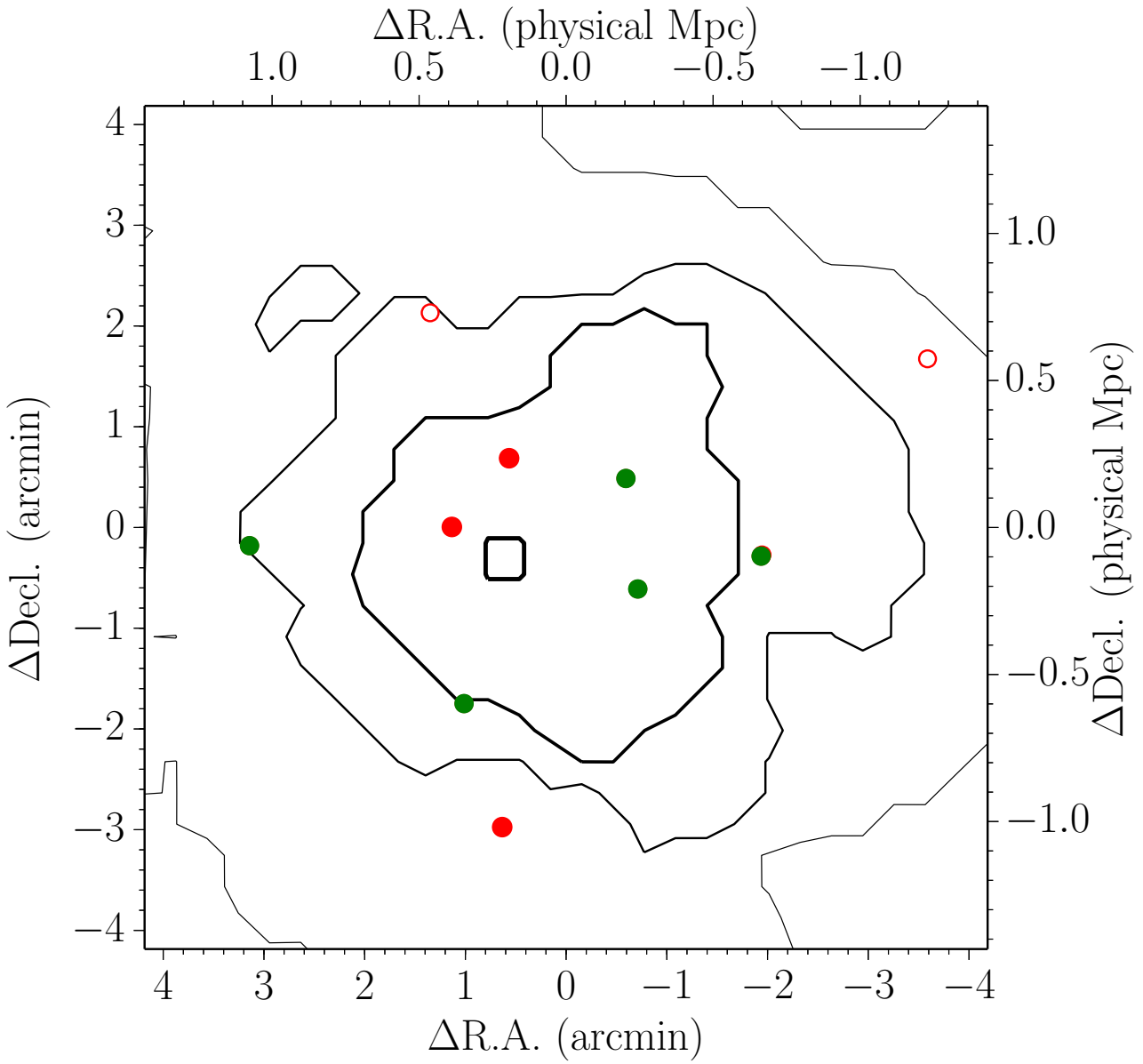

Fig. 21.— Sky distribution of i-dropout galaxies and number density contours in the D1-$i$drop region. Spectroscopically observed galaxies are marked by filled circles (red: Lyα detected galaxies, green: Lyα undetected galaxies), and spectroscopically unobserved galaxies are shown by open circles. The origin (0,0) is (R.A., Decl.) = (02 : 27 : 16.5, −04 : 50 : 49.6), which is defined as the center of the figure. The lines show the number density contours of i-dropout galaxies from 6σ to 0σ with a step of 2σ.

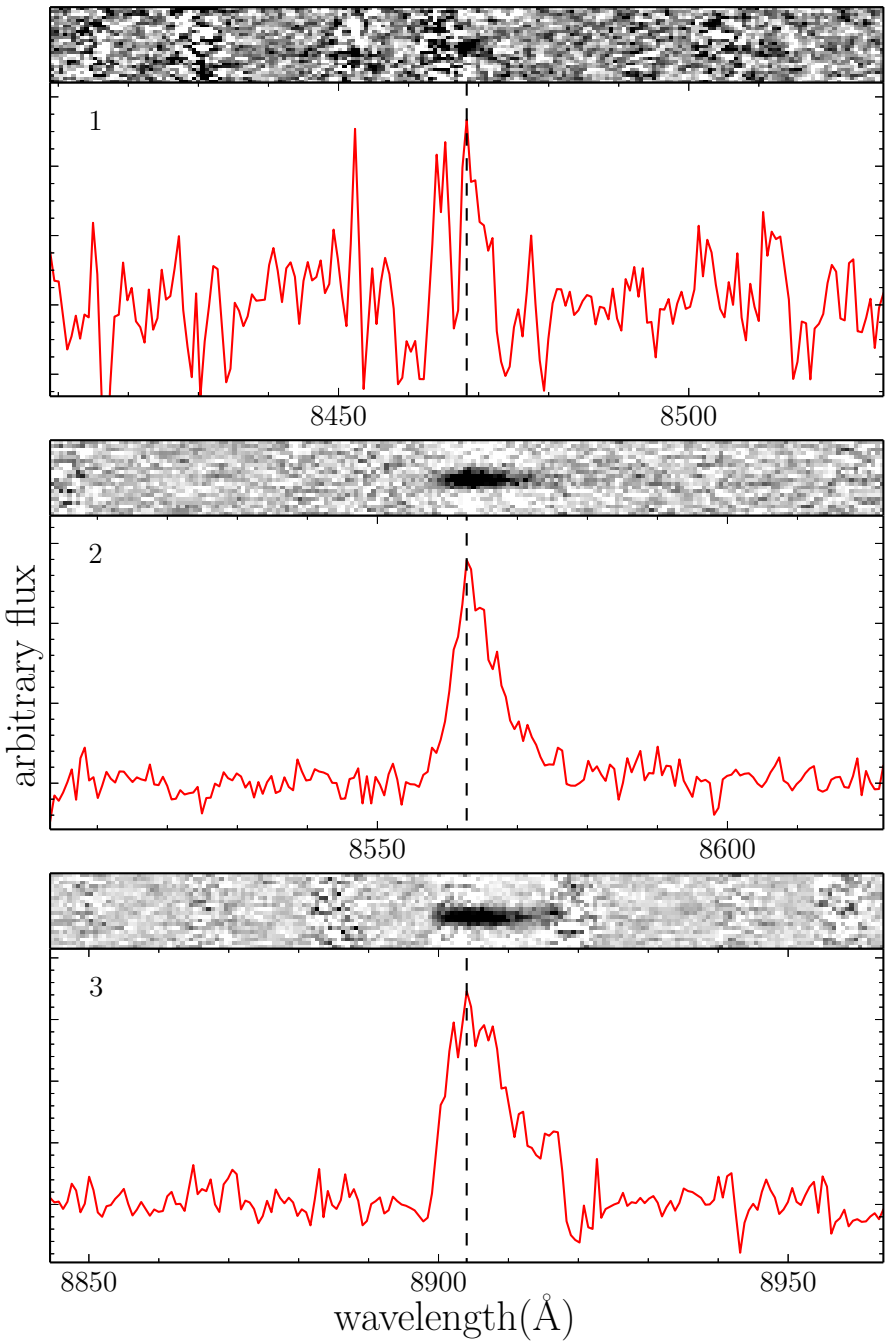

Fig. 22.— Spectra of three r-dropout galaxies having Lyα emission line in D1-$i$drop region. The object IDs are indicated at the upper left corner (Column 1 of Table 10).

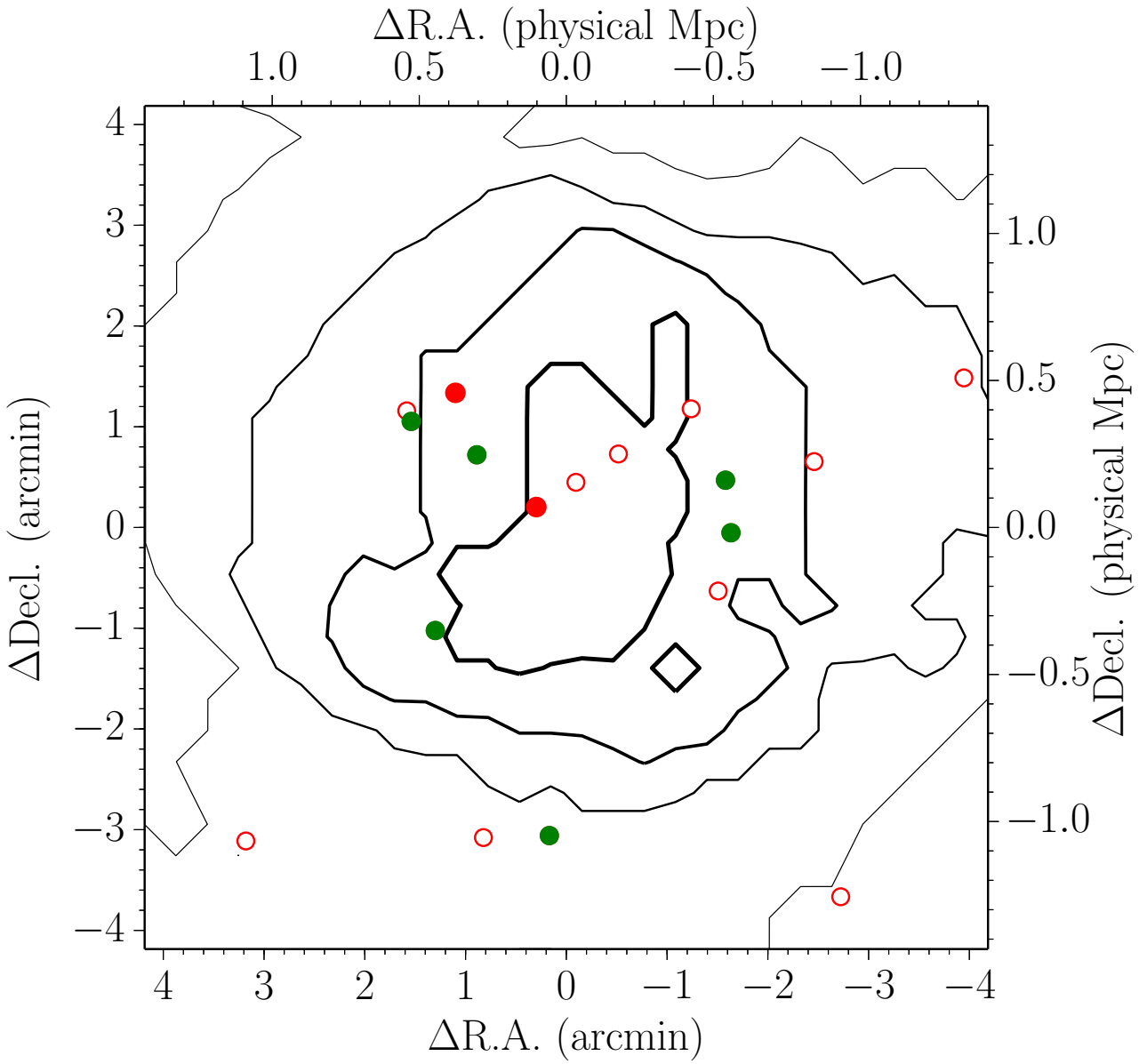

Fig. 23.— Sky distribution of i-dropout galaxies and number density contours in the D3-$i$drop region. Spectroscopically observed galaxies are marked by filled circles (red: Lyα detected galaxies, green: Lyα undetected galaxies), and spectroscopically unobserved galaxies are shown by open circles. The origin (0,0) is (R.A., Decl.) = $(14:19:15.2, +52:56:02.2)$, which is defined as the center of the figure. The lines show the number density contours of i-dropout galaxies from 6σ to 0σ with a step of 2σ.

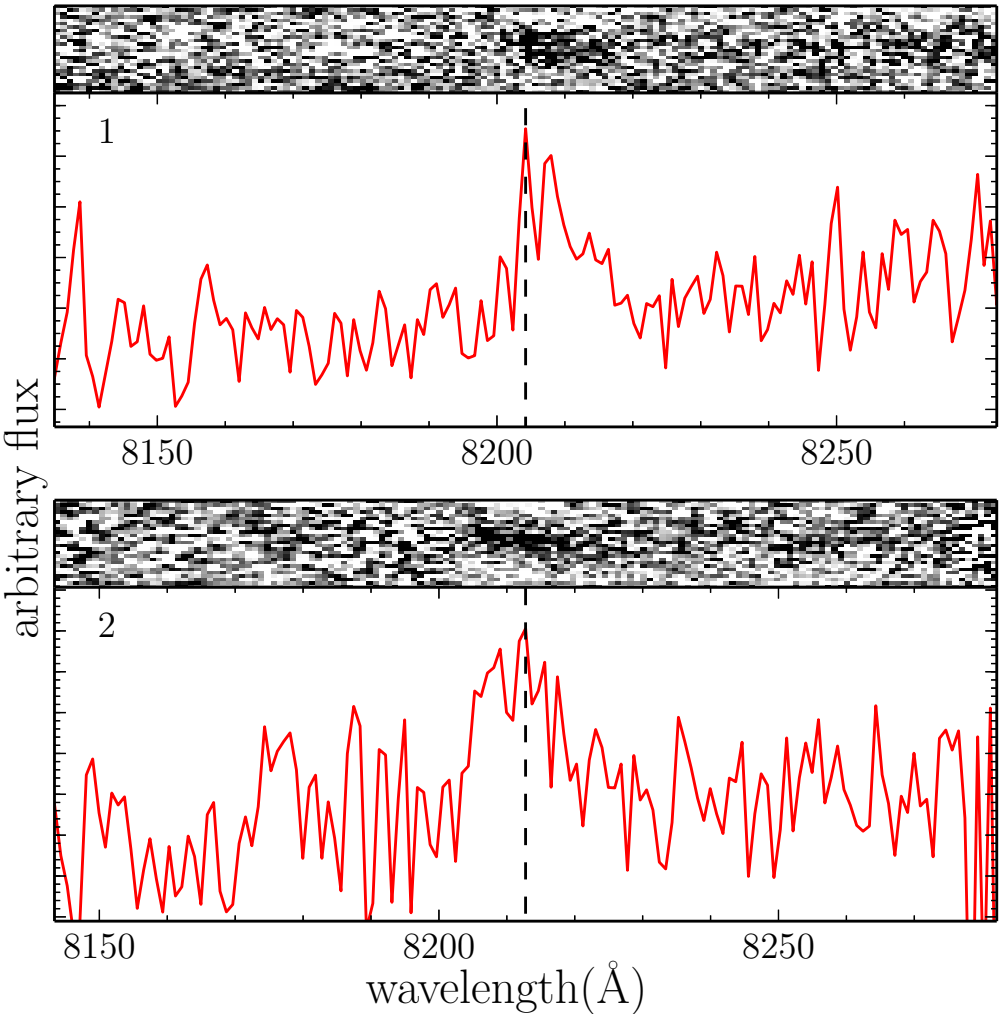

Fig. 24.— Spectra of two i-dropout galaxies having Lyα emission line in D3-$i$drop region. The object IDs are indicated at the upper left corner (Column 1 of Table 10).

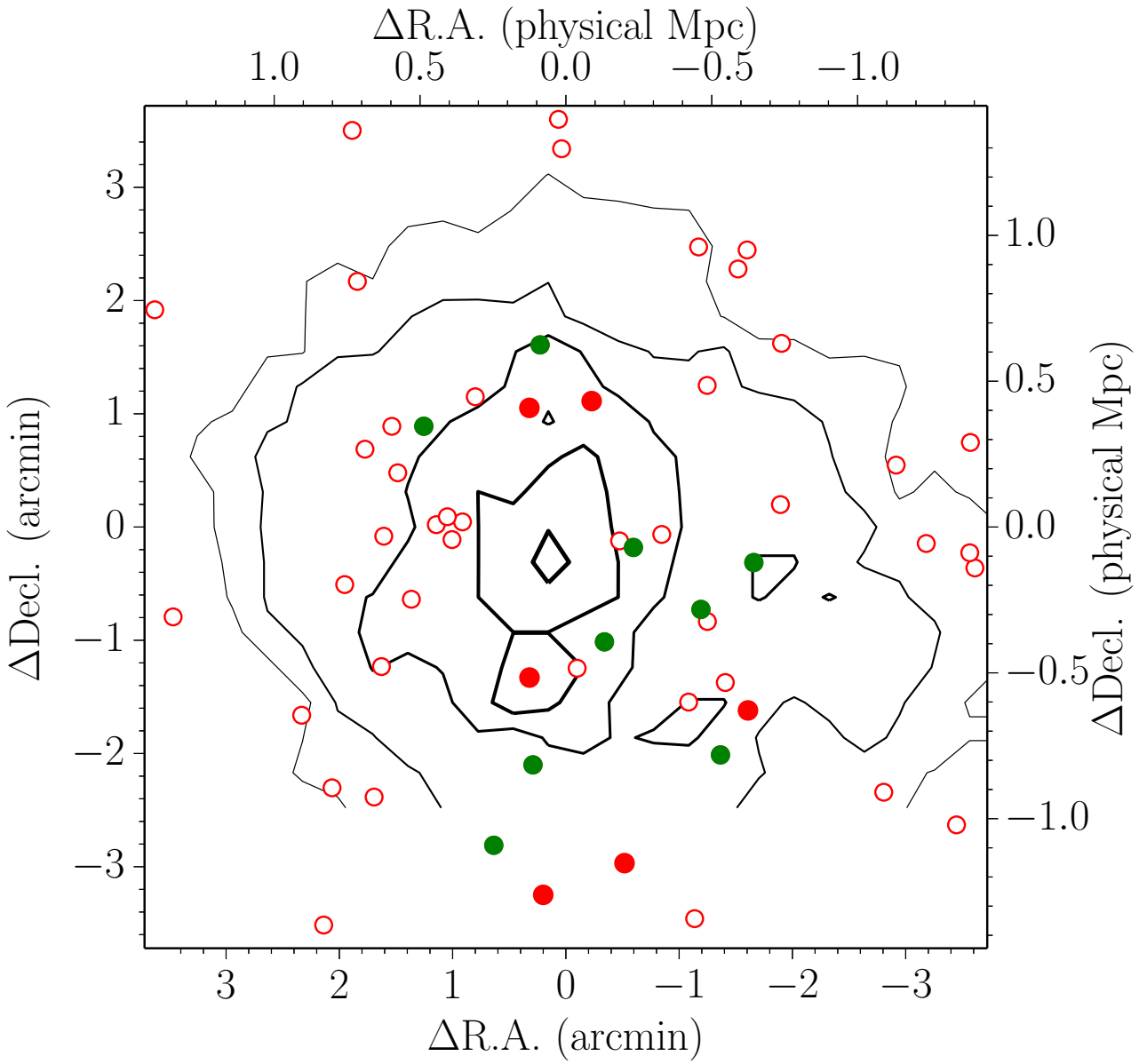

Fig. 25.— Sky distribution of r-dropout galaxies and number density contours in the D1-$r$drop region. Spectroscopically observed galaxies are marked by filled circles (red: Lyα detected galaxies, green: Lyα undetected galaxies), and spectroscopically unobserved galaxies are shown by open circles. The origin (0,0) is (R.A., Decl.) = (02 : 24 : 44.7, −04 : 55 : 37.9), which is defined as the center of the figure. The lines show the number density contours of i-dropout galaxies from 4σ to 0σ with a step of 1σ.

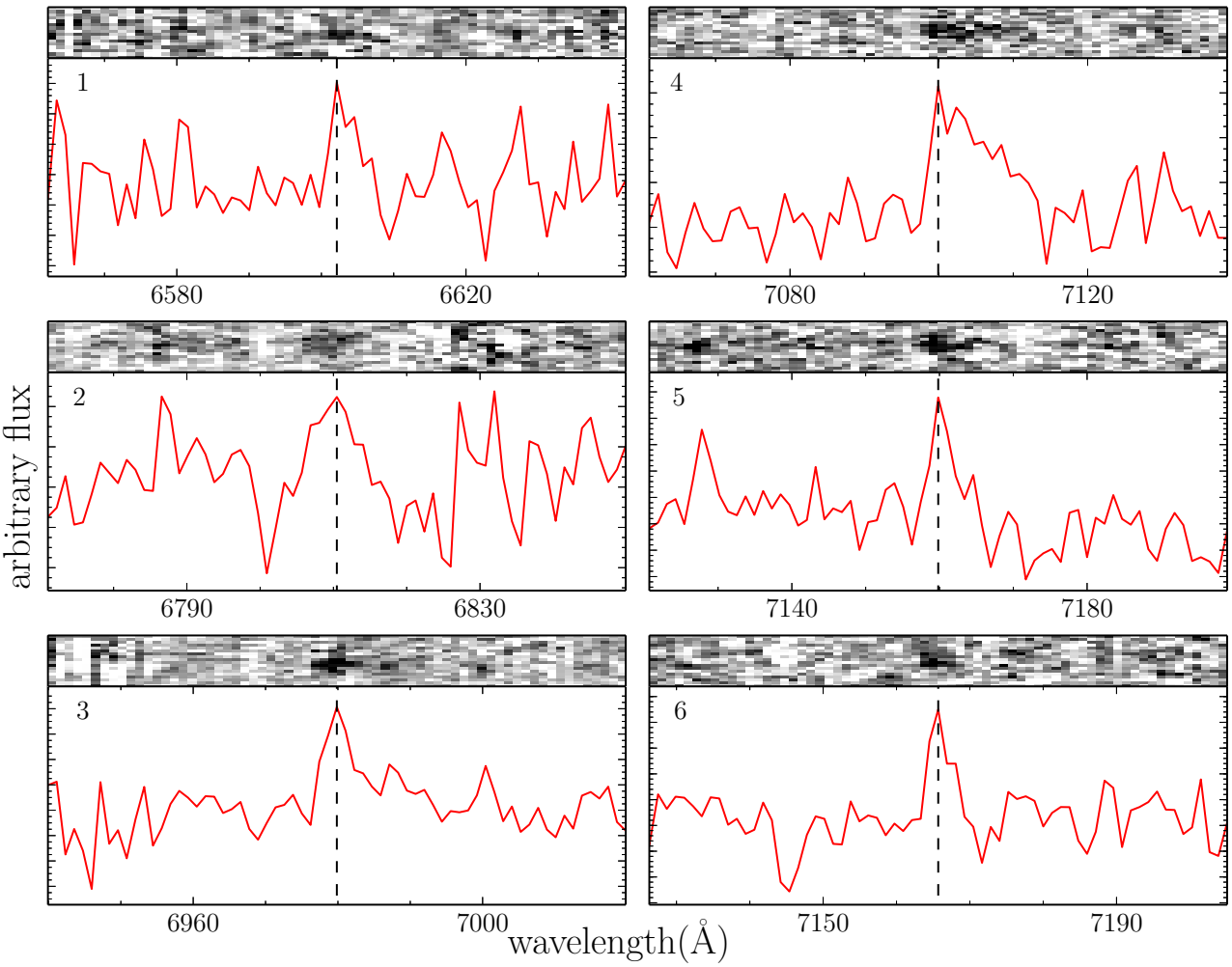

Fig. 26.— Spectra of six r-dropout galaxies having Lyα emission line in the D1-$r$drop region. The object IDs are indicated at the upper left corner (Column 1 of Table 10).

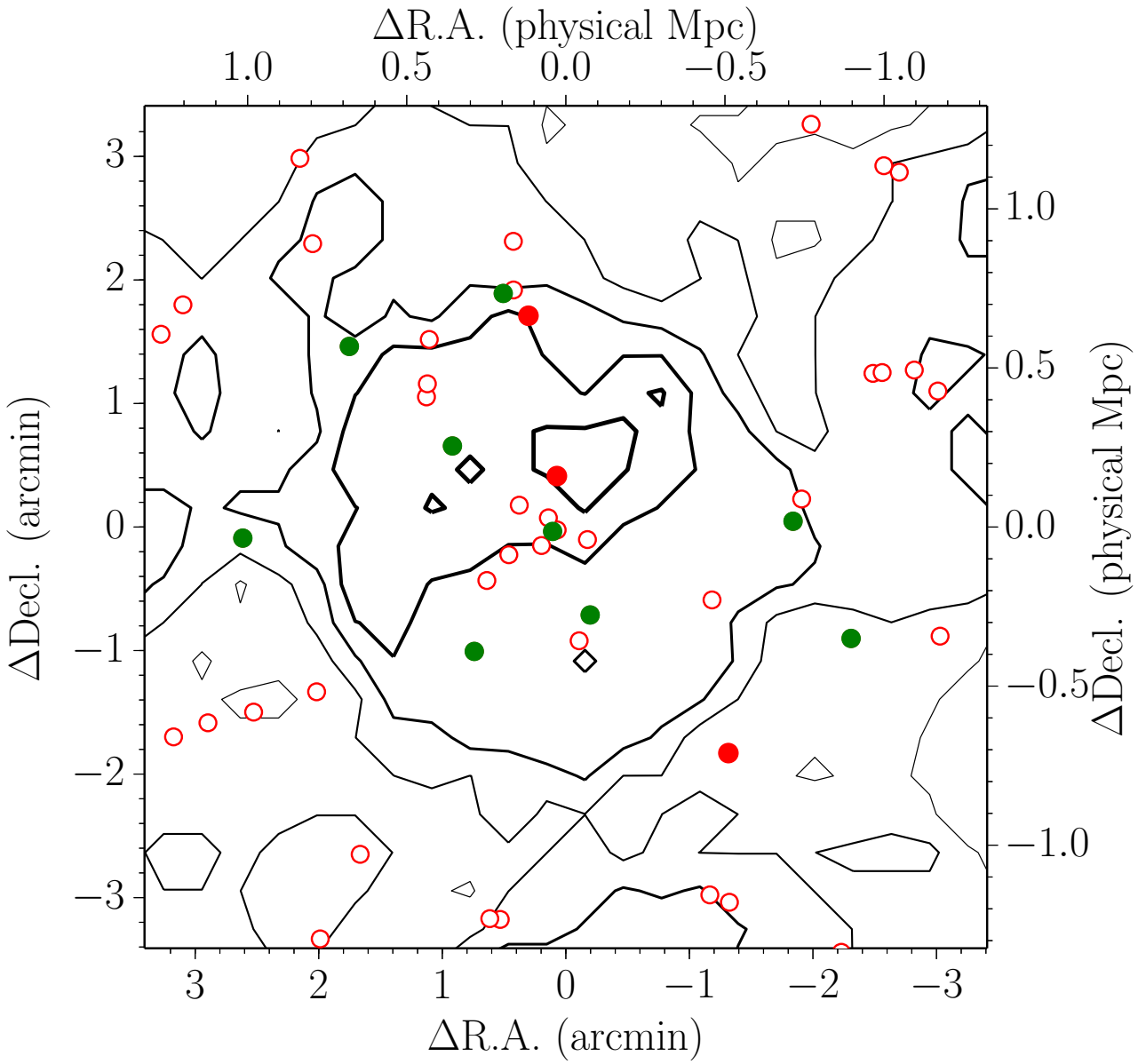

Fig. 27.— Sky distribution of r-dropout galaxies and number density contours in the D4-$r$drop region. Spectroscopically observed galaxies are marked by filled circles (red: Lyα detected galaxies, green: Lyα undetected galaxies), and spectroscopically unobserved galaxies are shown by open circles. The origin (0,0) is (R.A., Decl.) = $(22:16:45.5, -17:29:44.7)$, which is defined as the center of the figure. The lines show the number density contours of i-dropout galaxies from 4σ to 0σ with a step of 1σ.

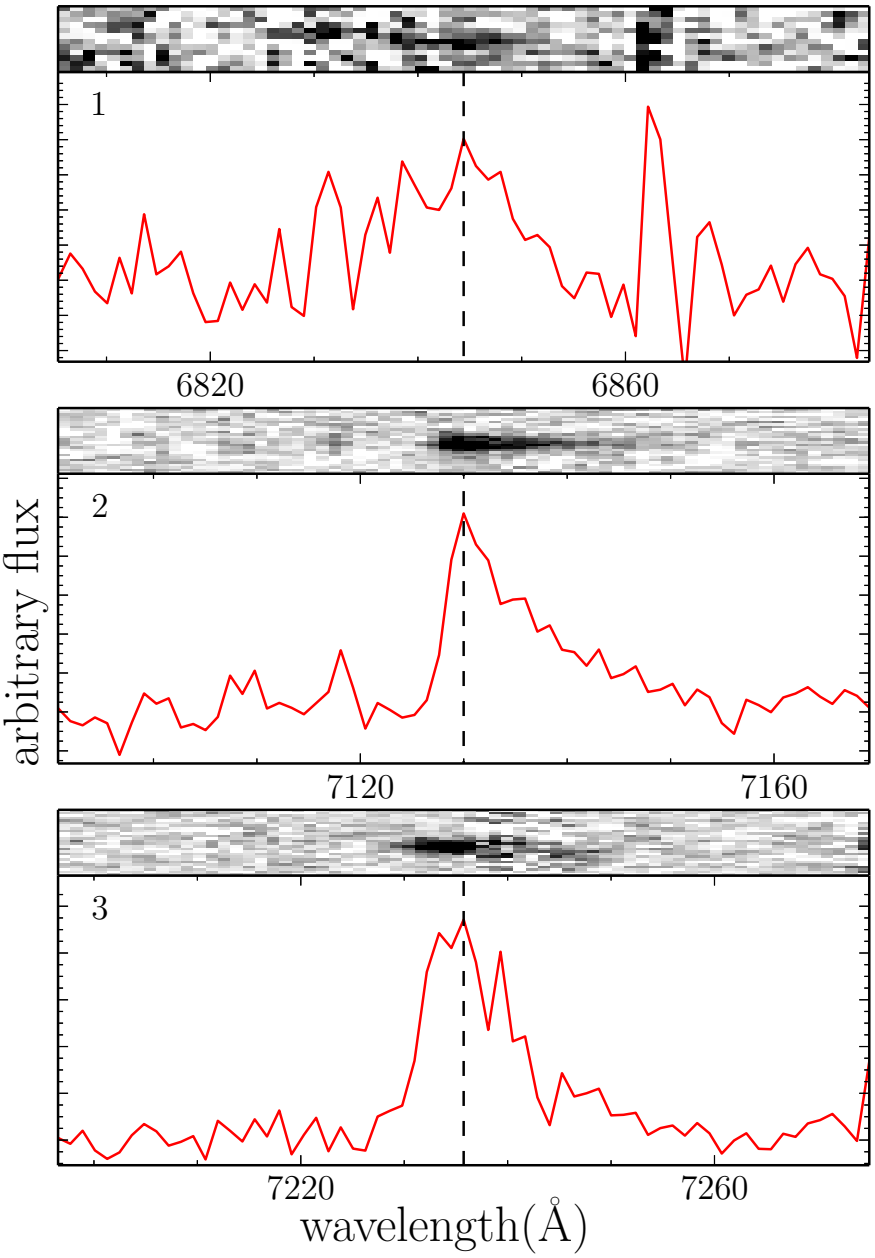

Fig. 28.— Spectra of two r-dropout galaxies having Lyα emission line in the D4-$r$drop region. The object IDs are indicated at the upper left corner (Column 1 of Table 10).

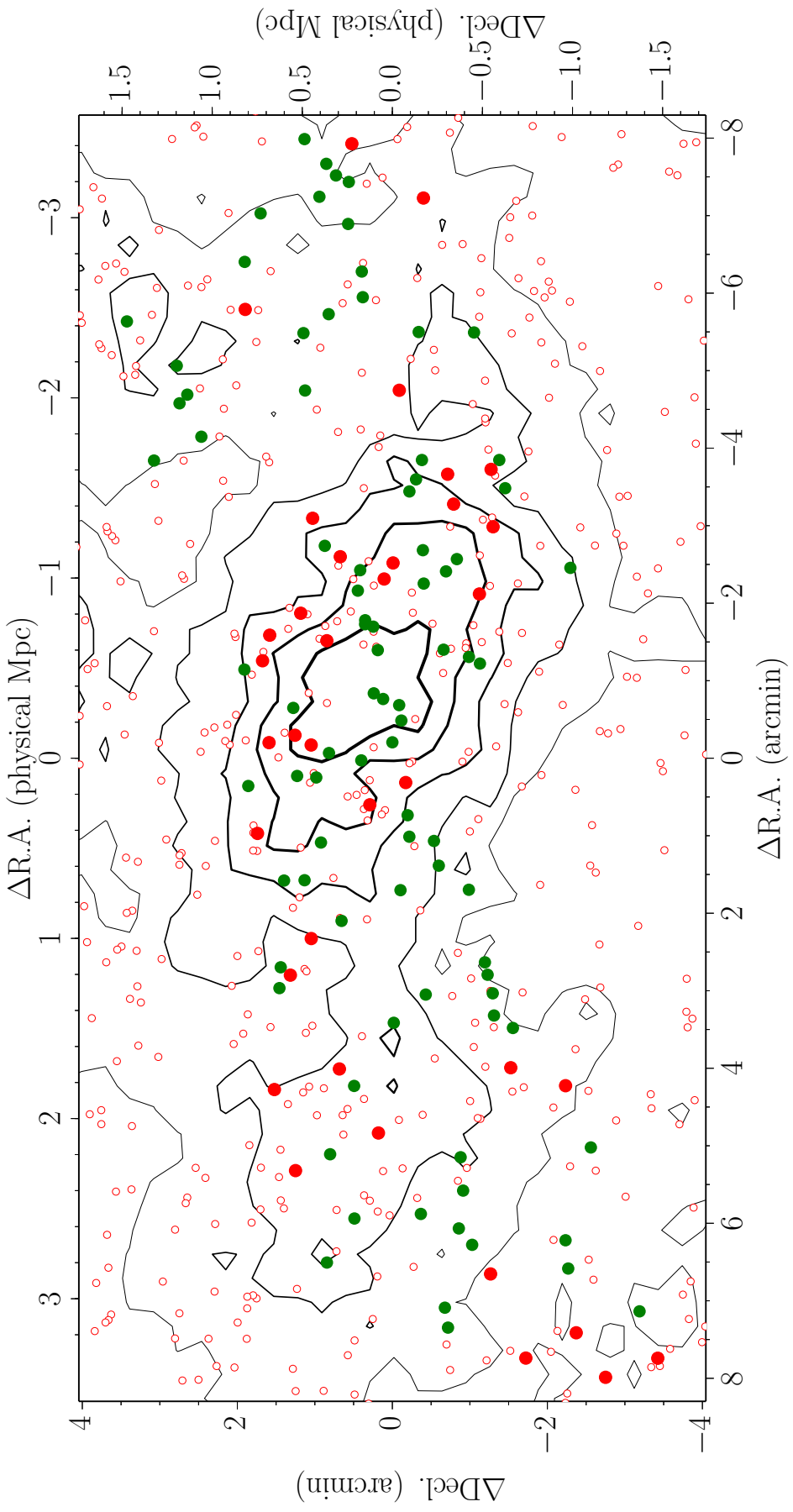

Fig. 29.— Sky distribution of g-dropout galaxies and number density contours in/around the D1-$g$drop region. Spectroscopically observed galaxies are marked by filled circles (red: Lyα detected galaxies, green: Lyα undetected galaxies), and spectroscopically unobserved galaxies are shown by open circles. The origin (0,0) is (R.A., Decl.) = (02 : 25 : 40.5, −04 : 15 : 56.3), which is defined as the center of the figure. The lines show the number density contours of i-dropout galaxies from 4σ to 0σ with a step of 1σ.

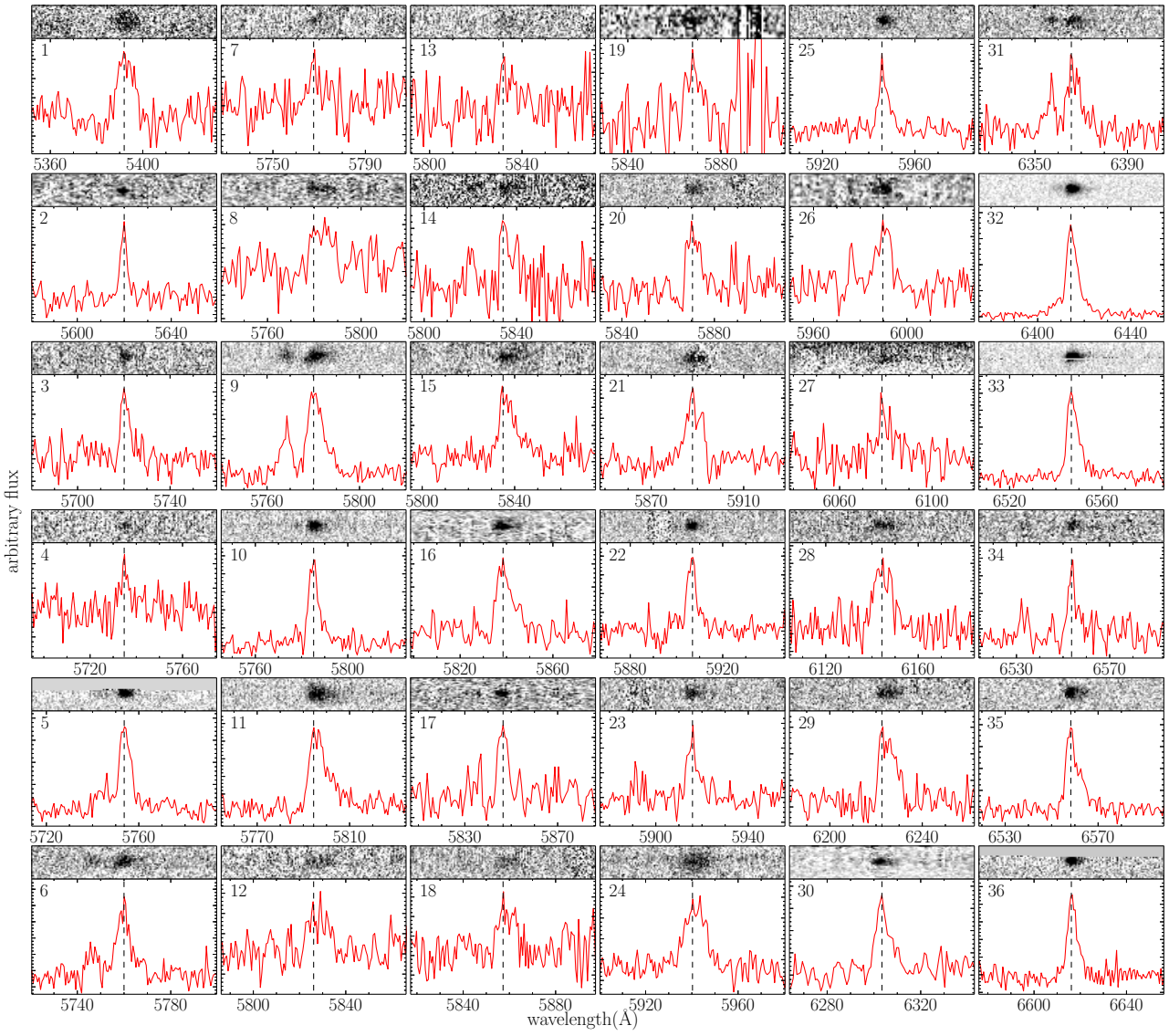

Fig. 30.— Spectra of 36 g-dropout galaxies having a Lyα emission line in/around the D1-$g$drop region. The object IDs are indicated at the upper left corner (Column 1 of Table 10).

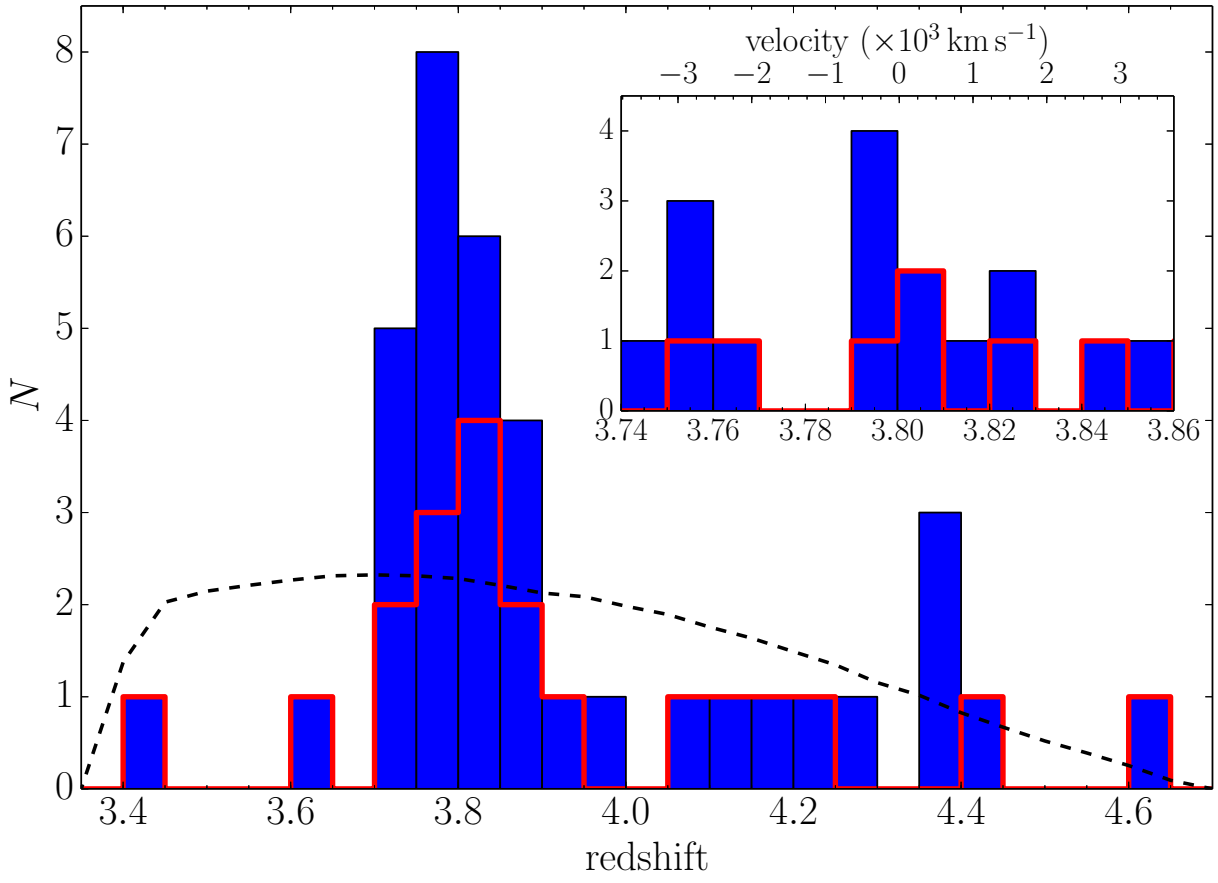

Fig. 31.— Redshift distribution of 36 g-dropout with the bin size of $\Delta z = 0.05$ in/around the D1-$g$drop region. Blue histogram shows all 36 galaxies, and red line shows galaxies only in the D1-$g$drop. The inset is a close-up of the protocluster redshift range, with a bin size of $\Delta z = 0.01$.

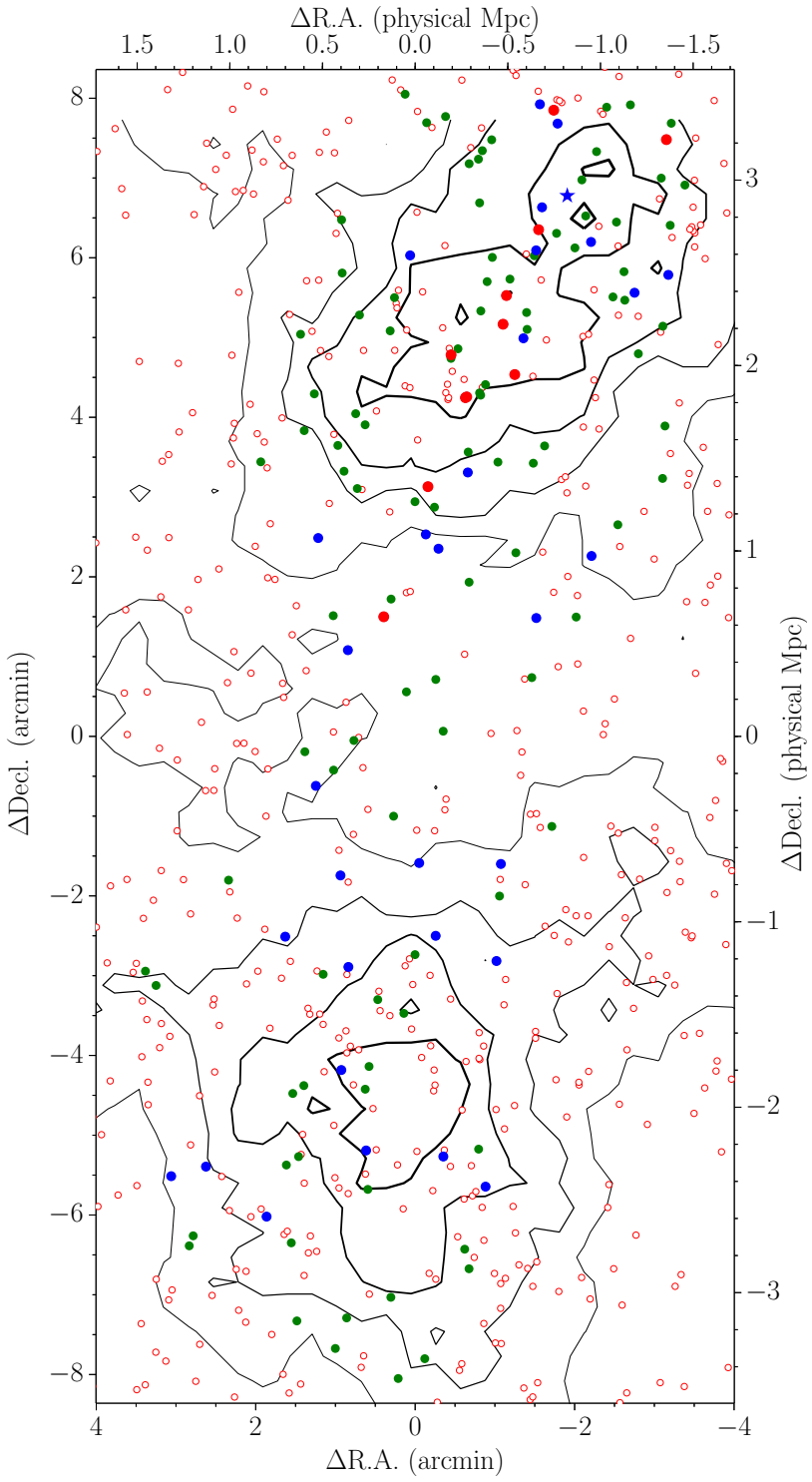

Fig. 32.— Sky distribution of g-dropout galaxies and number density contours in/around the D4-$g$drop region. Spectroscopically observed galaxies are marked by filled circles (red: proto-cluster members, blue: non-members, green: Lyα undetected galaxies), and spectroscopically unobserved galaxies are shown by open circles. The blue star indicates the position of the AGN. The origin (0,0) is (R.A., Decl.) = (22 : 16 : 56.3, −17 : 23 : 21.9), which is defined as the center of the figure. The lines show the number density contours of i-dropout galaxies from 4σ to 0σ with a step of 1σ.

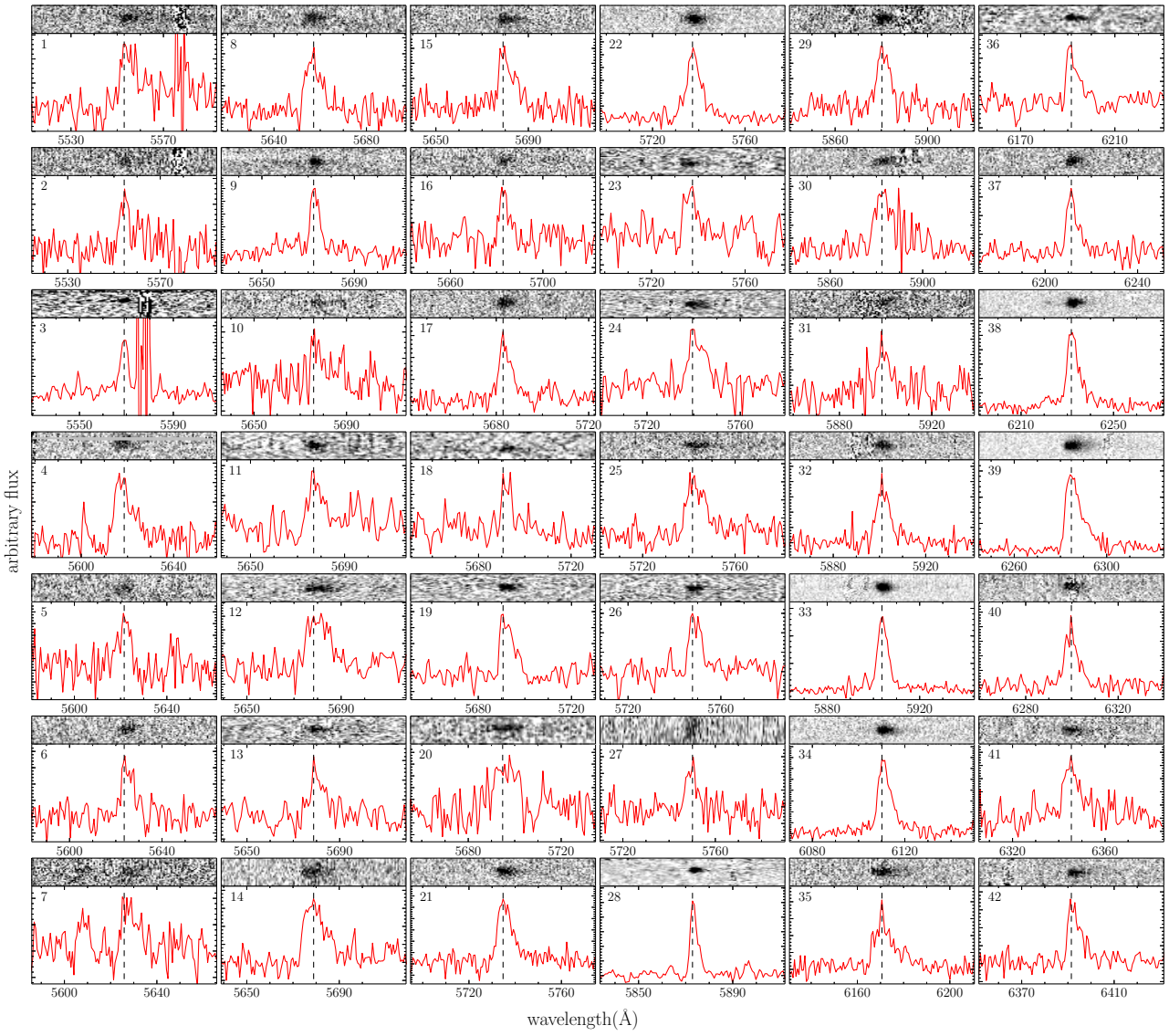

Fig. 33.— Spectra of 42 g-dropout galaxies having a Lyα emission line in/around the D4-$g$drop region. The object IDs are indicated at the upper left corner (Column 1 of Table 10).

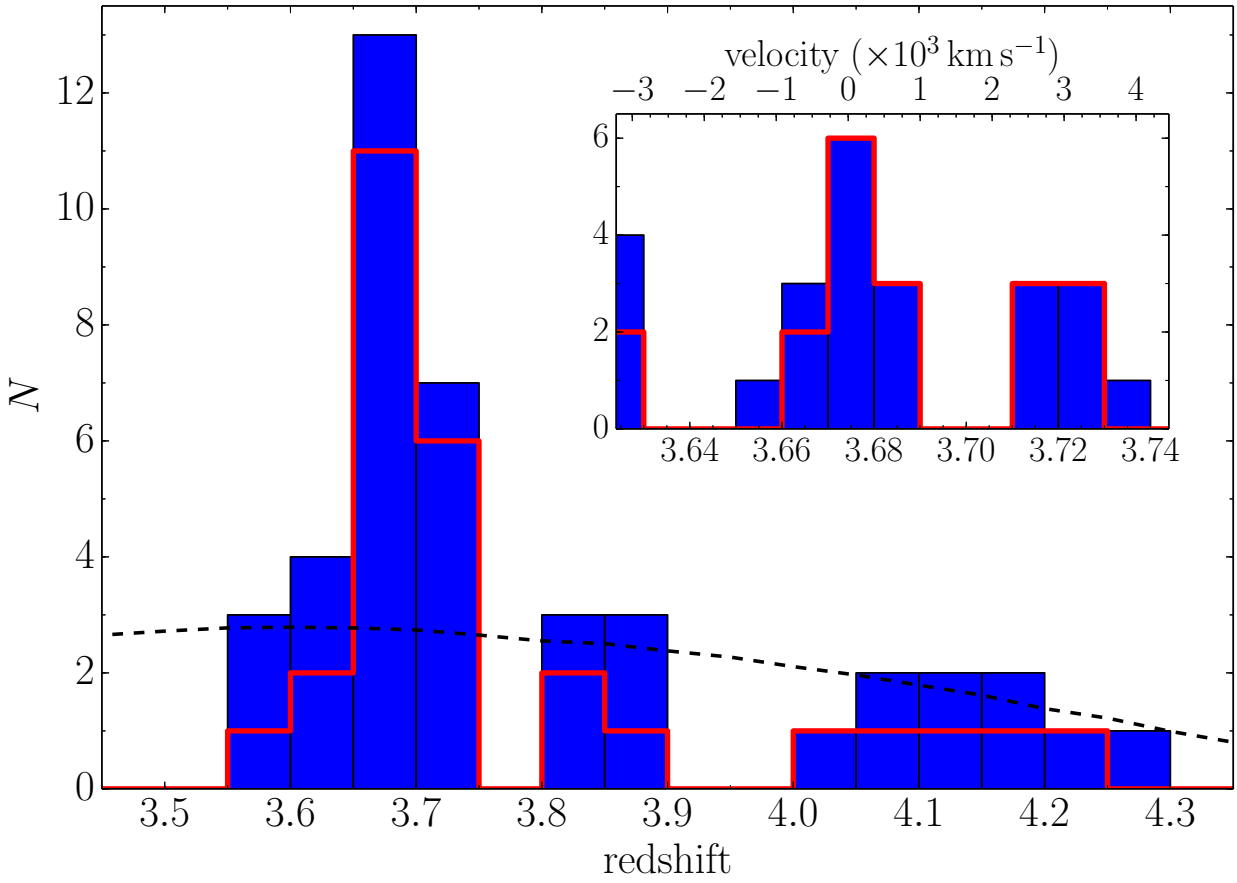

Fig. 34.— Redshift distribution of 42 g-dropout galaxies with the bin size of $\Delta z = 0.05$ in/around the D4-$g$drop region. Blue histogram shows all 42 galaxies, and red line shows galaxies only in the D4-$g$drop region. The inset is a close-up of the protocluster redshift range, with a bin size of $\Delta z = 0.01$.

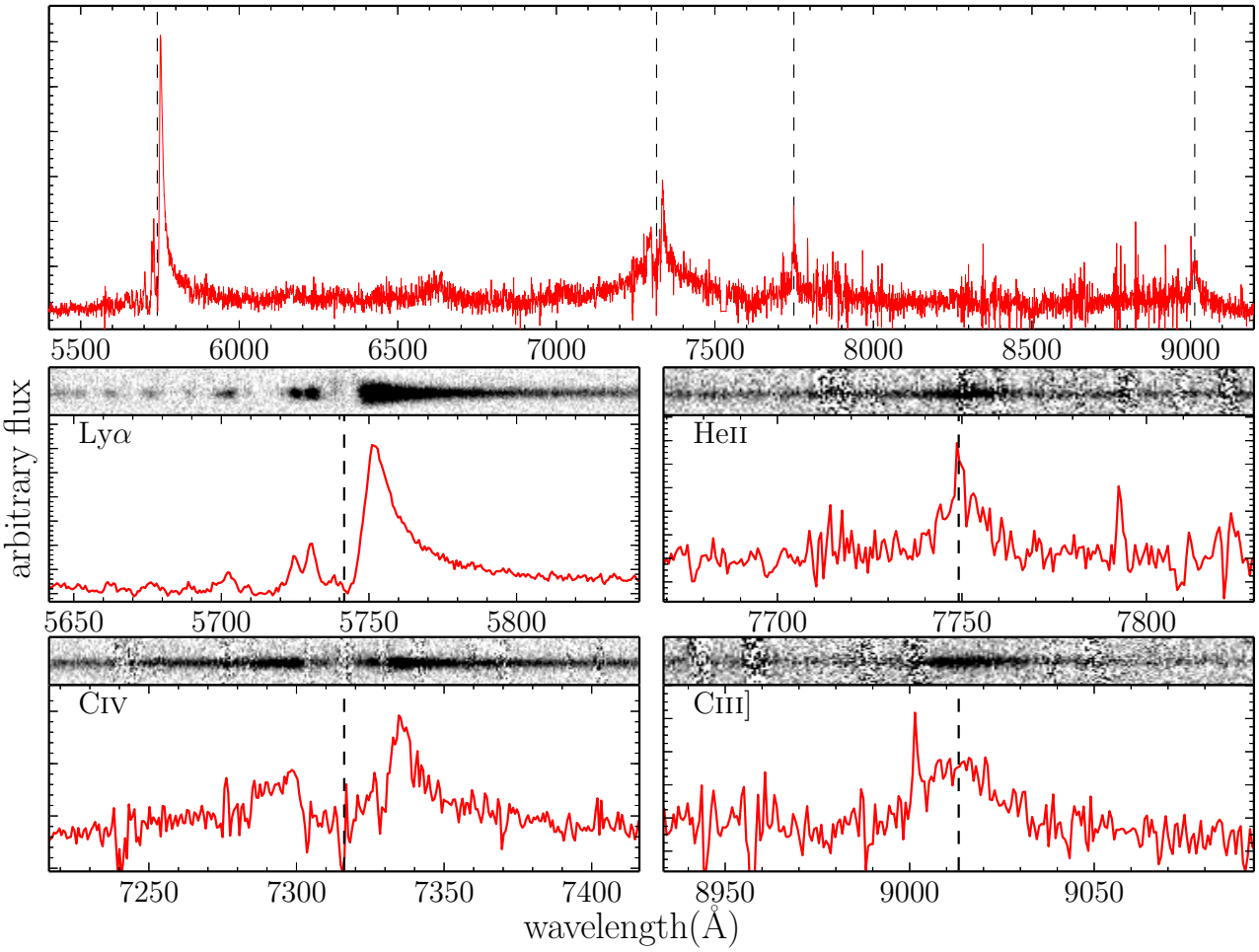

Fig. 35.— Spectra of the AGN in the D4-$g$drop. Upper panes shows the full wavelength coverage of the AGN, and lower four panels show emission lines which were clearly detected. The redshift was estimated by the peak wavelength of HeII and CIII], and the vertical dashed lines in the HeII and CIII] panels indicate the peak of the emission line. On the other hand, the vertical dashed lines in Lyα and CIV panels indicate the expected wavelength according to the redshift.

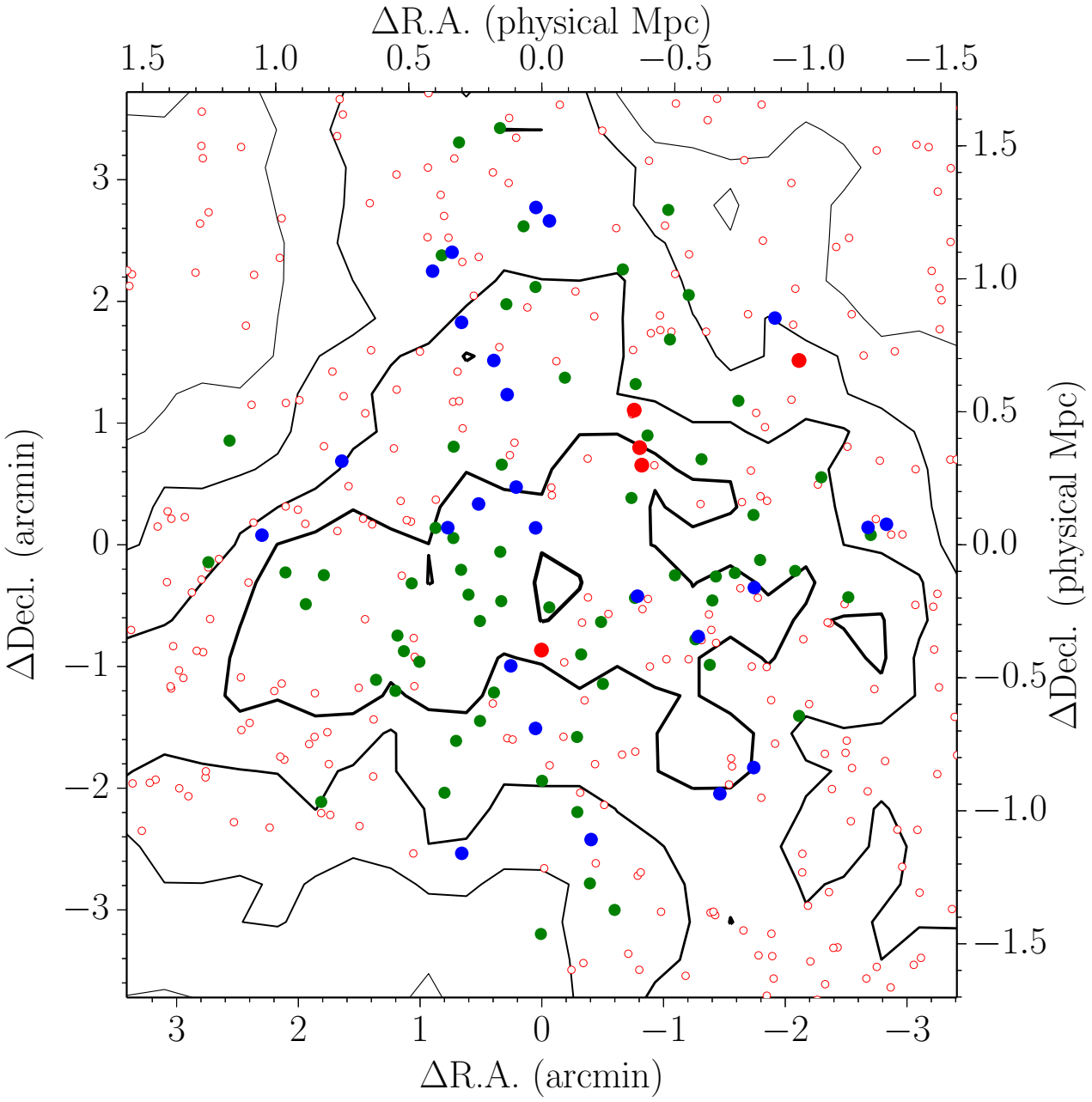

Fig. 36.— Sky distribution of u-dropout galaxies and number density contours in the D1-$u$drop region. Spectroscopically observed galaxies are marked by filled circles (red: protocluster members, blue: non-members, green: Lyα undetected galaxies), and spectroscopically unobserved galaxies are shown by open circles. The origin (0,0) is (R.A., Decl.) = (02 : 24 : 35.4, −04 : 19 : 40.3), which is defined as the center of the figure. The lines show the number density contours of i-dropout galaxies from 4σ to 0σ with a step of 1σ.

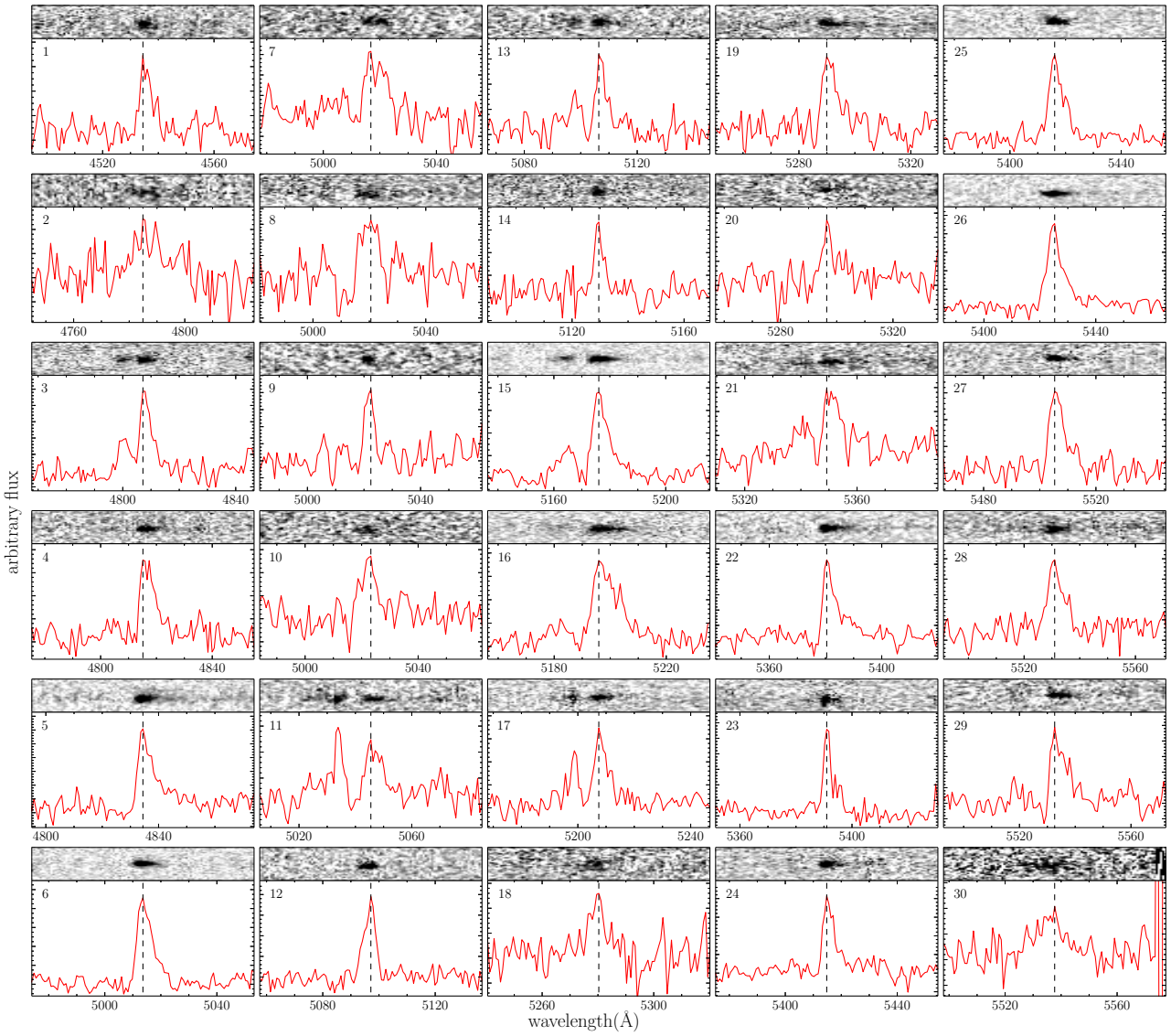

Fig. 37.— Spectra of 30 u-dropout galaxies having a Lyα emission line in the D1-$u$drop region. The object IDs are indicated at the upper left corner (Column 1 of Table 10).

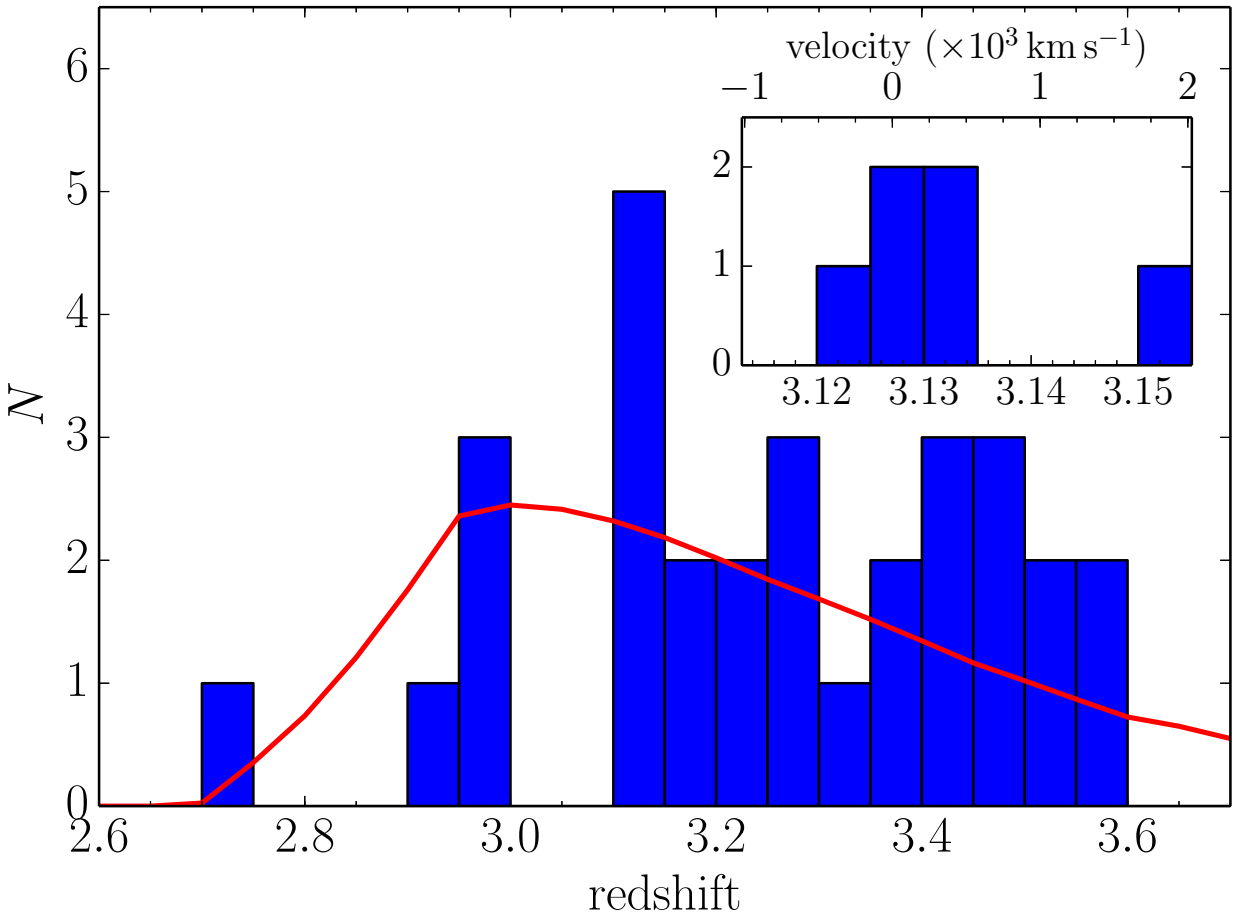

Fig. 38.— Redshift distribution of 30 u-dropout galaxies with the bin size of $\Delta z = 0.05$ in the D1-$u$drop region. The inset is a close-up of the protocluster redshift range, with a bin size of $\Delta z = 0.005$.

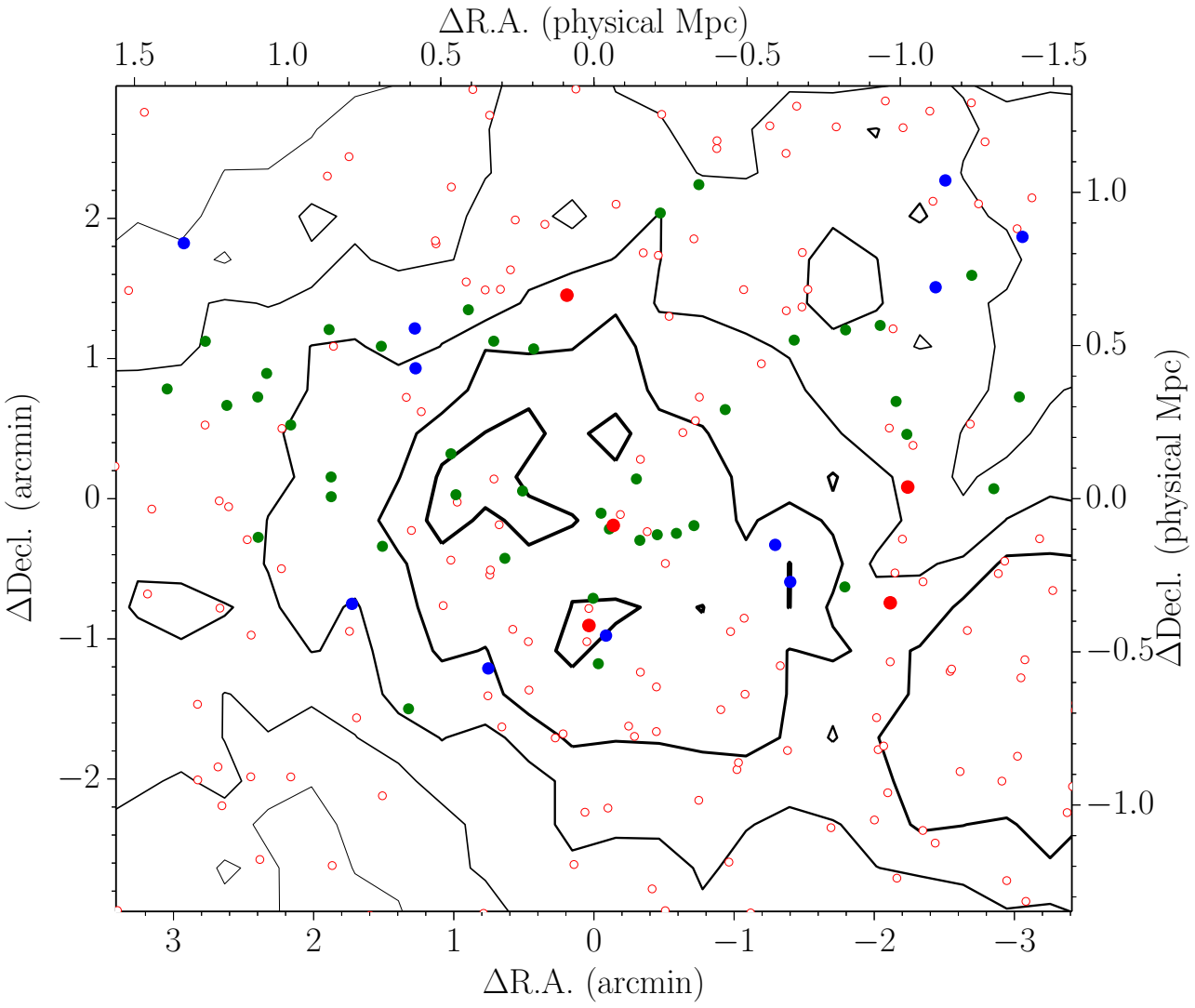

Fig. 39.— Sky distribution of u-dropout galaxies and number density contours in the D4-$u$drop region. Spectroscopically observed galaxies are marked by filled circles (red: protocluster members, blue: non-members, green: Lyα undetected galaxies), and spectroscopically unobserved galaxies are shown by open circles. The origin (0,0) is (R.A., Decl.) = (22 : 14 : 04.0, −17 : 59 : 11.3), which is defined as the center of the figure. The lines show the number density contours of i-dropout galaxies from 4σ to 0σ with a step of 1σ.

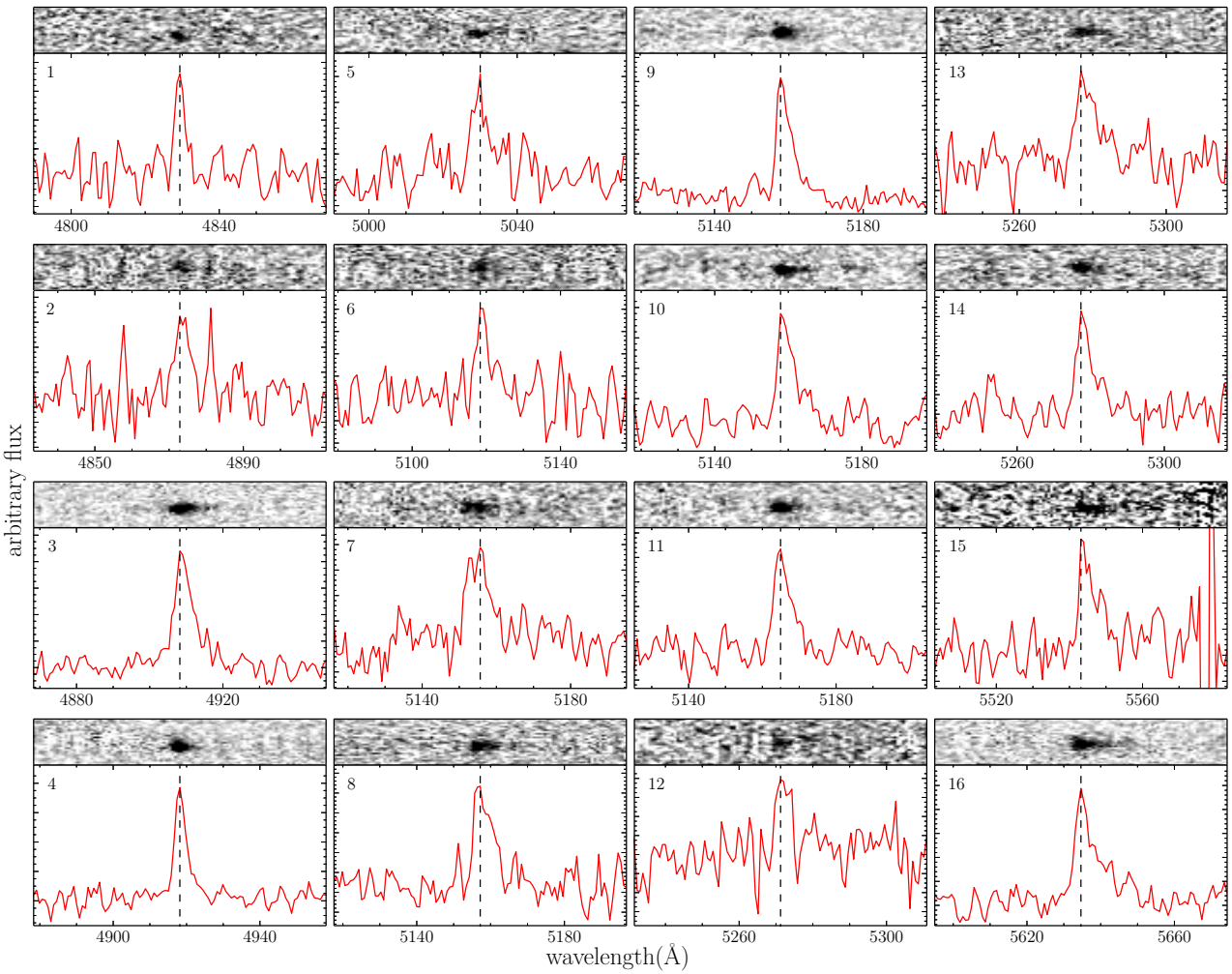

Fig. 40.— Spectra of 16 u-dropout galaxies having a Lyα emission line in the D4-$u$drop region. The object IDs are indicated at the upper left corner (Column 1 of Table 10).

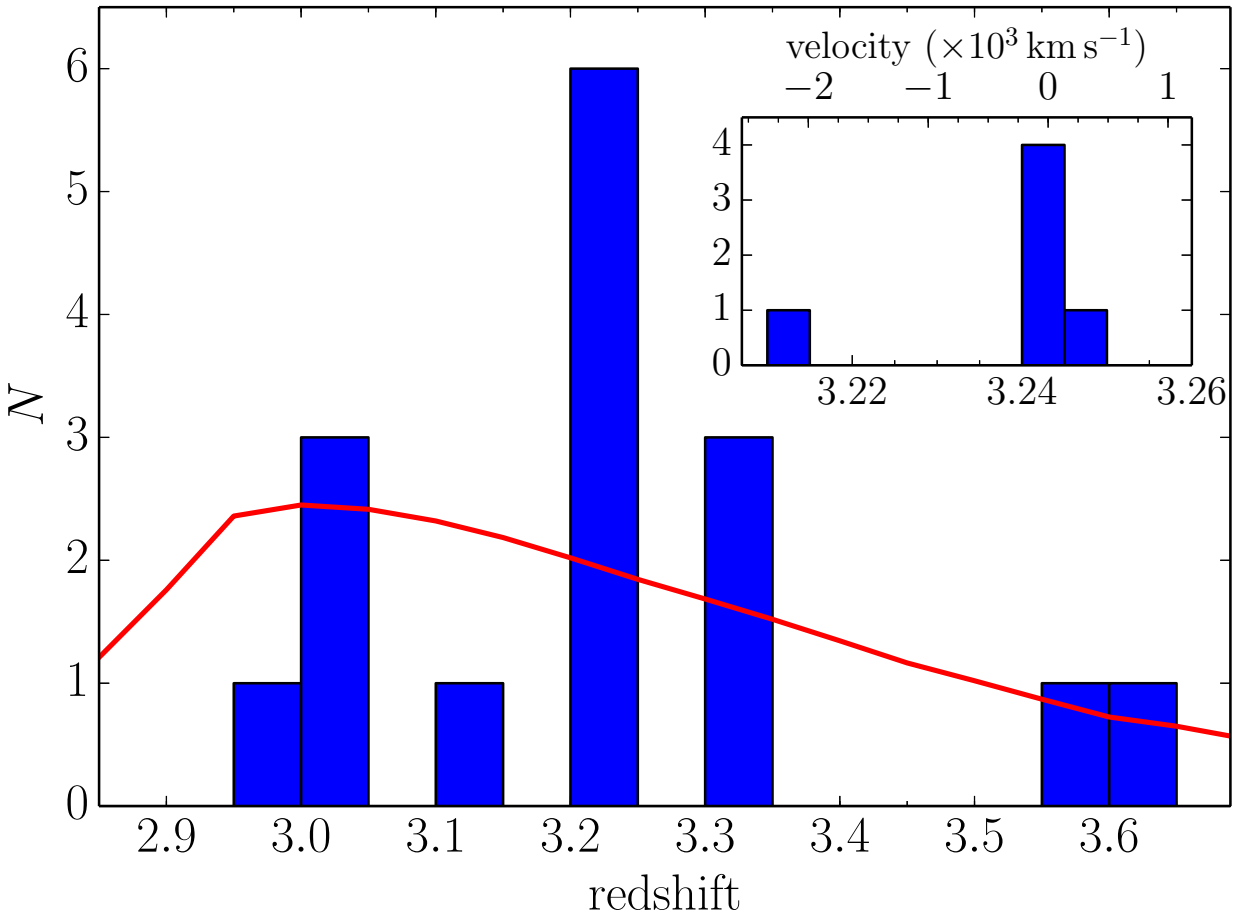

Fig. 41.— Redshift distribution of 16 u-dropout galaxies with the bin size of $\Delta z = 0.05$ in the D4-$u$drop region. The inset is a close-up of the protocluster redshift range, with a bin size of $\Delta z = 0.005$.

5. SED FITTING

5.1. Method

We analysed the stellar populations of the SDF-*i*drop protocluster galaxies by the standard spectral energy distribution (SED) fitting method based on the rest-frame UV-to-optical fluxes and redshifts (e.g., Papovich et al. 2001; Ono et al. 2010a). We generated various model SEDs, which are shifted to the spectroscopic redshift, in a similar way as in Section 2.3. The best-fit SED model was estimated so as to minimize the χ^2:

$$\chi^2 = \sum_i \frac{(f_{\mathrm{obs},i} - M_{\mathrm{star}} f_{\mathrm{model},i})^2}{\sigma_i^2}, \tag{1}$$

where $f_{\mathrm{obs},i}$ is the observed flux density in the i^{th} band, M_{star} is the stellar mass, $f_{\mathrm{model},i}$ is the mass-normalized model flux density in the i^{th} band, and σ_i is the sky noise of the i^{th} band. The $f_{\mathrm{model},i}$ depends on the assuming IMF, metallicity, star formation history, age, and dust extinction. The photometric data whose wavelength is shorter than Lyα are not used, since they are strongly attenuated by IGM. The flux density of undetected bands are replaced with as the 2σ upper limits. Only if the model flux is higher than the upper limit, a χ^2 is assessed with the equation (1).

We adopt Salpeter's IMF (Salpeter 1955) with lower and upper mass cut-offs of 0.1 and $100\mathrm{M}_\odot$. We fix the constant SFH, and metallicities to 0.02 and $0.2\mathrm{Z}_\odot$. The free parameters in the fitting routine are age, mass, and $E(B-V)$. Since GALAXEV code alone does not take into account possible contributions from emission lines, only the Lyα emission can be directly subtracted from the broad-band flux according to the Lyα flux measured by spectroscopy. As for nebular emission lines, we considered two extreme cases in the same way as Ono et al. (2010b): the one is without nebular emission where all ionizing photons escape from the galaxy, and the other is with nebular emission where all ionizing photons are converted into nebular emission. In the later case, we added these procedure to calculate the strength of each nebular emission under the assumption of electron temperature $T_e = 10^4\,\mathrm{K}$, electron density $n_e = 10^2\,\mathrm{cm}^{-3}$, and case B recombination. First, the number of ionizing photons produced per second, N_{Lyc}, is directly calculated from the SED generated from GALAXEV code. Then, Hβ line luminosity is estimated to be $L_{\mathrm{H}\beta} = 4.78 \times 10^{-13} N_{\mathrm{Lyc}}\,(\mathrm{erg\,s^{-1}})$ (Osterbrock & Ferland 2006). Based on the Hβ luminosity, the luminosities of other H recombination lines from Balmer, Paschen, and Brackett series and nebular lines from non-hydrogen are computed by the relative intensities given in Storey & Hummer (1995); Anders & Fritze-v. Alvensleben (2003). Nebular continuum emission is also estimated from N_{Lyc} (Krueger et al. 1995). Finally, the SED with nebular emission is generated by adding these three components: stellar continuum, nebular emissions, and nebular continuum. In the fitting procedure, we obtain M_{star}, the amplitude of a model SED, by $\partial\chi^2/\partial M_{\mathrm{star}} = 0$. The age was assumed between over 1 Myr and 1 Gyr with an interval of 0.05 dex, and $E(B-V)$ over 0 and 1.50 with an interval of 0.01. The errors in the best-fitting parameters are defined by 1σ confidence interval: $\Delta\chi_r^2 < 1$, where χ_r^2 is the reduced chi square.

5.2. Results

We investigated the stellar population only of the SDF-*i*drop protocluster members by SED-fitting analysis. Among the spectroscopic confirmed members in the SDF-*i*drop protocluster, we could detect only ID9 in both IRAC 3.6μm- and 4.5μm-bands (Figure 42). The other protocluster member galaxies could be detected with $\sim 2\sigma$ significance in both IRAC 3.6μm- and 4.5μm-bands by using stacked images. Thus, we investigated individual and average stellar population of one object of ID9 and protocluster members, respectively. They were detected in five bands of z'-, NB921-, NB973-, 3.6μm- and 4.5μm-bands, and the number of free parameters is three (mass, age, and dust); thus, the reduced chi square, χ^2_r is defined with $\chi^2/2$. The best-fitting parameters of two cases with and without nebular emission are summarized in Table 12, and the best-fitting SEDs are shown in Figure 43. Since both age and dust make similar behaviors on SEDs, both parameters are degenerate. The Balmer/4000Å break, which is good indicator for age, is not detected in our shallow NIR images, whose 2σ limiting magnitudes are indicated by arrows in Figure 43. Thus, it is difficult to separate the contribution of age from that of dust. Metallicity also works similar with age and dust; thus, the best-fitting age and dust can be significantly changed with the model about metallicity. On the other hand, the stellar mass is securely derived by the flux scaling and it is insensitive the shape of SEDs. Therefore, from fitting with five bands, the mass is relatively constrained, and both models about metallicities give similar masses of $\sim 1 \times 10^9\,\mathrm{M}_\odot$ for ID9 and $\sim 1.5 \times 10^8\,\mathrm{M}_\odot$ for stacked protocluster members in the case without nebular emission. The best-fitting $M_{\rm ster}$ in the case with nebular emission was found to be reduced by a factor of two or three compared with that in the case without nebular emission, since strong [O III] and Hα emissions can largely contribute to flux in 3.6μm- and 4.5μm-bands. Although ID9 is two or ten times more massive than the average $M_{\rm star}$ of protocluster members, some field LBGs (Eyles et al. 2007; Richard et al. 2011; McLure et al. 2011) and LAEs (Ono et al. 2010b) at the same redshift were also found to have similar stellar mass to that of ID9. Therefore, we could not find significant difference in $M_{\rm star}$ between protocluster and field galaxies. Further constraint on stellar population requires deep NIR images to measure the strength of Balmer/4000Å-break.

Table 12. SED fitting result of ID9 and stacked protocluster members

	Metallicity ($Z_\odot$)	χ^2_r	$M_{\rm star}$[a] ($M_\odot$)	Age (Myr)	$E(B-V)$ (mag)
			without nebular emission		
ID9	0.02	0.39	$1.3\,(0.3-2.9)\times10^9$	79.4	0.09
	0.2	0.44	$5.0\,(1.6-12.2)\times10^8$	4.5	0.24
stack	0.02	0.83	$2.0\,(0.8-10.3)\times10^8$	5.0	0.11
	0.2	0.86	$1.3\,(0.7-9.6)\times10^8$	15.8	0.01
			with nebular emission		
ID9	0.02	0.81	$3.2\,(1.0-10.9)\times10^8$	25.1	0.00
	0.2	1.54	$3.2\,(0.9-11.9)\times10^8$	25.1	0.00
stack	0.02	1.88	$1.6\,(0.5-10.4)\times10^8$	28.2	0.00
	0.2	4.63	$1.4\,(0.4-11.3)\times10^8$	25.1	0.00

[a]The 1σ uncertainty of $M_{\rm star}$ is indicated in parentheses.

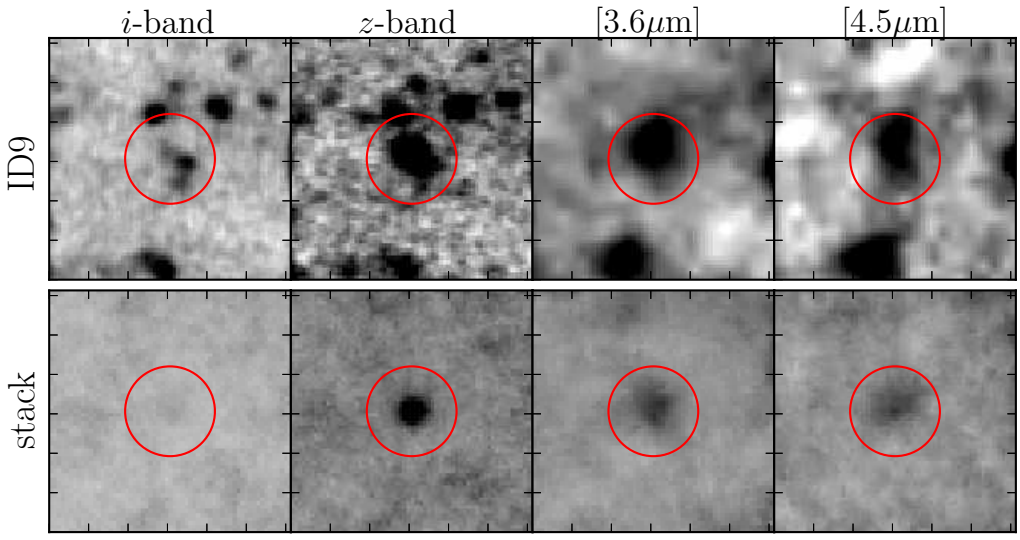

Fig. 42.— The thumbnail images ($\sim 6'' \times 6''$) of ID9 and stacked protocluster members.

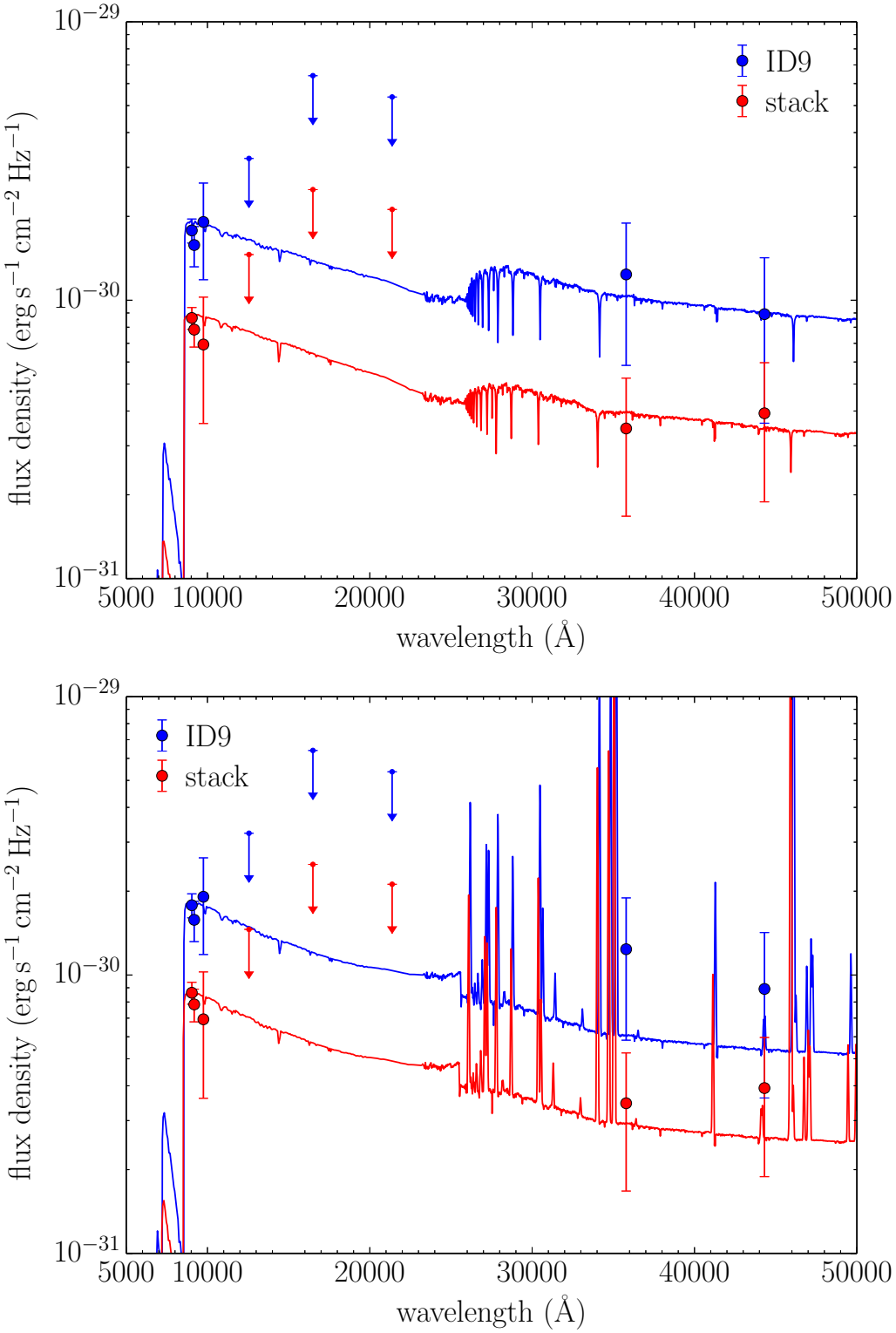

Fig. 43.— The best-fitting SED models without (upper) and with (lower) nebular emission to the photometric data points of ID9 (blue) and stacked protocluster members (red). The 2σ upper limits of non-detected bands are indicated by arrows.

6. DISCUSSIONS

6.1. Protocluster Search in Blank Fields

We demonstrate that wide-field imaging can be used to discover high-redshift protoclusters, even without possible probes of overdense regions. No regions where we are able to locate protoclusters include known RGs or QSOs within a radius of 10 arcmin and $\Delta z = \pm 0.1$ from the center of the protoclusters based on the NED database. Although RGs and QSOs may be effective probes to find protoclusters, our study shows several examples of high-redshift protoclusters without RGs or QSOs.

This study provides a valuable sample of protoclusters found in blank fields, which is interesting to be compared with the sample of protoclusters with RGs/QSOs to understand a possible relation between the activity of AGN and the environment. We found an AGN in the D4-$g$drop region; although far from the protocluster center (the redshift separation is $\Delta z = 0.05$ or $\Delta v = 3208\,\mathrm{km\,s^{-1}}$), this AGN may belong to a smaller galaxy group containing six galaxies (ID=21-26) at $z = 3.72$, as shown in Figure 34. If the protocluster will grow into an extremely massive cluster at $z = 0$, this small group is expected to be a part of a possible surrounding supercluster or might merge into a single halo. It has been reported that some protoclusters exhibit substructures, such as the merging of protoclusters. For example, Kuiper et al. (2012) found a protocluster around an RG at $z = 3.13$, as well as a nearby galaxy group, which had no RG. The difference in the redshift between these two structures was $\Delta z \sim 0.03$, which corresponds to $\Delta v \sim 1600\,\mathrm{km\,s^{-1}}$. Kuiper et al. (2011a) also found a protocluster at $z = 2.16$, which exhibited double-peaked velocity distribution, with a peak velocity separation of $\Delta v \sim 1600\,\mathrm{km\,s^{-1}}$. Furthermore, using narrow-band imaging, Hayashi et al. (2012) found that there were two or three clumps around a radio galaxy at $z = 2.53$. Although the velocity distribution and separation are unclear due to the lack of spectroscopic data, these clumps were spatially separated ~ 1.5 physical Mpc. Interestingly, the densest clump did not include a radio galaxy. Based on these results, AGNs are likely to preferentially reside in merging protoclusters, implying that galaxy mergers might trigger the activity of AGNs. It is expected that some properties of galaxies may be related to the dynamic state of their environment; however, it is difficult to make a strong arguments because the number of known protoclusters is small (especially those with large spectroscopic confirmation). While it is difficult to indicate any differences between protoclusters with and without RGs or QSOs, protocluster searches in blank fields are less biased than searches only around RGs or QSOs.

It should be noted that there would be selection bias even if we were to use wide-field imaging. We only used dropout samples to measure the overdensity; thus, our search is limited to protoclusters of star-forming galaxies. For this reason, mature protoclusters in which old and passive galaxies are dominant population, if present, would be missed in our sample selection. This bias is expected to be more serious at low redshifts because the protoclusters will have a varied population, and old and passive galaxies would be dominant toward mature clusters, as seen in the local universe. The VIMOS Ultra-Deep Survey (VUDS; Le Fevre et al. 2014) affords a good example of this possible bias. The VUDS is a spectroscopic redshift survey of ~ 10000 galaxies at $2 < z < 6$, covering three fields (i.e., COSMOS, ECDFS, and CFHTLS D1). In this survey, spectroscopic targets were mainly selected based on the photometric redshift, which enables us to select nearly the entire population of galaxies, including red and passive

galaxies, irrespective of the star-formation rate. Lemaux et al. (2014) discovered a protocluster at $z = 3.29$ in the CFHTLS D1 (which is the same survey field as this work). Interestingly, the protocluster region was identified as a 3σ overdense region of u-dropout galaxies at (ΔR.A., ΔDecl.)=(17, 8) arcmin, which is the second most overdense region in the CFHTLS D1. Lemaux et al. (2014) reported that the protocluster had a larger number of redder, brighter, and massive galaxies than the field. The 25 protocluster members, including nine tentative members, were spectroscopically confirmed, and 16 of them met our selection criteria of u-dropout galaxies. This example indicates that a protocluster, even that including more evolved galaxies than the field, can also be traced from the overdensity of star-forming galaxies, suggesting that the selection bias would not be severe, even at $z \sim 3$, although this is only one example.

6.2. Protocluster Structure

In this section, we discuss the structure of protoclusters using four confirmed protoclusters. We focus on the protoclusters of SDF-$i$drop and D4-$g$drop, which include more than ten members. With the other confirmed protoclusters of D1- and D4-$u$drop, there were too few spectroscopically confirmed members to discuss the internal structure.

6.2.1. $z = 6.01$ protocluster in the SDF

In the protocluster of SDF-$i$drop, the number of spectroscopically confirmed member galaxies is ten, and their velocity dispersion was found to be $906 \pm 188\,\mathrm{km\,s^{-1}}$. Venemans et al. (2007) found that the velocity dispersions of protoclusters at $z \sim 2-3$ and $4-5$ are $\sigma_r \sim 500-1000$ and $300\,\mathrm{km\,s^{-1}}$, respectively. The dark matter velocity dispersion is predicted to increase with cosmic time, based on a numerical simulation of cluster evolution (e.g., Eke et al. 1998). This is roughly consistent with observations at $z = 2-3$ and $4-5$, and is predicted to reach to $\sigma_r \sim 200\,\mathrm{km\,s^{-1}}$ at $z \sim 6$. Our estimate of the velocity dispersion at $z = 6.01$ is much larger than this, and the protocluster is expected to be far from virial equilibrium. This discrepancy could be due to the distinguishing three-dimensional structure of the protocluster. Figure 44 presents the 3D galaxy distribution in the protocluster; it reveals that the protocluster seems to consist of 4 subgroups of close pairs. Protocluster galaxies having almost the same redshifts happen to be located near to each other in the spatial dimension as well. As a result of substructure, the dynamical state of the protocluster as a whole is far from relaxation, and apparent velocity dispersion would be much larger than expected. To discuss this substructure more quantitatively, the histogram of the spatial separation from the nearest galaxy is shown in the left panel of Figure 45. The KS test suggests that the observed histogram is significantly different from a random distribution (the p-value is less than 0.01); random distribution was generated from a uniform distribution in the limited-size box of $17 \times 19 \times 29\,\mathrm{Mpc}^3$ in comoving scale, which corresponds to the volume occupied by the ten member galaxies. Furthermore, Figure 45 shows a histogram of the separation from the nearest neighbor of field LAEs. The data were taken from the spectroscopic LAE samples at $z = 5.7$ and 6.5 (Kashikawa et al. 2011), which have a high degree of spectroscopic completeness ($\sim 80-90\%$). To compare protocluster and field galaxies more accurately, the difference in average number density should

be corrected. The separation of field LAEs is multiplied by $(n_{\rm field}/n_{\rm protocluster})^{1/3} \sim 0.6$, where $n_{\rm protocluster}$ and $n_{\rm field}$ are the average number density of the protocluster and field, respectively. The p-value of a KS-test between the distribution of field LAEs and that of the protocluster was found to be less than 0.03, suggesting that the excess of close pairs cannot be attributed to the clustering nature of Lyα emitters alone.

We also evaluated the separations from the second nearest galaxies (the right panel of Figure 45) based on the same procedure as for the first nearest neighbors. Its separation distribution was found to be reproduced by the random distribution with the p-value of 0.23. Moreover, the separations from Nth nearest galaxies were also calculated, and shown in Figure 46. The separation, D, was fitted as a function of the Nth ($N > 2$) nearest galaxy: $\log(D) = a \times \log(N) + b$ (a and b are free parameters). The values of a and b were $a = 0.53 \pm 0.04$ and $b = 1.82 \pm 0.07$ (blue dashed line in Figure 46). The separation was found to be well approximated by this formula for $N > 2$, while the observed separation from the first nearest galaxies was found to be smaller with 1.8σ significance than the extrapolation from the formula. Even if we exclude two galaxies that have exceptionally small separations from the first nearest galaxy, the trend was confirmed with 1.8σ significance. Actually, as seen in Figure 46, all individual separations from the first nearest galaxy are smaller than the best fitted line. It is a statistically reliable result that galaxy separation from the first nearest galaxy is significantly smaller in this protocluster. Therefore, the protocluster galaxies tend to make galaxy pairs rather than triplets or larger structures. Similarly, close galaxy-pairs were also found in the possible protocluster candidates of D3-$i$drop and D1-$r$drop. Although the physical origin of the excess of galaxy pairs in protoclusters is unclear, galaxy formation could be affected to form pair-like structure in some way by high-density environments The typical separation length (> 100 kpc in physical scale) is too large for galaxy mergers or interactions. This is consistent with Cooke et al. (2010) who found that the fraction of Lyα emission in LBGs is larger in pairs with separation of only $\leqslant 70$ kpc in physical scale.

The inset in Figure 46 shows the same relations in the case of protoclusters at lower redshifts taken from the literature (Steidel et al. 1998; Venemans et al. 2007; Kuiper et al. 2012). Most of the protoclusters, whose members have been identified by Lyα emission, show the smooth relation without a bend at the first nearest neighbor. Interestingly, the protoclusters, SSA22 and MRC 0316-257, whose members are selected by the dropout technique, show a similar trend as our study: smaller separations from the first nearest galaxies than those from the second or higher nearest galaxies. Generally, LBGs have brighter UV luminosity than LAEs; thus, this trend would imply that bright galaxies are located at the core of a protocluster and make pair-like structures, while faint galaxies are more widely distributed. Bright galaxies, presumably more massive, would form structures faster than less massive galaxies. However, this comparison requires many caveats because the limiting magnitudes and spectroscopic completeness are different; in most lower-redshift protoclusters, only $40 - 60\,\%$ galaxies are spectroscopically observed. We only selected LBGs or LAEs in the above analysis, but various galaxy populations were found in $z \sim 2 - 3$ protoclusters. For example, Kuiper et al. (2011a, 2012) found large subgroups in protoclusters at $z \sim 2 - 3$, which contain Hα and [O III] emitters as well. These results would be naively consistent with the hierarchical structure formation model: at first, galaxies form small groups like galaxy pairs, and these small groups grow to larger structures through mergers. The cosmic epoch of $z \sim 6$ may be the onset of cluster formation.

6.2.2. $z = 3.67$ protocluster in the CFHTLS D4

We investigated the three-dimensional distribution of protocluster galaxies in the D4-$g$drop region, as shown in Figure 47. In contrast to the $z = 6.01$ protocluster in the SDF, the protocluster of D4-$g$drop appears to have a region where galaxies are strongly concentrated, as a cluster core, as opposed to being composed of several pairs. We applied the same analysis of separation from the Nth nearest protocluster members as with the SDF. The separation from the Nth nearest galaxies is shown in Figure 48, and is compared to that derived from a uniform random distribution in the same way with as the SDF. The figure clearly shows that the average separation from the Nth nearest galaxies of the D4-$g$drop protocluster was consistent with that of a uniform random distribution. Galaxies with a close neighbor in the protocluster core should have a small separation from second or higher nearest galaxies. Figure 49 shows a separation histogram from the first to sixth nearest galaxies of individual protocluster members, which clearly reveals that the galaxy distribution is far from random. The separation histograms in the case of fourth and fifth nearest galaxies can be divided into two groups of smaller and larger separation. Based on the KS-test, the observed distribution of the fifth nearest was significantly different from a random distribution ($p < 0.01$). In contrast, there were no significant differences in the distribution of sixth or higher nearest galaxies ($p \sim 0.4 - 0.8$). This result can be considered a result of a subgroup consisting of six galaxies (ID=11-16). These six galaxies are indicated by red circles in Figure 47, and are located near the center of the protocluster. There were several galaxies in the region surrounding the core, which will soon assemble at the core to form a rich cluster. We concluded that the D4-$g$drop protocluster has a core-like structure, which contrasts with many small subgroups seen in the SDF-$i$drop protocluster. This may be indicative of the virializing process over cosmic time, whereby protoclusters dynamically evolve to a concentrated structure from $z \sim 6$ to $z \sim 3$, although we have only one protocluster at each redshift.

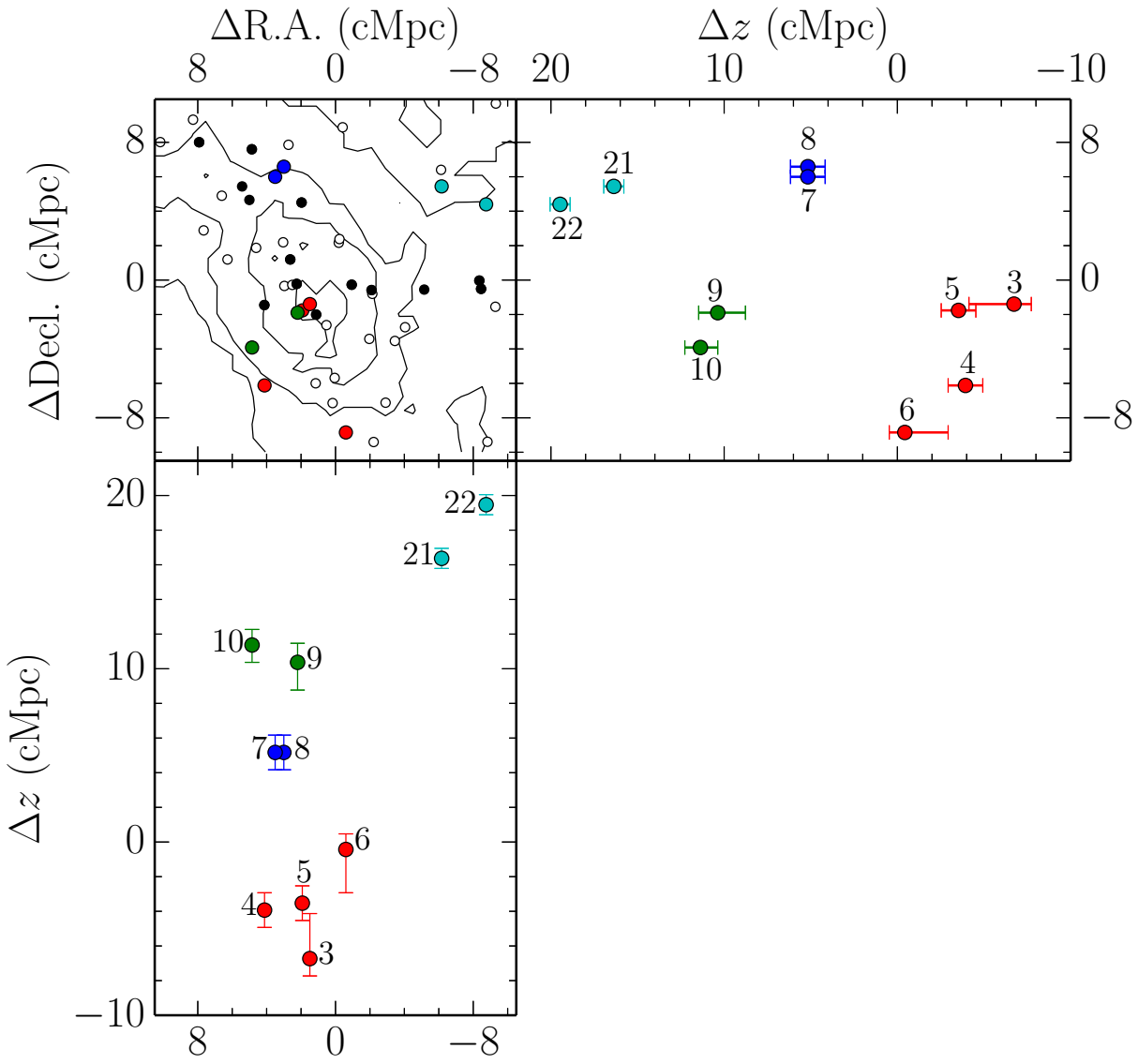

Fig. 44.— Three-dimensional distribution of the protocluster galaxies in the SDF-*i*drop region. The filled points represent the 28 Lyα detected galaxies, and the color-coded points indicate the protocluster galaxies. Possible substructures are grouped by the same color Note that the origin (0,0) of this figure is defined as (R.A., Decl.) = (13 : 24 : 22.4, +27 : 16 : 47.3).

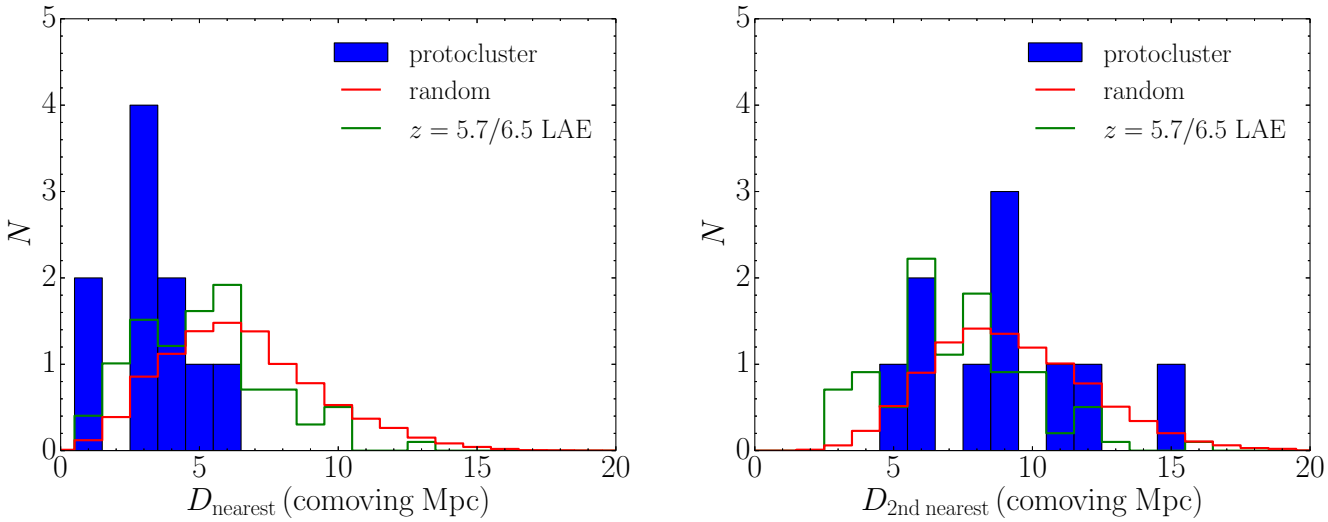

Fig. 45.— Distribution of the separation from the first (left) and second (right) nearest galaxy in the protocluster (blue histogram). The red line shows an expected distribution assuming that ten galaxies are randomly distributed in the protocluster region of $17 \times 19 \times 29\,{\rm Mpc}^3$, which was defined by the smallest box, including ten protocluster galaxies. This random realization was repeated 1,000 times. The green line shows the distribution of $z = 5.7$ and 6.5 LAEs in the SDF (Kashikawa et al. 2011). Separation of field LAEs is corrected for the difference in the average number density between the protocluster and field by multiplying $(n_{\rm field}/n_{\rm protocluster})^{1/3} \sim 0.6$.

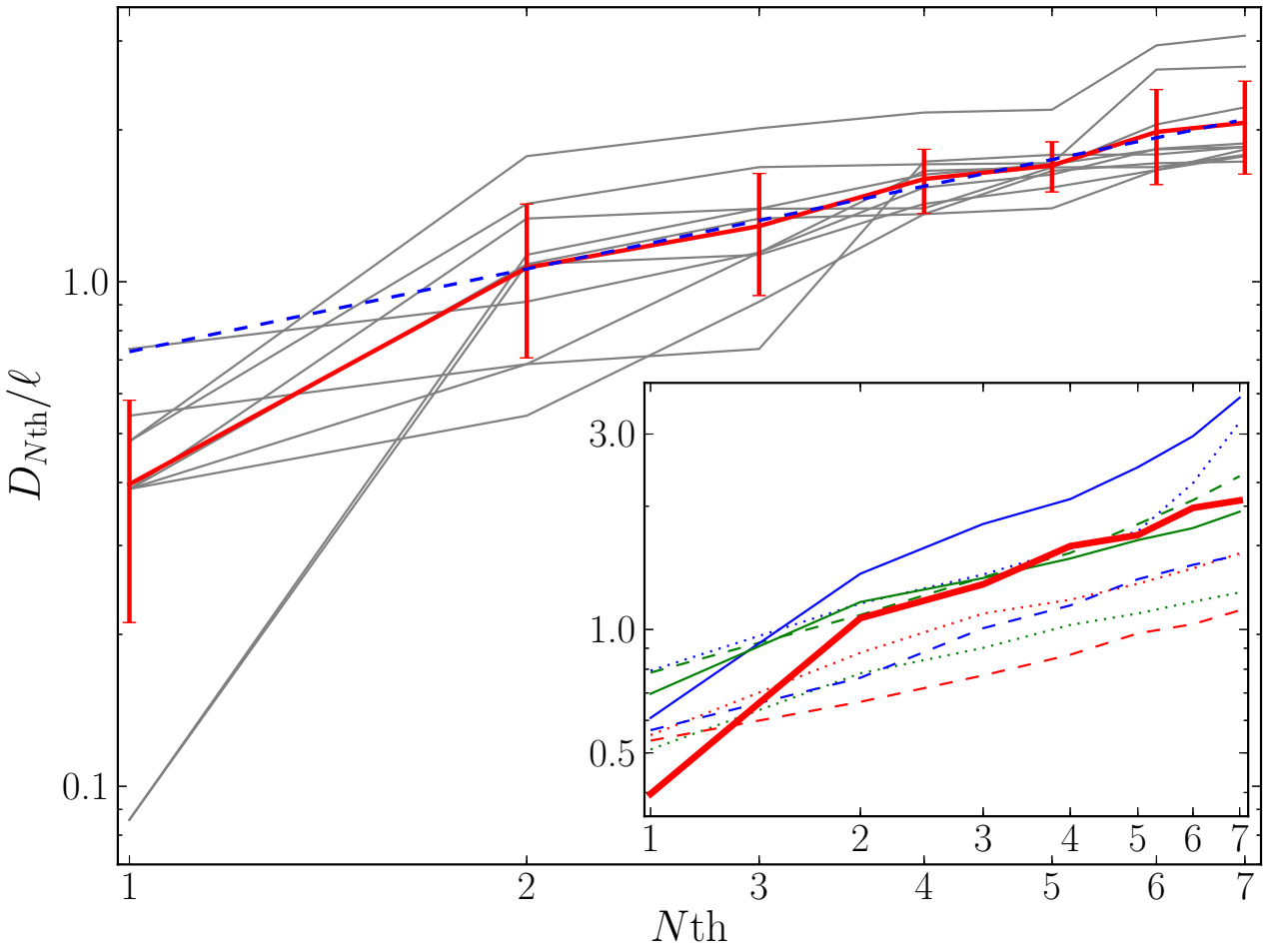

Fig. 46.— Galaxy separation from the first to seventh nearest galaxies. In the vertical axis, the galaxy separation is normalized by ℓ ($= n^{-1/3}$, where n is the number density). The red and gray lines represent the average and individual separations. The blue dashed line is the best fitted line to the separation from the second to seventh nearest galaxies. The inset shows the same relations in the case of protoclusters at lower redshifts. The solid lines shows the case for LBGs (red: SDF at $z = 6.0$ (this study), green: SSA22 at $z = 3.1$ (Steidel et al. 1998), blue: MRC 0316-257 at $z = 3.1$ (Kuiper et al. 2012)). The dashed and dotted lines show the case for LAEs (dashed red: TN J1338-1942 at $z = 4.1$, dashed green: TN J2009-3040 at $z = 3.2$ (Venemans et al. 2007), dashed blue: MRC 0316-257 at $z = 3.1$ (Venemans et al. 2005), dotted red: MRC 0943-242 at $z = 2.9$, dotted green: MRC 0052-241 at $z = 2.9$ (Venemans et al. 2007), dotted blue: MRC 1138-262 at $z = 2.2$ (Pentericci et al. 2000)).

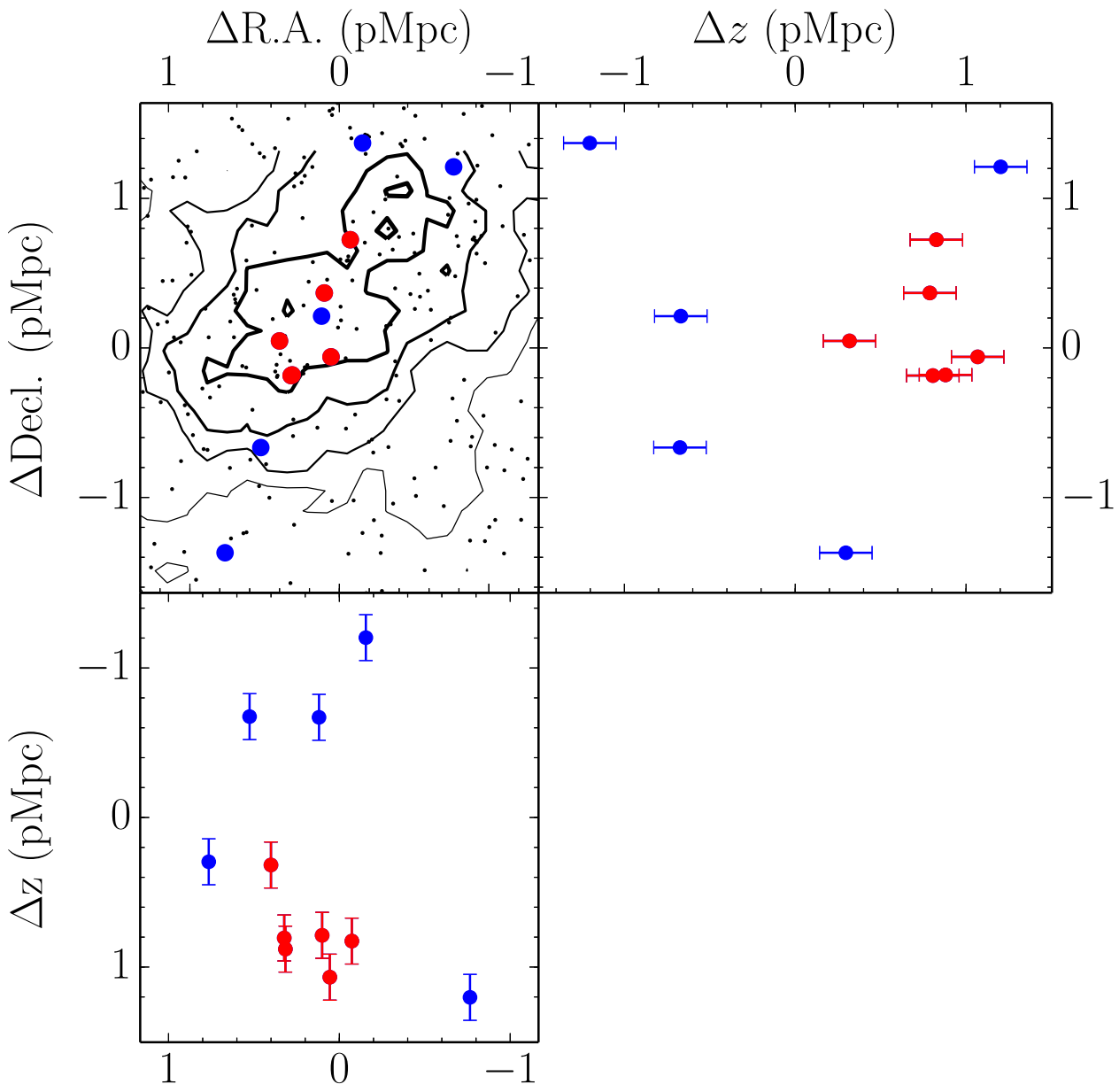

Fig. 47.— Three-dimensional distribution of the protocluster galaxies in the D4-$g$drop region. The filled circles represent the eleven protocluster galaxies (six red ones are galaxies residing in core region, and five blue in surrounding region), and the dots are g-dropout galaxies. Note that the origin (0,0) of this figure is defined as (R.A., Decl.) = (22 : 16 : 50.4, −17 : 18 : 41.6).

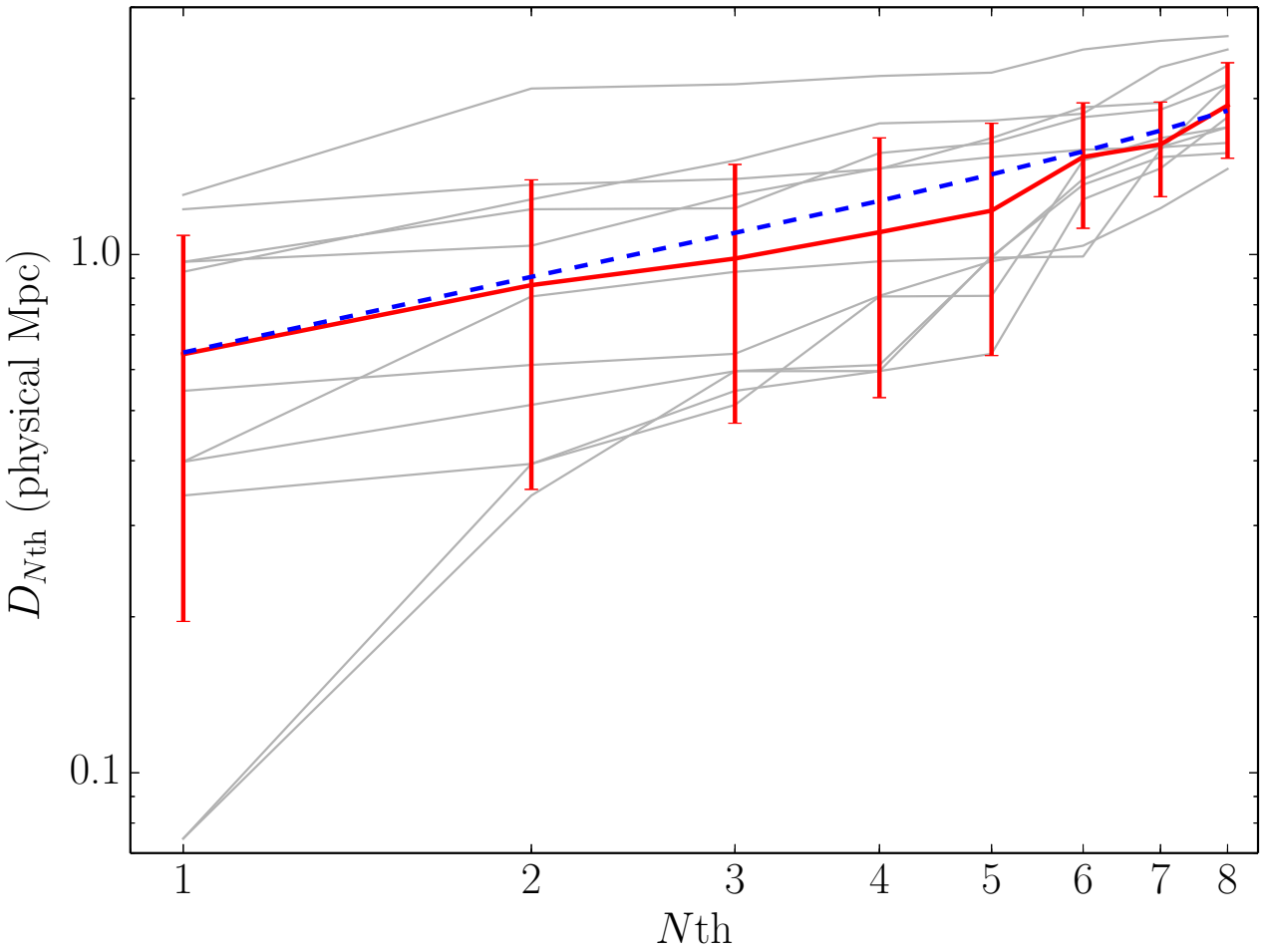

Fig. 48.— Galaxy separation from the first to eighth nearest galaxies of the D4-$g$drop protocluster. The red and gray lines represent the average and individual separations. The blue dashed line is the average separation derived by uniform random distribution.

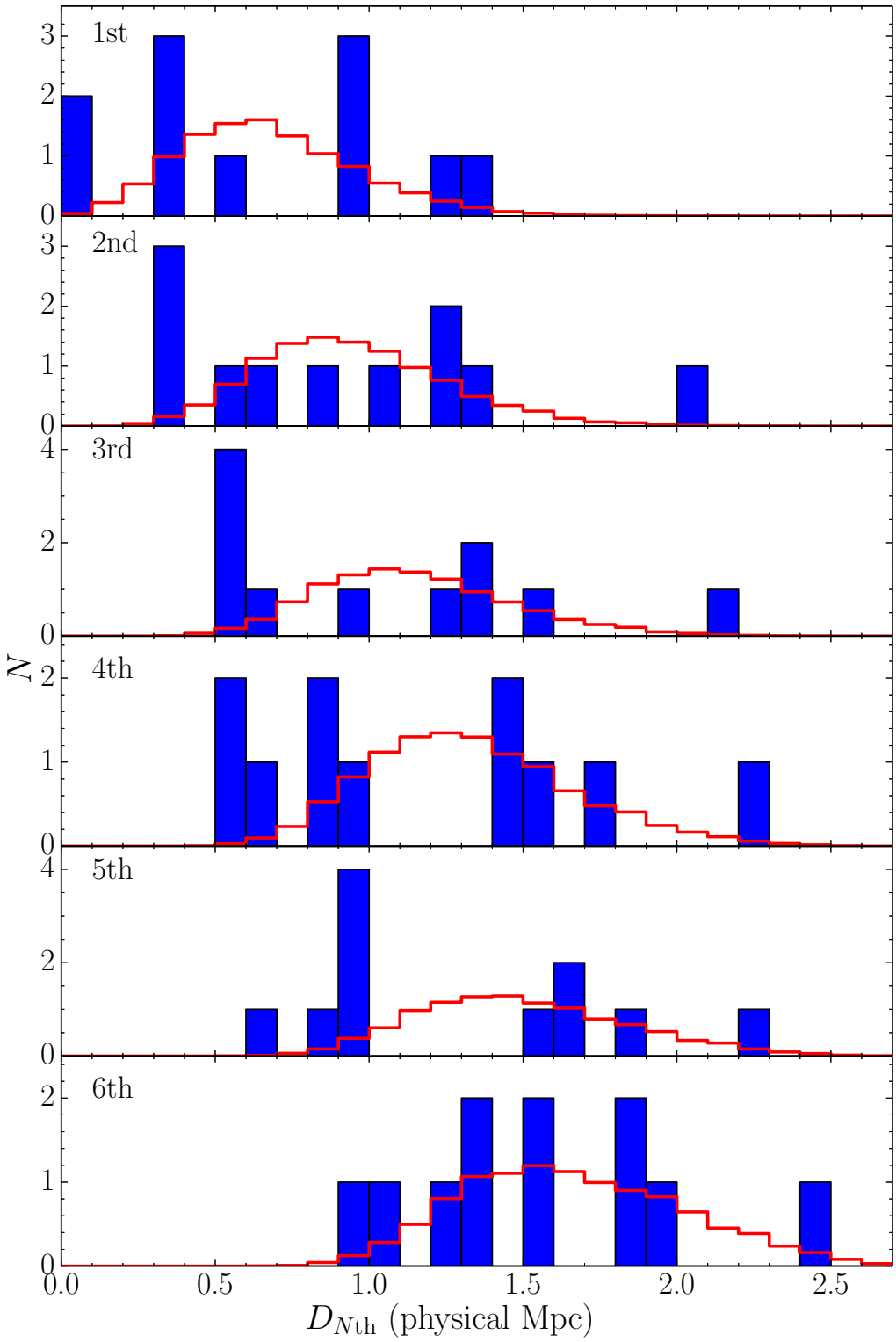

Fig. 49.— Distribution of the separation from the first (top) to sixth (bottom) nearest galaxy in the D4-$g$drop protocluster (blue histogram). The red line shows an expected distribution assuming that eleven galaxies are randomly distributed in the same volume of the D4-$g$drop protocluster.

6.3. Properties of Protocluster Members

6.3.1. $z = 6.01$ Protocluster in the SDF

We compared several galaxy properties between members and non-members to investigate whether there was any differences due to their environments at this early epoch. The average and standard deviation of $L_{\mathrm{Ly}\alpha}$, M_{UV}, and EW_{rest} in the protocluster and field galaxies were estimated, and found that all of these quantities of protocluster and field galaxies are consistent with each other within 1σ scatter, as shown in Table 13. Figure 50 shows that there are no significant differences between the M_{UV} and Lyα EW_{rest} distribution between protocluster and field (the p-value derived by the Kolmogorov-Smirnov (KS) test is > 0.3); however, a possible difference can be seen at the lowest EW_{rest} bin ($EW_{\mathrm{rest}} < 20\,\text{Å}$). Because both protocluster and field galaxies were observed in the same observing runs, it is unlikely that this difference was caused by a difference in the completeness limit of the spectroscopic observations. Taking into account the completeness limit, the sample in the lowest EW_{rest} bin mostly consists of the brightest galaxies in M_{UV}. This may imply that the brightest galaxies in the overdense region are older and have more dust, suppressing the Lyα emission compared with those in the field galaxies. Lee et al. (2013) also reported that the median EW_{rest} of $z = 3.78$ protocluster galaxies is higher than that of field galaxies. However, the Lyα emission, which is a resonantly-scattered line, can be affected by many physical parameters such as SFR, dust amount, and geometry of dust and neutral gas. It is therefore difficult to identify the reason of the possible difference at the lowest EW_{rest}. In this study of a $z = 6.01$ protocluster, it should be noted that the difference can be only seen in the lowest EW_{rest} bin, and there is no significant difference between the EW_{rest} distribution of the protocluster and the field galaxies as a whole.

We measured the Lyα fraction, which is the fraction of Lyα emitting galaxies among our dropout galaxies. This has been widely studied at $4 < z < 8$ (e.g., Stark et al. 2010; Schenker et al. 2012; Treu et al. 2013), and the fraction steadily increases toward higher redshift, while it gradually decreases beyond $z = 6$, possibly as a signature of reionization. However, those measurements were made using only field galaxies. It is important to compare the Lyα fraction between field galaxies and galaxies in overdense regions in order to ascertain whether it has environmental dependence or not. Since it is impossible to distinguish between member and non-member galaxies in the spectroscopically undetected galaxies, we measured the Lyα fraction in the projected overdense region over $8 \times 8\,\mathrm{arcmin}^2$, including Ly$\alpha$ emitting galaxies, even if they were found in the field behind and in front of the protocluster. We assumed that the Lyα undetected galaxies are all at $z = 6.0$, and calculated their M_{UV}. In this estimate, expected IGM absorption at $z = 6.0$ in the z'-band was also corrected for though the correction is as small as 0.08 mag. We here apply the same color selection criterion of $i' - z' > 1.3$ as in Stark et al. (2011). Our spectroscopic completeness still remains high ($> 95\%$) in the overdense region because i'-dropout galaxies with $1.3 < i' - z' < 1.5$ were also observed as secondary targets. We compare our result with the bright sample of Stark et al. (2011), which has the same M_{UV} range as ours. The fraction in the overdense region was found to be $0.0^{+6.4}_{-0.0}\%$ and $20.0 \pm 11.0\%$ for $EW_{\mathrm{rest}} > 50\,\text{Å}$ and $> 25\,\text{Å}$, which are almost the same as in the field at $z \sim 6$.

In addition to M_{star} investigated in Section 5.2, these results show that we do not find any significant differences in the observed properties between protocluster and field galaxies. This would indicate that this protocluster is still in the early phase of cluster formation, before

any environmental effect works on galaxy properties. However, the observed properties of protocluster galaxies in this study are very limited. According to other works for lower-redshift protoclusters, differences in galaxy properties between protocluster and field galaxies begin to appear at $z \sim 2-3$: protocluster galaxies are $\sim 2-3$ times more massive than field galaxies at the same redshift (Steidel et al. 2005; Kuiper et al. 2010; Hatch et al. 2011b). In this study, the UV and Lyα properties of the protocluster galaxies are almost the same as those of field galaxies. These properties are closely related to star-formation activity. Therefore, the stellar-mass difference as seen at $z = 2-3$ could emerge in a later cluster formation phase rather than in this early stage. Overdense regions would result in a higher rate of galaxy mergers, which could ignite intense star forming. Furthermore, it would be expected that a large amount of gas, which is ingredient to sustain star-formation activity for a long time, is stored in the gravitational potential well of protoclusters. In order to find which is a major factor in generating stellar-mass difference as seen in $z \sim 2-3$ protoclusters, short intense or long steady star-formation, it is required to directly observe star-formation activity in lower-redshift protoclusters.

6.3.2. $z = 3.67$ Protocluster in the CFHTLS D4

The average properties of eleven galaxies in the D4-$g$drop protocluster are listed in Table 14. The number of field g-dropout galaxies found in the D1- and D4-$g$drop regions is 67. The average properties of these field galaxies are also listed in Table 14. Furthermore, as mentioned in Section 6.2.2, the protocluster has a core-like structure, and the eleven galaxies can be divided into two groups: six galaxies of the core and five galaxies of the outskirt; the average properties of these galaxies are also listed in Table 14. The relation between $M_{\rm UV}$ and $EW_{\rm rest}$ for both protocluster members and field galaxies is shown in Figure 52. A difference in the properties of protocluster and field galaxies was clearly found: protocluster galaxies have smaller $EW_{\rm rest}$ and $L_{{\rm Ly}\alpha}$ than field galaxies (KS p-value is < 0.05); however, no difference was found at $z \sim 6$, as shown in Figure 50.

A simple mechanism that can affect the $EW_{\rm rest}$ of the Lyα emission is dust, which traps Lyα photons. If dust were a major reason for the small $EW_{\rm rest}$, we would also expect differences to appear in the $M_{\rm UV}$. However, we could not find any systematic differences in $M_{\rm UV}$ between the protocluster and field galaxies (see Table 14). Furthermore, we compared the UV slope, which is an indicator of dust attenuation, between protocluster and field galaxies. The UV slope of the g-dropout galaxy is determined from the $i-z$ color. Since the i-band, which is a detection band, image was significantly deeper than z-band image, some g-dropout galaxies were not detected in z-band. We only used g-dropout galaxies, where the z-band magnitude was greater than the 2σ limiting magnitude for the estimate of the UV slope. The numbers of g-dropout galaxies used in the estimate of the UV slope was 50 for the field and nine for the protocluster. Differences in the limiting magnitude between i- and z-band can lead to bias in the UV slope; however, the comparison was performed using the same criteria from the same dataset, and any bias would lead to the same effect on the estimate of the UV slope. The UV slope was calculated from

$$\beta = -\frac{1}{2.5} \times \frac{m_i - m_z}{\log_{10} \lambda_{{\rm eff},i} - \log_{10} \lambda_{{\rm eff},z}} - 2.0,$$

where $\lambda_{\rm eff}$ is the effective wavelength. The average β of the protocluster galaxies was $\beta =$

-1.88 ± 1.15, and that of the field galaxies was $\beta = -1.92 \pm 1.21$. There were no significant differences between the UV slopes of the protocluster and field galaxies. Therefore, the difference between $EW_{\rm rest}$ of the protocluster and field galaxies cannot be attributed only to dust. Since Lyα photons are resonantly scattered by neutral hydrogen, the Lyα radiation generally travels farther before escaping from a galaxy than does UV radiation. Although both $EW_{\rm rest}$ and $M_{\rm UV}$ are affected by dust, it should be noted that $M_{\rm UV}$ will be less strongly affected by dust than the Lyα emission.

Neutral hydrogen gas within a protocluster is another possible reason for the small $EW_{\rm rest}$. Cucciati et al. (2014) found a large amount of neutral hydrogen gas in the intracluster space of a protocluster by examining spectra that showed absorption of background galaxies behind a protocluster at $z = 2.9$ with the same redshift as the protocluster. The total gas mass of neutral hydrogen should be a few $10^{12} - 10^{13}\,{\rm M}_{\odot}$. As described in Section 6.2, Kuiper et al. (2012) found two subgroups with a velocity separation of $1600\,{\rm km\,s^{-1}}$ in a $z = 3.13$ protocluster: one that included an RG, and one that did not. The average Lyα $EW_{\rm rest}$ of member galaxies in the subgroup without an RG was $-13.3 \pm 5.3\,$Å, which is significantly smaller than that of field ($7.4 \pm 2.1\,$Å) at the same redshift, whereas the subgroup with an RG had a larger $EW_{\rm rest}$ ($26.4 \pm 3.8\,$Å). If the protocluster had a large quantity of intracluster hydrogen gas, we would expect a smaller $EW_{\rm rest}$ in the subgroup without the RG; on the other hand, a larger $EW_{\rm rest}$ would be expected in the subgroup with the RG if the radiation from the RG were strong enough to ionize the neutral hydrogen gas. If this were the case for our D4-$g$drop protocluster, a small Lyα $EW_{\rm rest}$ could be explained as a result of systematic attenuation due to the intracluster neutral hydrogen gas. Suppose that a nearly mature protocluster, such as the D4-$g$drop protocluster, had already accumulated significant cold intracluster gas at $z = 3.67$; the intracluster gas would come either from the outside of the protocluster drawn by the strong gravitational potential of the protocluster, or from the evolved member galaxies themselves through the galactic outflow. However, Kuiper et al. (2012) reported that differences in $EW_{\rm rest}$ can be attributed to dust rather than intracluster neutral hydrogen gas, because the UV slopes of subgroups with and without an RG were systematically different. A small Lyα $EW_{\rm rest}$ in protocluster could be explained by intracluster gas; however, further study is required to obtain conclusive evidence.

Interestingly, clear contrast in the internal structure was also found between the SDF-$i$drop protocluster at $z = 6.01$ and the D4-$g$drop protocluster at $z = 3.67$, as discussed in Section 6.2. The properties of protocluster galaxies might be affected by their environment, in combination with dramatic changes in the internal structure. Galaxies in more mature protoclusters may be more evolved and contain more dust, and are expected to store more gas in the surrounding environment. Further observations to increase the number of the protocluster sample galaxies would help us to draw firmer conclusions. If our finding of small Lyα $EW_{\rm rest}$ in overdense region was a general feature (at least at $z = 3.67$), this would impact the measurement of the Lyα fraction, which is an effective method to probe reionization at high redshifts. The measurements were mostly made using only field galaxies; however, our results suggest that there may be dependence on the environment.

6.3.3. $z \sim 3$ Protocluster in the CFHTLS D1 and D4

We found two $z \sim 3$ protoclusters in the CFHTLS D1 and D4. Although it is difficult to analyze the internal structure due to the small number of confirmed protocluster galaxies, here we investigate galaxy properties. Table 15 lists the average properties of each of the protocluster and field galaxies, and Figure 52 shows the distribution of $M_{\rm UV}$ and $EW_{\rm rest}$. We did not find a significant difference in the $M_{\rm UV}$–$EW_{\rm rest}$ relation between the protocluster and field galaxies in the D4-$u$drop protocluster, while the D1-$u$drop protocluster members tended to have a slightly lower $EW_{\rm rest}$ than the field galaxies. Although these were at the same redshift ($z = 3.13$ and 3.24), there was the difference of $L_{{\rm Ly}\alpha}$ over 1σ uncertainty between the D1-$u$drop and D4-$u$drop protocluster galaxies. The velocity dispersions of these protoclusters are significantly different, although the uncertainty was large due to the small number of confirmed protocluster members. The D1-$u$drop protocluster, which had a larger velocity dispersion, also had lower $L_{{\rm Ly}\alpha}$ than the D4-$u$drop protocluster. If the velocity dispersion (which corresponds to the dynamical mass under virial equilibrium) was a good indicator of the maturity of the protoclusters, the results would appear consistent with what we found in the D4-$g$drop protocluster (i.e., Lyα emission would be suppressed to a greater degree in more mature protoclusters). As we have shown in the previous subsection, differences in Lyα $EW_{\rm rest}$ can be attributed either to dust in the protocluster galaxies, or the intracluster neutral hydrogen gas. It is difficult to determine which is the most significant factor based on current data; however, we checked only the UV slope to the spectroscopically confirmed u-dropout galaxies. As shown in Figure 53, we were not able to find any significant differences in the UV slope among D1- and D4-$u$drop protocluster galaxies and field galaxies. Our sample size was too small to determine a clear systematic trend, but we should consider that a variety of properties of protoclusters, even at the same redshift. Further systematic surveys are required for a deeper discussion of cluster formation and evolution.

Table 13. Average of observed properties of i-dropout galaxies in the SDF

	$L_{{\rm Ly}\alpha}$ ($10^{42}\,{\rm erg\,s^{-1}}$)	$M_{\rm UV}$ (mag)	$EW_{\rm rest}$ (Å)
protocluster	5.51 ± 3.78	-20.16 ± 0.49	50.74 ± 31.66
field	4.21 ± 2.44	-20.34 ± 0.61	45.53 ± 52.60
p-value[a]	0.78	0.78	0.32

[a]Using the KS test, the distribution of observed properties are compared between protocluster and field galaxies.

Table 14. Average of observed properties of g-dropout galaxies in the CFHTLS Deep Fields.

	$L_{\mathrm{Ly}\alpha}$ ($10^{42}\,\mathrm{erg\,s^{-1}}$)	M_{UV} (mag)	EW_{rest} (Å)
protocluster	1.46 ± 0.76	-19.47 ± 0.51	24.48 ± 12.20
core	1.69 ± 0.75	-19.84 ± 0.60	22.45 ± 10.03
surrounding	1.20 ± 0.68	-19.29 ± 0.26	27.13 ± 14.60
field	2.34 ± 1.67	-19.45 ± 0.74	41.68 ± 39.00
p-value[a]	0.04	0.67	0.03

[a]Using the KS test, the distribution of observed properties are compared between protocluster and field galaxies.

Table 15. Average of observed properties of u-dropout galaxies in the CFHTLS Deep Fields.

	$L_{\mathrm{Ly}\alpha}$ ($10^{42}\,\mathrm{erg\,s^{-1}}$)	M_{UV} (mag)	EW_{rest} (Å)
D1 protocluster	0.98 ± 0.27	-19.19 ± 0.84	31.49 ± 25.29
D4 protocluster	2.05 ± 0.58	-19.27 ± 0.47	34.34 ± 24.03
field	1.89 ± 1.29	-19.26 ± 0.68	37.70 ± 22.80
p-value (D1 and field)	0.28	0.98	0.64
p-value (D4 and field)	0.82	0.90	0.99

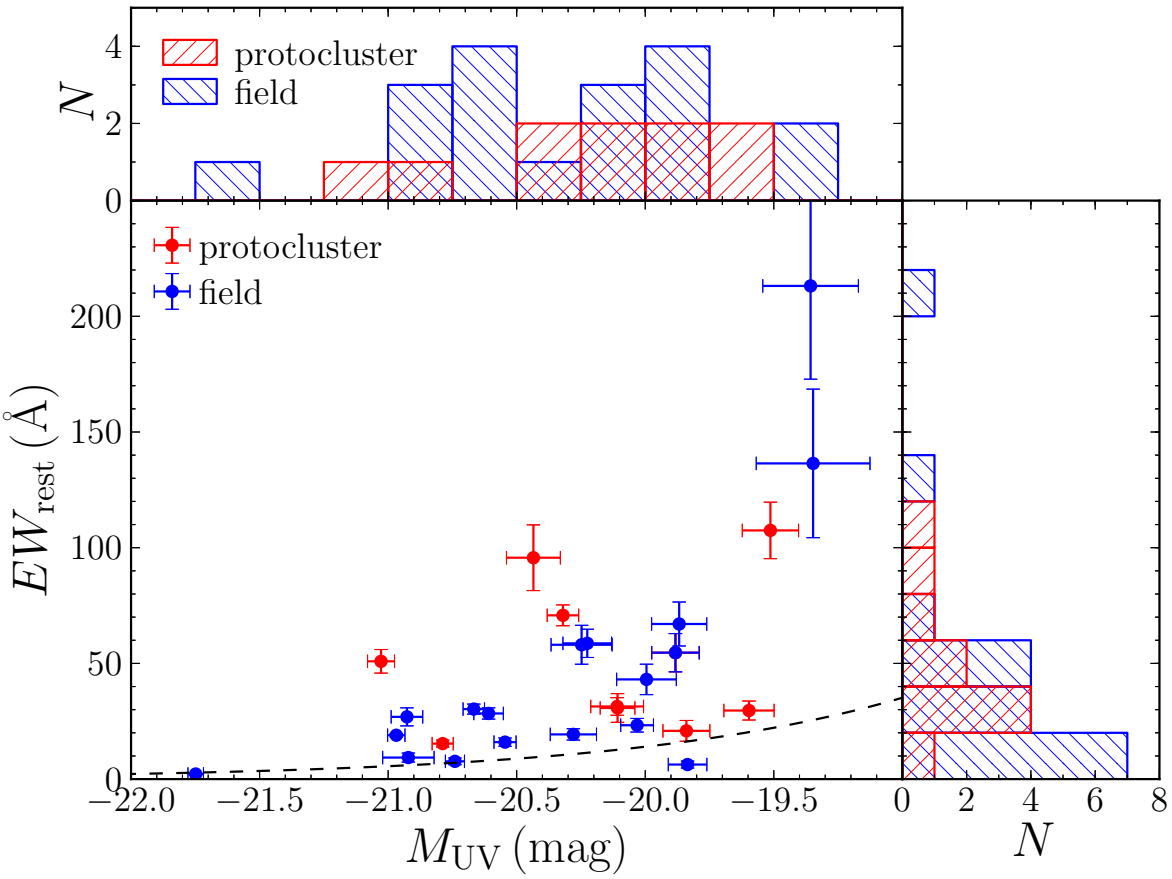

Fig. 50.— $EW_{\rm rest}$ versus $M_{\rm UV}$ of spectroscopically confirmed i-dropout galaxies in the SDF. The histograms in the top and right panels show the $EW_{\rm rest}$ and $M_{\rm UV}$ distributions of the protocluster and field galaxies. Red and blue color represent the protocluster and field galaxies, respectively. The dashed line indicates the 5σ detection limit of the spectroscopic observation.

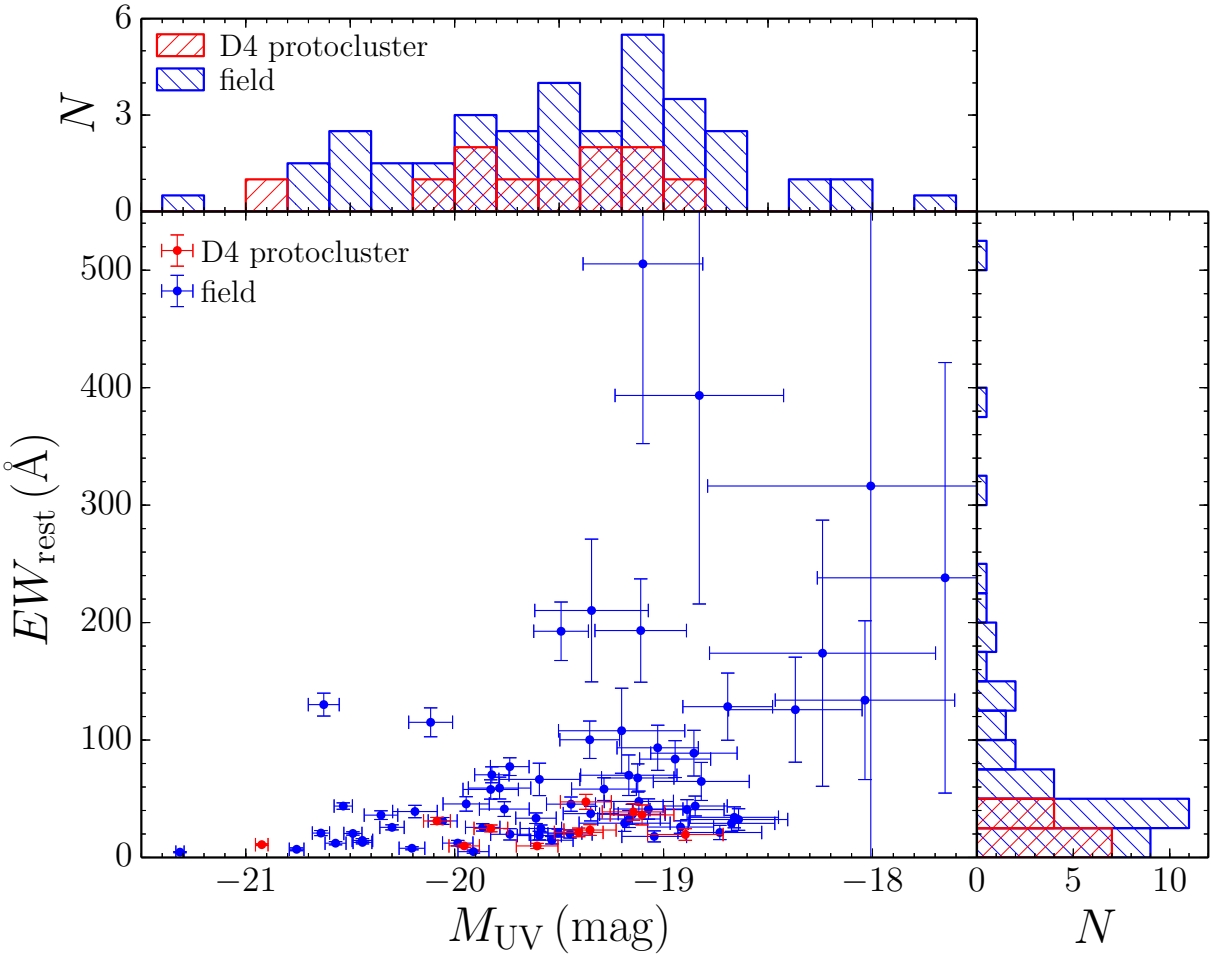

Fig. 51.— $EW_{\rm rest}$ versus $M_{\rm UV}$ of spectroscopically confirmed g-dropout galaxies in the CFHTLS D1 and D4. The histograms in the top and right panels show the $EW_{\rm rest}$ and $M_{\rm UV}$ distributions of the protocluster and field galaxies. Red and blue color represent the protocluster and field galaxies, respectively.

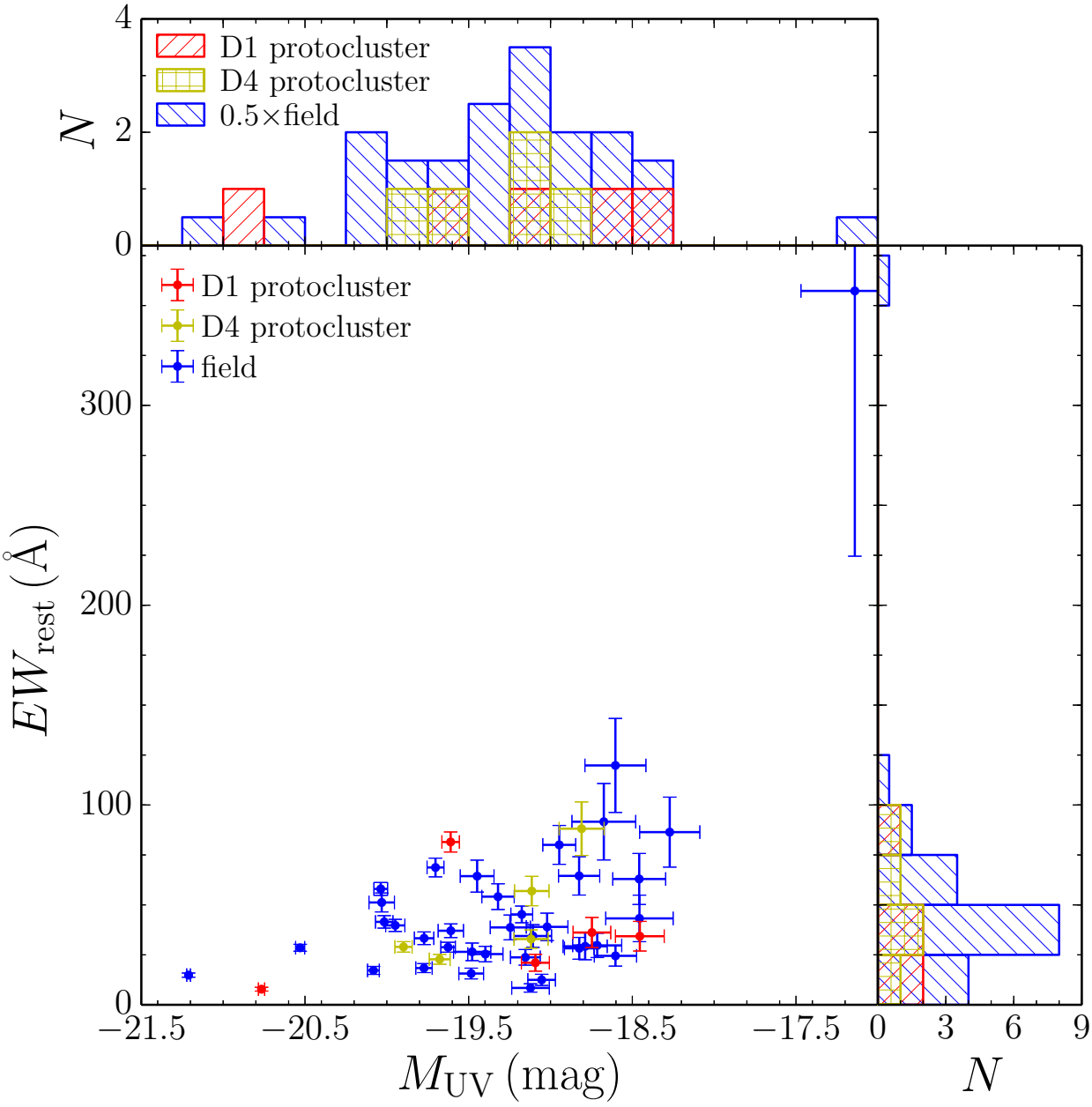

Fig. 52.— $EW_{\rm rest}$ versus $M_{\rm UV}$ of spectroscopically confirmed u-dropout galaxies in the CFHTLS D1 and D4. The histograms in the top and right panels show the $EW_{\rm rest}$ and $M_{\rm UV}$ distributions of the protocluster and field galaxies. The D1-$u$drop, D4-$u$drop protocluster, and field galaxies are represented in red, yellow, and blue, respectively.

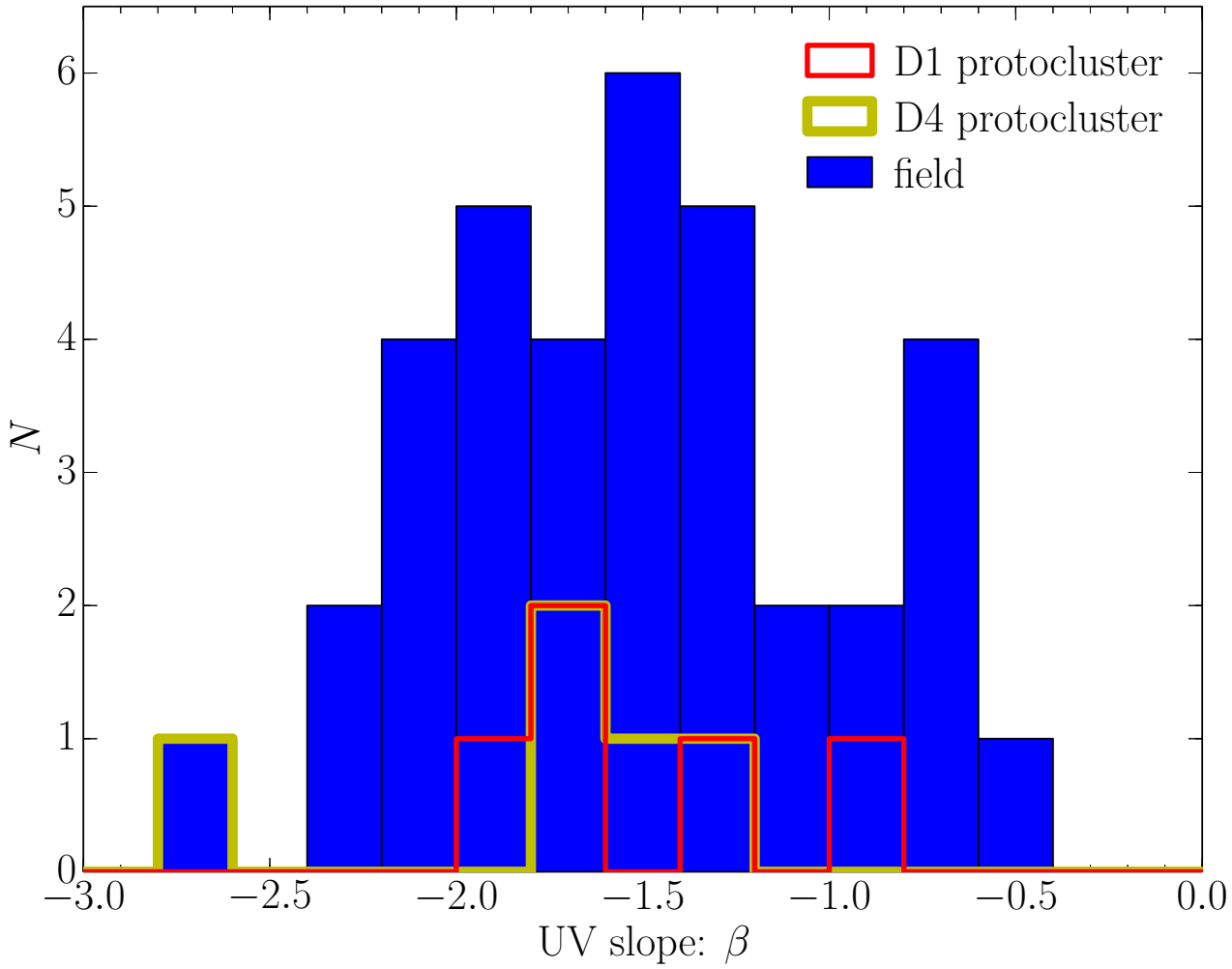

Fig. 53.— Distribution of UV slope of spectroscopically confirmed u-dropout galaxies in the CFHTLS D1 and D4. The D1-$u$drop, D4-$u$drop protocluster, and field galaxies are represented in red, yellow, and blue, respectively.

7. CONCLUSION

In this thesis, we have presented a protocluster survey from $z \sim 6$ to $z \sim 3$ in the SDF and CFHTLS Deep Fields. This survey was performed in the blank fields using wide-field imaging (i.e., RGs and QSOs were not used as protocluster probes). Protocluster candidates were identified by measuring the surface number density of dropout galaxies, and follow-up spectroscopic observations revealed that most of the candidates were real protoclusters. Our discovery of protoclusters includes one at $z = 6.01$, which is the highest-redshift protocluster known to date with sufficient spectroscopic confirmation. The major results and implications of this thesis are summarized below.

1. We investigated the sky distribution of u-, g-, r-, and i-dropout galaxies in the wide-field imaging of the SDF and the CFHTLS Deep Fields, and quantified the local surface number density by counting galaxies within a fixed aperture. We selected a total of 22 overdense regions with an overdensity significance greater than 4σ as protocluster candidates. The number density of protocluster candidates was approximately one candidate per $1\,\mathrm{deg}^2$ area. Based on this number density, we may infer that finding a protocluster in the SDF was serendipitous, as we must survey an area of a few square degrees in order to find each protocluster.

2. We investigated the relation between the overdensity at high redshifts and the descendant halo mass using the light-cone model. We selected galaxy samples with the same redshift distribution as the observations, and the same overdensity measurement was applied to this simulated sample of dropout galaxies. We find that the overdensity at high redshifts and the descendant halo mass at $z = 0$ were quite strongly correlated, and $\gtrsim 85\%$ of the overdense regions with significance over 4σ are expected to grow to dark matter halos with $M > 10^{14}\,\mathrm{M}_\odot$, which corresponds to a nearby cluster of galaxies at $z = 0$. The model predicts that protoclusters can be identified with high confidence by measuring the surface overdensity significance. Furthermore, from the model, protocluster members were, on average, spread within a scale of 2 physical Mpc radius and line-of-sight velocity of $|v| < 1000\,\mathrm{km\,s}^{-1}$.

3. We carried out follow-up spectroscopic observations of nine candidates to confirm whether these were genuine protoclusters. The redshift of protocluster members were determined by detecting Lyα emission lines, and there was no apparent contamination in our spectroscopic observation. Four of the nine protocluster candidates were confirmed to be genuine protoclusters by ascertaining that their member galaxies were significantly clustered both in terms of spatial and redshift spaces. We were not able to conclude whether the other candidates were genuine protoclusters due to the small number of spectroscopically confirmed galaxies, except for one candidate where the overdensity was determined through chance alignment. Our method to search for protoclusters utilizing wide-field imaging is reliable and sufficiently effective to construct high-redshift protocluster samples based on the success rate of follow-up observations.

4. We investigated the protocluster structure of the SDF-$i$drop and D4-$g$drop protoclusters, which have sufficient numbers of spectroscopically confirmed members. The protocluster at $z \sim 6$ was composed of several small subgroups that consist of a galaxy-pairs, implying

that galaxy assembly had only recently began. On the other hand, with the protocluster at $z \sim 3.7$, the distribution of member galaxies exhibited global structure composed of a core in which half of confirmed members was included, and outskirts, in which the remaining were randomly distributed throughout the surrounding regions. The results suggest that protocluster structure drastically evolved toward a virialized structure from $z \sim 6$ to $z \sim 3.7$, although further protocluster samples are required to confirm a general trend.

5. No differences were found between protocluster and field galaxies in terms of $M_{\rm star}$, $M_{\rm UV}$ and $EW_{\rm rest}$ at $z \sim 6$. In contrast, we find that $EW_{\rm rest}$ of the $z \sim 3.7$ protocluster was significantly smaller than that of field galaxies. We considered two physical mechanisms that may lead to this difference; the first is dust in member galaxies, and the second is intracluster neutral hydrogen gas. Although we were not able to draw definite conclusions based on our data, the UV slope (which is an indicator of dust) was found not to favor an interpretation whereby we attribute the difference in $EW_{\rm rest}$ only to dust in member galaxies. Our findings of a small $EW_{\rm rest}$ in more dynamically mature protocluster at lower-redshifts implies that the properties of protocluster galaxies might be affected by the environment in combination with dramatic changes in the internal structure. However, it should be noted that two $z \sim 3$ protoclusters showed inconsistent tendencies in terms of the protocluster properties, even with the same redshift.

The results described in this thesis are qualitatively and, in some respects, quantitatively consistent with the hierarchical structure formation model. The epoch of $z \sim 6$ may be a time when galaxies began to coalesce; in the subsequent virialization process, primitive protocluster cores appeared at $z \sim 3-4$ as progenitors of the cluster centers that are observed in the local universe. We found four new protoclusters using wide-field imaging without probes of overdense regions; however, the sample size was too small to elucidate a general picture of the structure formation and evolution of environmental effects. It is necessary to increase the number of protoclusters at redshifts of $z \sim 6$ to $z \sim 3$ to obtain a statistically significant sample across cosmic time. Using the new instrument of Hyper SuprimeCam (HSC) on the Subaru telescope, we plan to perform an unprecedented wide and deep survey over the next five years. This HSC survey is composed of three layers covered by five broad-bands of g-, r-, i-, z-, and y-bands (Ultradeep: $3.5\,{\rm deg}^2$ with the limiting magnitude of $m_i \sim 27.4\,{\rm mag}$, Deep: $27\,{\rm deg}^2$ with $m_i \sim 26.8\,{\rm mag}$, and Wide: $1400\,{\rm deg}^2$ with $m_i \sim 26.0\,{\rm mag}$). We estimate that the number of protoclusters that will be discovered from this Subaru strategic survey, based both on observations and the light-cone model, will be > 10 at $z \sim 6$, > 500 at $z \sim 5-4$, as well as even one at $z \sim 7$. This will enable us to derive a more complete picture of cluster formation and galaxy evolution in high density environments.

REFERENCES

Adams, S. M., Martini, P., Croxall, K. V., Overzier, R. A., & Silverman, J. D. 2014, arXiv:1407.2609

Alpaslan, M., Robotham, A. S. G., Driver, S., et al. 2014, MNRAS, 438, 177

Anders, P., & Fritze-v. Alvensleben, U. 2003, A&A, 401, 1063

Angulo, R. E., Springel, V., White, S. D. M., et al. 2012, MNRAS, 426, 2046

Aragón-Calvo, M. A., Jones, B. J. T., van de Weygaert, R., & van der Hulst, J. M. 2007, A&A, 474, 315

Aragón-Calvo, M. A., van de Weygaert, R., & Jones, B. J. T. 2010, MNRAS, 408, 2163

Bahcall, N. A., & Cen, R. 1993, ApJ, 407, L49

Bañados, E., Venemans, B., Walter, F., et al. 2013, ApJ, 773, 178

Barbosa, D., Bartlett, J. G., Blanchard, A., & Oukbir, J. 1996, A&A, 314, 13

Barkana, R., & Loeb, A. 1999, ApJ, 523, 54

Baugh, C. M., Benson, A. J., Cole, S., Frenk, C. S., & Lacey, C. G. 1999, MNRAS, 305, L21

Beers, T. C., Flynn, K., & Gebhardt, K. 1990, AJ, 100, 32

Benson, A. J., Frenk, C. S., Baugh, C. M., Cole, S., & Lacey, C. G. 2001, MNRAS, 327, 1041

Bertin, E., & Arnouts, S. 1996, A&AS, 117, 393

Best, P. N. 2000, MNRAS, 317, 720

Bielby, R., Hudelot, P., McCracken, H. J., et al. 2012, A&A, 545, A23

Blanton, M., Cen, R., Ostriker, J. P., Strauss, M. A., & Tegmark, M. 2000, ApJ, 531, 1

Böhringer, H., Schuecker, P., Guzzo, L., et al. 2004, A&A, 425, 367

Bond, J. R., Cole, S., Efstathiou, G., & Kaiser, N. 1991, ApJ, 379, 440

Bouwens, R. J., Illingworth, G. D., Franx, M., & Ford, H. 2007, ApJ, 670, 928

Bouwens, R. J., Illingworth, G. D., Franx, M., et al. 2009, ApJ, 705, 936

Bouwens, R. J., Illingworth, G. D., Labbe, I., et al. 2011, Nature, 469, 504

Bouwens, R. J., Illingworth, G. D., Oesch, P. A., et al. 2011, ApJ, 737, 90

Bouwens, R. J., Illingworth, G. D., Oesch, P. A., et al. 2012, ApJ, 754, 83

Bouwens, R. J., Bradley, L., Zitrin, A., et al. 2014, ApJ, 795, 126

Bower, R. G. 1991, MNRAS, 248, 332

Bruzual, G., & Charlot, S. 2003, MNRAS, 344, 1000

Butcher, H., & Oemler, A., Jr. 1984, ApJ, 285, 426

Calzetti, D., Armus, L., Bohlin, R. C., et al. 2000, ApJ, 533, 682

Capak, P. L., Riechers, D., Scoville, N. Z., et al. 2011, Nature, 470, 233

Casali, M., Adamson, A., Alves de Oliveira, C., et al. 2007, A&A, 467, 777

Cassata, P., Tasca, L. A. M., Le Fèvre, O., et al. 2015, A&A, 573, A24

Chiang, Y.-K., Overzier, R., & Gebhardt, K. 2013, ApJ, 779, 127

Coil, A. L., Hennawi, J. F., Newman, J. A., Cooper, M. C., & Davis, M. 2007, ApJ, 654, 115

Colless, M., Dalton, G., Maddox, S., et al. 2001, MNRAS, 328, 1039

Cooke, J., Berrier, J. C., Barton, E. J., Bullock, J. S., & Wolfe, A. M. 2010, MNRAS, 403, 1020

Croom, S. M., Boyle, B. J., Shanks, T., et al. 2005, MNRAS, 356, 415

Cucciati, O., Zamorani, G., Lemaux, B. C., et al. 2014, A&A, 570, A16

Curtis-Lake, E., McLure, R. J., Pearce, H. J., et al. 2012, MNRAS, 422, 1425

Dannerbauer, H., Kurk, J. D., De Breuck, C., et al. 2014, A&A, 570, A55

de Lapparent, V., Geller, M. J., & Huchra, J. P. 1986, ApJ, 302, L1

De Lucia, G., Springel, V., White, S. D. M., Croton, D., & Kauffmann, G. 2006, MNRAS, 366, 499

De Lucia, G., & Blaizot, J. 2007, MNRAS, 375, 2

Digby-North, J. A., Nandra, K., Laird, E. S., et al. 2010, MNRAS, 407, 846

Donoso, E., Li, C., Kauffmann, G., Best, P. N., & Heckman, T. M. 2010, MNRAS, 407, 1078

Dressler, A. 1980, ApJ, 236, 351

Driver, S. P., Hill, D. T., Kelvin, L. S., et al. 2011, MNRAS, 413, 971

Einasto, M., Lietzen, H., Tempel, E., et al. 2014, A&A, 562, A87

Eisenhardt, P. R. M., Brodwin, M., Gonzalez, A. H., et al. 2008, ApJ, 684, 905

Eke, V. R., Navarro, J. F., & Frenk, C. S. 1998, ApJ, 503, 569

Eyles, L. P., Bunker, A. J., Ellis, R. S., et al. 2007, MNRAS, 374, 910

Faber, S. M., Phillips, A. C., Kibrick, R. I., et al. 2003, Proc. SPIE, 4841, 1657

Fazio, G. G., Hora, J. L., Allen, L. E., et al. 2004, ApJS, 154, 10

Finkelstein, S. L., Rhoads, J. E., Malhotra, S., & Grogin, N. 2009, ApJ, 691, 465

Finkelstein, S. L., Hill, G. J., Gebhardt, K., et al. 2011, ApJ, 729, 140

Finkelstein, S. L., Papovich, C., Dickinson, M., et al. 2013, Nature, 502, 524

Finoguenov, A., Guzzo, L., Hasinger, G., et al. 2007, ApJS, 172, 182

Flin, P., & Krywult, J. 2006, A&A, 450, 9

Fontana, A., Vanzella, E., Pentericci, L., et al. 2010, ApJ, 725, L205

Galametz, A., Vernet, J., De Breuck, C., et al. 2010, A&A, 522, A58

George, M. R., Leauthaud, A., Bundy, K., et al. 2011, ApJ, 742, 125

Gladders, M. D., & Yee, H. K. C. 2000, AJ, 120, 2148

Giavalisco, M., Steidel, C. C., & Szalay, A. S. 1994, ApJ, 425, L5

Girardi, L., Groenewegen, M. A. T., Hatziminaoglou, E., & da Costa, L. 2005, A&A, 436, 895

Gobat, R., Daddi, E., Onodera, M., et al. 2011, A&A, 526, A133

Gobat, R., Strazzullo, V., Daddi, E., et al. 2013, ApJ, 776, 9

Gould, A., Bahcall, J. N., & Flynn, C. 1996, ApJ, 465, 759

Graur, O., Poznanski, D., Maoz, D., et al. 2011, MNRAS, 417, 916

Guo, Q., White, S., Boylan-Kolchin, M., et al. 2011, MNRAS, 413, 101

Gwyn, S. D. J. 2012, AJ, 143, 38

Haines, C. P., Gargiulo, A., & Merluzzi, P. 2008, MNRAS, 385, 1201

Haines, C. P., Smith, G. P., Egami, E., et al. 2009, ApJ, 704, 126

Hatch, N. A., De Breuck, C., Galametz, A., et al. 2011a, MNRAS, 410, 1537

Hatch, N. A., Kurk, J. D., Pentericci, L., et al. 2011b, MNRAS, 415, 2993

Hatch, N. A., Wylezalek, D., Kurk, J. D., et al. 2014, MNRAS, 445, 280

Hawley, S. L., Covey, K. R., Knapp, G. R., et al. 2002, AJ, 123, 3409

Hayashi, M., Kodama, T., Tadaki, K.-i., Koyama, Y., & Tanaka, I. 2012, ApJ, 757, 15

Henriques, B. M. B., White, S. D. M., Lemson, G., et al. 2012, MNRAS, 421, 2904

Hook, I. M., Jørgensen, I., Allington-Smith, J. R., et al. 2004, PASP, 116, 425

Husband, K., Bremer, M. N., Stanway, E. R., et al. 2013, MNRAS, 432, 2869

Iliev, I. T., Shapiro, P. R., McDonald, P., Mellema, G., & Pen, U.-L. 2008, MNRAS, 391, 63

Inoue, A. K., Shimizu, I., Iwata, I., & Tanaka, M. 2014, MNRAS, 442, 1805

Ishigaki, M., Kawamata, R., Ouchi, M., et al. 2014, arXiv:1408.6903

Jiang, L., Egami, E., Kashikawa, N., et al. 2011, ApJ, 743, 65

Kang, E., & Im, M. 2009, ApJ, 691, L33

Kashikawa, N., Aoki, K., Asai, R., et al. 2002, PASJ, 54, 819

Kashikawa, N., Shimasaku, K., Yasuda, N., et al. 2004, PASJ, 56, 1011

Kashikawa, N., Shimasaku, K., Malkan, M. A., et al. 2006, ApJ, 648, 7

Kashikawa, N., Kitayama, T., Doi, M., et al. 2007, ApJ, 663, 765

Kashikawa, N., Shimasaku, K., Matsuda, Y., et al. 2011, ApJ, 734, 119

Kauffmann, G. 1995, MNRAS, 274, 153

Kauffmann, G., Colberg, J. M., Diaferio, A., & White, S. D. M. 1999, MNRAS, 307, 529

Kennicutt, R. C., Jr. 1998, ARA&A, 36, 189

Kim, S., Stiavelli, M., Trenti, M., et al. 2009, ApJ, 695, 809

Kodama, T., Tanaka, I., Kajisawa, M., et al. 2007, MNRAS, 377, 1717

Konno, A., Ouchi, M., Ono, Y., et al. 2014, ApJ, 797, 16

Kovač, K., Somerville, R. S., Rhoads, J. E., Malhotra, S., & Wang, J. 2007, ApJ, 668, 15

Krueger, H., Fritze-v. Alvensleben, U., & Loose, H.-H. 1995, A&A, 303, 41

Kubo, M., Uchimoto, Y. K., Yamada, T., et al. 2013, ApJ, 778, 170

Kuiper, E., Hatch, N. A., Röttgering, H. J. A., et al. 2010, MNRAS, 405, 969

Kuiper, E., Hatch, N. A., Miley, G. K., et al. 2011, MNRAS, 415, 2245

Kuiper, E., Hatch, N. A., Venemans, B. P., et al. 2011, MNRAS, 417, 1088

Kuiper, E., Venemans, B. P., Hatch, N. A., Miley, G. K., Röttgering, H. J. A. 2012, MNRAS, 425, 801

Kulas, K. R., McLean, I. S., Shapley, A. E., et al. 2013, ApJ, 774, 130

Lahav, O., Lilje, P. B., Primack, J. R., & Rees, M. J. 1991, MNRAS, 251, 128

Lee, K.-S., Dey, A., Cooper, M. C., Reddy, N., & Jannuzi, B. T. 2013, ApJ, 771, 25

Lee, K.-S., Dey, A., Hong, S., et al. 2014, ApJ, 796, 126

Le Fevre, O., Deltorn, J. M., Crampton, D., & Dickinson, M. 1996, ApJ, 471, L11

Le Fevre, O., Tasca, L. A. M., Cassata, P., et al. 2014, arXiv:1403.3938

Lehmer, B. D., Alexander, D. M., Geach, J. E., et al. 2009, ApJ, 691, 687

Lemaux, B. C., Cucciati, O., Tasca, L. A. M., et al. 2014, A&A, 572, A41

Lerchster, M., Seitz, S., Brimioulle, F., et al. 2011, MNRAS, 411, 2667

Lloyd-Davies, E. J., Romer, A. K., Mehrtens, N., et al. 2011, MNRAS, 418, 14

Ly, C., Malkan, M. A., Kashikawa, N., et al. 2007, ApJ, 657, 738

Ly, C., Malkan, M. A., Kashikawa, N., et al. 2012, ApJ, 757, 63

Madau, P. 1995, ApJ, 441, 18

Malhotra, S., Rhoads, J. E., Pirzkal, N., et al. 2005, ApJ, 626, 666

Mandelbaum, R., Li, C., Kauffmann, G., & White, S. D. M. 2009, MNRAS, 393, 377

Matsuda, Y., Yamada, T., Hayashino, T., et al. 2011, MNRAS, 410, L13

Mayo, J. H., Vernet, J., De Breuck, C., et al. 2012, A&A, 539, A33

McLure, R. J., Dunlop, J. S., Bowler, R. A. A., et al. 2013, MNRAS, 432, 2696

McQuinn, M., Hernquist, L., Zaldarriaga, M., & Dutta, S. 2007, MNRAS, 381, 75

Meiksin, A. 2006, MNRAS, 365, 807

Miley, G., & De Breuck, C. 2008, A&A Rev., 15, 67

Miyazaki, S., Komiyama, Y., Sekiguchi, M., et al. 2002, PASJ, 54, 833

Miyazaki, M., Shimasaku, K., Kodama, T., et al. 2003, PASJ, 55, 1079

Morselli, L., Mignoli, M., Gilli, R., et al. 2014, A&A, 568, A1

Mortonson, M. J., Hu, W., & Huterer, D. 2011, Phys. Rev. D, 83, 023015

McLure, R. J., Dunlop, J. S., de Ravel, L., et al. 2011, MNRAS, 418, 2074

Muldrew, S. I., Croton, D. J., Skibba, R. A., et al. 2012, MNRAS, 419, 2670

Muzzin, A., Wilson, G., Demarco, R., et al. 2013, ApJ, 767, 39

Nagao, T., Murayama, T., Maiolino, R., et al. 2007, A&A, 468, 877

Nakajima, T., Iwamuro, F., Maihara, T., et al. 2000, AJ, 120, 2488

Ono, Y., Ouchi, M., Shimasaku, K., et al. 2010, MNRAS, 402, 1580

Ono, Y., Ouchi, M., Shimasaku, K., et al. 2010, ApJ, 724, 1524

Ono, Y., Ouchi, M., Mobasher, B., et al. 2012, ApJ, 744, 83

Orsi, A., Lacey, C. G., Baugh, C. M., & Infante, L. 2008, MNRAS, 391, 1589

Osterbrock, D. E., & Ferland, G. J. 2006, Astrophysics of gaseous nebulae and active galactic nuclei, 2nd. ed. by D.E. Osterbrock and G.J. Ferland. Sausalito, CA: University Science Books, 2006

Ota, K., Iye, M., Kashikawa, N., et al. 2008, ApJ, 677, 12

Ouchi, M., Shimasaku, K., Furusawa, H., et al. 2003, ApJ, 582, 60

Ouchi, M., Shimasaku, K., Akiyama, M., et al. 2005, ApJ, 620, L1

Overzier, R. A., Miley, G. K., Bouwens, R. J., et al. 2006, ApJ, 637, 58

Overzier, R. A., Bouwens, R. J., Cross, N. J. G., et al. 2008, ApJ, 673, 143

Overzier, R. A., Guo, Q., Kauffmann, G., et al. 2009, MNRAS, 394, 577

Overzier, R. A., Shu, X., Zheng, W., et al. 2009, ApJ, 704, 548

Overzier, R., Lemson, G., Angulo, R. E., et al. 2013, MNRAS, 428, 778

Papovich, C., Dickinson, M., & Ferguson, H. C. 2001, ApJ, 559, 620

Papovich, C., Momcheva, I., Willmer, C. N. A., et al. 2010, ApJ, 716, 1503

Park, C., Choi, Y.-Y., Kim, J., et al. 2012, ApJ, 759, L7

Peng, C. Y., Ho, L. C., Impey, C. D., & Rix, H.-W. 2002, AJ, 124, 266

Pentericci, L., Roettgering, H. J. A., Miley, G. K., Carilli, C. L., & McCarthy, P. 1997, A&A, 326, 580

Pentericci, L., Kurk, J. D., Röttgering, H. J. A., et al. 2000, A&A, 361, L25

Pisani, A. 1993, MNRAS, 265, 706

Pisani, A. 1996, MNRAS, 278, 697

Popesso, P., Rodighiero, G., Saintonge, A., et al. 2011, A&A, 532, A145

Poznanski, D., Maoz, D., Yasuda, N., et al. 2007, MNRAS, 382, 1169

Ramella, M., Biviano, A., Pisani, A., et al. 2007, A&A, 470, 39

Rasmussen, J., Mulchaey, J. S., Bai, L., et al. 2012, ApJ, 757, 122

Reichardt, C. L., Stalder, B., Bleem, L. E., et al. 2013, ApJ, 763, 127

Rhoads, J. E., Malhotra, S., Dey, A., et al. 2000, ApJ, 545, L85

Richard, J., Kneib, J.-P., Ebeling, H., et al. 2011, MNRAS, 414, L31

Rosati, P., Della Ceca, R., Norman, C., & Giacconi, R. 1998, ApJ, 492, L21

Salpeter, E. E. 1955, ApJ, 121, 161

Salvador-Sole, E., Gonzalez-Casado, G., & Solanes, J. M. 1993, ApJ, 410, 1

Schenker, M. A., Stark, D. P., Ellis, R. S., et al. 2012, ApJ, 744, 179

Seldner, M., Siebers, B., Groth, E. J., & Peebles, P. J. E. 1977, AJ, 82, 249

Shattow, G. M., Croton, D. J., Skibba, R. A., et al. 2013, MNRAS, 433, 3314

Shibuya, T., Kashikawa, N., Ota, K., et al. 2012, ApJ, 752, 114

Shimakawa, R., Kodama, T., Tadaki, K.-i., et al. 2014, arXiv:1406.5219

Shimasaku, K., Ouchi, M., Okamura, S., et al. 2003, ApJ, 586, L111

Simpson, C., Mortlock, D., Warren, S., et al. 2014, MNRAS, 442, 3454

Smargon, A., Mandelbaum, R., Bahcall, N., & Niederste-Ostholt, M. 2012, MNRAS, 423, 856

Spitler, L. R., Labbé, I., Glazebrook, K., et al. 2012, ApJ, 748, L21

Springel, V., White, S. D. M., Jenkins, A., et al. 2005, Nature, 435, 629

Stanford, S. A., Romer, A. K., Sabirli, K., et al. 2006, ApJ, 646, L13

Stanway, E. R., Bremer, M. N., Davies, L. J. M., et al. 2008, ApJ, 687, L1

Stark, D. P., Ellis, R. S., Bunker, A., et al. 2009, ApJ, 697, 1493

Stark, D. P., Ellis, R. S., Chiu, K., Ouchi, M., & Bunker, A. 2010, MNRAS, 408, 1628

Stark, D. P., Ellis, R. S., & Ouchi, M. 2011, ApJ, 728, L2

Steidel, C. C., & Hamilton, D. 1992, AJ, 104, 941

Steidel, C. C., Pettini, M., & Hamilton, D. 1995, AJ, 110, 2519

Steidel, C. C., Adelberger, K. L., Dickinson, M., et al. 1998, ApJ, 492, 428

Steidel, C. C., Adelberger, K. L., Shapley, A. E., et al. 2005, ApJ, 626, 44

Stiavelli, M., Djorgovski, S. G., Pavlovsky, C., et al. 2005, ApJ, 622, L1

Storey, P. J., & Hummer, D. G. 1995, MNRAS, 272, 41

Sunyaev, R. A., & Zeldovich, Y. B. 1972, Comments on Astrophysics and Space Physics, 4, 173

Tamura, Y., Iono, D., Wilner, D. J., et al. 2010, ApJ, 724, 1270

Tanaka, M., Finoguenov, A., & Ueda, Y. 2010, ApJ, 716, L152

Tegmark, M., Blanton, M. R., Strauss, M. A., et al. 2004, ApJ, 606, 702

Thomas, D., Maraston, C., Bender, R., & Mendes de Oliveira, C. 2005, ApJ, 621, 673

Trenti, M., Bradley, L. D., Stiavelli, M., et al. 2012, ApJ, 746, 55

Treu, T., Schmidt, K. B., Trenti, M., Bradley, L. D., & Stiavelli, M. 2013, ApJ, 775, L29

Valentino, F., Daddi, E., Strazzullo, V., et al. 2014, arXiv:1410.1437

Vanzella, E., Pentericci, L., Fontana, A., et al. 2011, ApJ, 730, L35

Venemans, B. P., Kurk, J. D., Miley, G. K., et al. 2002, ApJ, 569, L11

Venemans, B. P., Röttgering, H. J. A., Overzier, R. A., et al. 2004, A&A, 424, L17

Venemans, B. P., Röttgering, H. J. A., Miley, G. K., et al. 2005, A&A, 431, 793

Venemans, B. P., Röttgering, H. J. A., Miley, G. K., et al. 2007, A&A, 461, 823

Vikhlinin, A., Voevodkin, A., Mullis, C. R., et al. 2003, ApJ, 590, 15

Visvanathan, N., & Sandage, A. 1977, ApJ, 216, 214

Voit, G. M. 2005, Reviews of Modern Physics, 77, 207

van der Burg, R. F. J., Hildebrandt, H., & Erben, T. 2010, A&A, 523, A74

von der Linden, A., Best, P. N., Kauffmann, G., & White, S. D. M. 2007, MNRAS, 379, 867

Vulcani, B., Poggianti, B. M., Fasano, G., et al. 2012, MNRAS, 420, 1481

Wake, D. A., Croom, S. M., Sadler, E. M., & Johnston, H. M. 2008, MNRAS, 391, 1674

Wen, Z. L., Han, J. L., & Liu, F. S. 2010, MNRAS, 407, 533

West, M. J., Oemler, A., Jr., & Dekel, A. 1988, ApJ, 327, 1

Wilkins, S. M., Bunker, A. J., Lorenzoni, S., & Caruana, J. 2011, MNRAS, 411, 23

Wilkins, S. M., Bunker, A. J., Stanway, E., Lorenzoni, S., & Caruana, J. 2011, MNRAS, 417, 717

Wylezalek, D., Galametz, A., Stern, D., et al. 2013, ApJ, 769, 79

Wylezalek, D., Vernet, J., De Breuck, C., et al. 2014, ApJ, 786, 17

Yates, M. G., Miller, L., & Peacock, J. A. 1989, MNRAS, 240, 129

Yoshikawa, K., Taruya, A., Jing, Y. P., & Suto, Y. 2001, ApJ, 558, 520

Zheng, W., Overzier, R. A., Bouwens, R. J., et al. 2006, ApJ, 640, 574

Zheng, Z., Flynn, C., Gould, A., Bahcall, J. N., & Salim, S. 2001, ApJ, 555, 393

Zheng, Z., Flynn, C., Gould, A., Bahcall, J. N., & Salim, S. 2004, ApJ, 601, 500

Zirm, A. W., Stanford, S. A., Postman, M., et al. 2008, ApJ, 680, 224

Zirm, A. W., Toft, S., & Tanaka, M. 2012, ApJ, 744, 181